

# A model for cosmological simulations of galaxy formation physics

Mark Vogelsberger<sup>1\*</sup>, Shy Genel<sup>1</sup>, Debora Sijacki<sup>1,2</sup>, Paul Torrey<sup>1</sup>, Volker Springel<sup>3,4</sup>, and Lars Hernquist<sup>1</sup>

<sup>1</sup> *Harvard-Smithsonian Center for Astrophysics, 60 Garden Street, Cambridge, MA, 02138, USA*

<sup>2</sup> *Kavli Institute for Cosmology, Cambridge and Institute of Astronomy, Madingley Road, Cambridge, CB3 0HA*

<sup>3</sup> *Heidelberg Institute for Theoretical Studies, Schloss-Wolfsbrunnenweg 35, 69118 Heidelberg, Germany*

<sup>4</sup> *Zentrum für Astronomie der Universität Heidelberg, ARI, Mönchhofstr. 12-14, 69120 Heidelberg, Germany*

23 December 2013

## ABSTRACT

We present a new comprehensive model of the physics of galaxy formation designed for large-scale hydrodynamical simulations of structure formation using the moving mesh code AREPO. Our model includes primordial and metal line cooling with self-shielding corrections, stellar evolution and feedback processes, gas recycling, chemical enrichment, a novel subgrid model for the metal loading of outflows, black hole (BH) seeding, BH growth and merging procedures, quasar- and radio-mode feedback, and a prescription for radiative electromagnetic (EM) feedback from active galactic nuclei (AGN). Our stellar evolution and chemical enrichment scheme follows nine elements (H, He, C, N, O, Ne, Mg, Si, Fe) independently. Stellar feedback is realised through kinetic outflows. The metal mass loading of outflows can be adjusted independently of the wind mass loading. This is required to simultaneously reproduce the stellar mass content of low mass haloes and their gas oxygen abundances. Radiative EM AGN feedback is implemented assuming an average spectral energy distribution and a luminosity-dependent scaling of obscuration effects. This form of feedback suppresses star formation more efficiently than continuous thermal quasar-mode feedback alone, but is less efficient than mechanical radio-mode feedback in regulating star formation in massive haloes. We contrast simulation predictions for different variants of our galaxy formation model with key observations, allowing us to constrain the importance of different modes of feedback and their uncertain efficiency parameters. We identify a fiducial best match model and show that it reproduces, among other things, the cosmic star formation history, the stellar mass function, the stellar mass – halo mass relation, g-, r-, i-, z-band SDSS galaxy luminosity functions, and the Tully-Fisher relation. We can achieve this success only if we invoke very strong forms of stellar and AGN feedback such that star formation is adequately reduced in both low and high mass systems. In particular, the strength of radio-mode feedback needs to be increased significantly compared to previous studies to suppress efficient cooling in massive, metal-enriched haloes.

**Key words:** methods: numerical – cosmology: theory – cosmology: galaxy formation

## 1 INTRODUCTION

In the standard model of cosmology, the dominant mass contribution to the Universe is in the form of cold dark matter (DM). Together with a large dark energy (DE) component (Riess et al. 1999; Perlmutter et al. 1999), this is the defining feature of the concordance  $\Lambda$  cold dark matter ( $\Lambda$ CDM) cosmogony. Early models of structure formation have predicted the condensation of baryons via radiative cooling at the centres of a population of hierarchically

growing DM haloes, forming galaxies (Silk 1977; Rees & Ostriker 1977; White & Rees 1978; Blumenthal et al. 1984). Galaxy formation theory aims to explain the observed galaxy population of our Universe through a self-consistent model which requires as input only the initial conditions left behind after the Big Bang, as inferred from the cosmic microwave background (CMB). Such a model needs to correctly predict the evolution of all constituents of the Universe: DM, DE *and* baryons. Despite the fact that it is still unknown what DM and DE are, numerical N-body simulations of these “dark components” have reached a high degree of sophistication over the past decade, making possible accurate calculations

\* Hubble Fellow, mvogelsb@cfa.harvard.edu

far into the non-linear regime (e.g., Springel et al. 2005c, 2008; Boylan-Kolchin et al. 2010; Klypin et al. 2011; Wu et al. 2013).

However, to make direct connections with the large amount of available and upcoming observations of the *visible* universe, simulations must also account for baryonic physics. Especially in the era of “precision cosmology” based on large surveys like SDSS, LSST, etc., it is crucial to have predictive, accurate and reliable galaxy formation models to test our understanding of structure formation by confronting these models with a plethora of data. Including baryons in cosmological models is also a necessity for predicting the back-reaction of baryons on the dark matter distribution, an effect that is particularly important for observational searches of dark matter and for concluding whether the  $\Lambda$ CDM model is viable on small scales (Vogelsberger et al. 2009; Ling et al. 2010).

There are currently two main approaches for computing cosmological models of galaxy formation and evolution: so-called semi-analytic models and self-consistent hydrodynamical simulations. Semi-analytic models (e.g., White & Frenk 1991; Kauffmann et al. 1993; Baugh 2006; Croton et al. 2006; Guo et al. 2011; Benson 2012) account for baryonic physics by adding galaxy formation as a post-processing step on top of the output of N-body simulations or onto Monte-Carlo realisations of dark matter merger history trees. Specifically, this approach uses simple analytical prescription to describe the baryonic physics that shape galaxy populations. Typically, the free parameters of the models are tuned to reproduce certain key observations, like the local stellar mass function, and are then used to predict other characteristics of the observed galaxy population. By contrasting those predictions to observations the model can then be refined. While this approach allows a fast parameter space exploration of the relevant physics at play, its predictive power for certain observables is limited. For example, semi-analytic models do not permit a detailed prediction for the gas properties of the intergalactic medium (IGM), let alone the circumgalactic medium (CGM) in and around galaxy haloes. Moreover, since the gas dynamics in the semi-analytic approach is approximated only in a very crude way, it is difficult to correctly identify the primary physics driving the outcome.

The most general way to overcome these limitations is to couple the gas physics to the “dark components” and perform fully self-consistent hydrodynamical simulations in cosmological volumes. This approach is significantly more expensive from a computational point of view than semi-analytic models. In addition, modelling the required physics in a numerically meaningful way is also challenging. The difficulties arise from two different considerations: (i) the underlying numerical technique must solve the hydrodynamical equations efficiently and accurately, and offer a sufficiently large dynamic range to describe both cosmological and galactic scales; and (ii) the relevant baryonic processes must be implemented in a physically and numerically meaningful way. Especially the latter point should not be viewed as an after-thought – owing to inevitable technical limitations, brute force implementations of the physics are often ill-posed numerically, non-convergent, and may produce spurious results. These limitations can be overcome only by employing sub-grid prescriptions that provide numerical closure, albeit at the cost of some modelling uncertainty. Such sub-resolution models aim to link the unresolved small-scale physics within galaxies to the scales that can actually be resolved in large-scale cosmological simulations. We stress that any numerical model always requires closure at some scale, since cosmological simulations cannot resolve all scales. Schemes without closure naturally lack convergence. This can be seen for example in the recent comparison paper by Scannapieco et al. (2012) and in more

detail in Marinacci et al. (2013), where different numerical implementations were compared. Fig. 21 (bottom left) in Marinacci et al. (2013) demonstrates that the convergence properties of a numerically well-posed scheme (as presented below) are significantly better than those other methods. We note that this does not mean, that smaller scales can and should not be resolved in future simulations. But we stress that this has to be done in a numerically meaningful way such that convergence can be achieved.

Many previous studies have argued that accurate schemes for solving the inviscid Euler equations are crucial for reliably modelling galaxy formation (Frenk et al. 1999; Agertz et al. 2007; Mitchell et al. 2009; Sijacki et al. 2012). Recently, we have corroborated this point explicitly through a detailed comparison campaign between simulations carried out with the moving-mesh code AREPO (Springel 2010) and with smoothed particle hydrodynamics (SPH) with the GADGET (last described in Springel et al. 2005b) code. The differences we identified are sufficiently large to qualitatively change the way galaxies accrete their gas (Nelson et al. 2013), and to quantitatively modify the strength of required feedback processes. We stress that these results were obtained with “standard SPH” as implemented in the GADGET code. We hence consider it essential to eliminate numerical artifacts and errors in galaxy formation simulations as far as possible. Without doing so, the physical models used to describe effects associated with star formation, black hole growth, and feedback will be corrupted by numerical limitations. Furthermore, galaxy formation simulations should ideally be performed at the highest possible resolution in order to faithfully model also small galaxies and to limit the amount of relevant physics modelled as “sub-grid”. This clearly requires a very good scaling behaviour of the employed numerical scheme to allow the use of state-of-the-art supercomputers.

Over the last several years, a large body of results based on hydrodynamical simulations of galaxy formation have been obtained (e.g., Ocvirk et al. 2008; Crain et al. 2009; Schaye et al. 2010; Davé et al. 2011b; McCarthy et al. 2012; Puchwein & Springel 2013; Kannan et al. 2013). A detailed investigation of the impact of various physical mechanisms on cosmic gas can be found in Schaye et al. (2010) as well as in other recent studies (e.g. Haas et al. 2012a,b). A consensus from these works is that feedback processes are crucial for any successful model of galaxy formation. For example, Davé et al. (2011b) focused on the impact of stellar winds on the faint-end of the stellar mass function. Puchwein & Springel (2013) tried to match the stellar mass function and the stellar mass – halo mass relation through stellar and active galactic nuclei (AGN) feedback, but their simulations did not include effects like metal line cooling and gas recycling. Other studies focused specifically on low mass haloes and showed that specific forms of stellar feedback may be successful in producing the correct amount of stellar mass in these systems (e.g. McCarthy et al. 2012; Kannan et al. 2013).

We note that these cosmological simulations of the formation of representative galaxy populations are markedly different from studies where the computational power is focused on a single galaxy (e.g., Governato et al. 2010; Agertz et al. 2011; Guedes et al. 2011; Genel et al. 2012; Scannapieco et al. 2012; Aumer et al. 2013). In the latter case, a very high spatial and mass resolution can be achieved, allowing one to resolve the physics to smaller scales. However, one does not obtain a statistical sample of objects to compare to observations. Moreover, the impact of numerical artifacts inherent to some methods such as SPH varies significantly from one halo to another (e.g., Vogelsberger et al. 2012; Sales et al. 2012). This means that physics models calibrated against individ-

ual objects will be corrupted by numerical errors in unpredictable ways, rendering their applicability to galaxy populations problematic. These considerations limit the ability of such “zoom-in” simulations by themselves to constrain galaxy formation models. Nevertheless, when used in conjunction with large-scale simulations, the zoom-in procedure will be essential for constructing more reliable sub-resolution models for characterising entire galaxy populations.

Modern cosmological hydrodynamical simulations typically include a sub-resolution model for star formation (e.g., Ascibar et al. 2002; Springel & Hernquist 2003a; Schaye & Dalla Vecchia 2008; Dubois & Teyssier 2008; Few et al. 2012), radiative cooling (e.g., Katz et al. 1996; Wiersma et al. 2009a), and chemical enrichment (e.g., Steinmetz & Mueller 1994; Mosconi et al. 2001; Lia et al. 2002; Springel & Hernquist 2003a; Kobayashi 2004; Scannapieco et al. 2005; Tornatore et al. 2007; Oppenheimer & Davé 2008; Wiersma et al. 2009b; Few et al. 2012). Furthermore, some small-scale simulations also include magnetic fields (e.g., Teyssier et al. 2006; Dolag & Staszczyn 2009; Collins et al. 2010; Pakmor et al. 2011; Pakmor & Springel 2012), radiative transfer (e.g., Abel & Wandelt 2002; Petkova & Springel 2010; Cantalupo & Porciani 2011), cosmic ray physics (Jubelgas et al. 2008) and thermal conduction (Jubelgas et al. 2004; Dolag et al. 2004). Most importantly, hydrodynamic simulations of galaxy formation usually include some form of stellar feedback (e.g., Dekel & Silk 1986; Navarro & White 1993; Mihos & Hernquist 1994; Gerritsen & Icke 1997; Thacker & Couchman 2000; Kay et al. 2002; Kawata & Gibson 2003; Sommer-Larsen et al. 2003; Springel & Hernquist 2003a; Brook et al. 2004; Oppenheimer & Davé 2006; Stinson et al. 2006; Dubois & Teyssier 2008; Dalla Vecchia & Schaye 2008; Okamoto et al. 2010; Piontek & Steinmetz 2011; Dalla Vecchia & Schaye 2012; Stinson et al. 2013), and more recently also AGN feedback (e.g., Springel et al. 2005b; Kawata & Gibson 2005; Di Matteo et al. 2005; Thacker et al. 2006; Sijacki & Springel 2006; Sijacki et al. 2007; Di Matteo et al. 2008; Okamoto et al. 2008; Booth & Schaye 2009; Kurosawa & Proga 2009; Teyssier et al. 2011; Debuhr et al. 2011; Dubois et al. 2012).

In a recent series of papers (Vogelsberger et al. 2012; Kereš et al. 2012; Sijacki et al. 2012; Torrey et al. 2012; Nelson et al. 2013; Bird et al. 2013) we have demonstrated that a moving mesh approach as implemented in the AREPO code (Springel 2010) provides a promising numerical method for performing galaxy formation calculations. Indeed, such a scheme combines most of the advantages of previous Eulerian and pseudo-Lagrangian techniques used in the field while avoiding many of their weaknesses. We therefore concluded in our previous work that the quasi-Lagrangian finite volume scheme of AREPO is well-suited for reliably solving the hydrodynamical equations posed by the galaxy formation problem. However, the simulations presented in Vogelsberger et al. (2012) accounted for only a rather limited set of physical processes in order to simplify comparisons with earlier numerical approaches. Most importantly, they did not include any form of explicit stellar feedback and also did not account for feedback from active galactic nuclei (AGN). But it has become clear over the last decade that both forms of feedback are crucial for shaping, for example, the stellar mass function. The stellar mass function may be viewed as a convolution of the underlying DM halo mass function with the efficiency with which stars form in these haloes (Springel & Hernquist 2003b). Stellar feedback regulates star formation in low mass haloes, since their potential wells are sufficiently shallow such that energy supplied through supernovae can remove gas efficiently from the galaxy, yielding galactic winds and outflows. For more massive systems, this channel of feedback becomes in-

efficient. However, as was realised already many years ago, AGN feedback from black holes (BH) can supply sufficient energy to quench star formation in these more massive systems. A combination of both feedback channels is the leading theoretical conjecture to explain the observed stellar mass function in the local Universe.

Besides these feedback mechanisms other physical processes are known to be important but were not included in our first moving-mesh simulations of galaxy formation presented in Vogelsberger et al. (2012). In particular, these simulations considered cooling processes only through a primordial mixture of hydrogen and helium. But evolving and dying stars release significant amounts of heavier elements, which leads to an important source of additional atomic line cooling once these metals are mixed with ambient gas. Stellar evolution processes also lead to gas recycling such that baryonic matter is not completely locked up in stars in a permanent fashion; rather it is returned at some rate to the gas phase, even by old stellar populations. Both metal line cooling and gas recycling elevate the supply of cold gas to galaxies and hence tend to increase the star formation rates in these systems.

In this paper, we present a new implementation of galaxy formation physics in the moving code AREPO, suitable for large-scale hydrodynamical simulations of structure formation. Our goal is to account for all primary physical processes that are known to be crucial for shaping the galaxy population. While we aim to be reasonably comprehensive in this endeavour, we note that it is clear that we cannot be fully complete in this first installment of our model. For example, we neglect some “non-standard” physics that has been proposed to influence galaxy formation, such as cosmic rays and magnetic fields. Besides presenting our implementation we also demonstrate how different feedback effects influence properties of galaxies and how the simulated galaxy population compares to current observations. We also identify the physical parameters of a fiducial reference model that leads to reasonable agreement with many key observables.

This paper is organised as follows. In Section 2, we present our galaxy formation model. Analysis and post-processing techniques that we have implemented in AREPO are described in Section 3. The first cosmological simulations using the newly added physics, and a comparison to different observational datasets, are discussed in Section 4. Here we also explore different feedback settings and introduce a fiducial reference model which provides a good fit to a set of important key observations. Finally, we give our conclusions and summary in Section 5 of the paper.

## 2 GALAXY FORMATION MODEL

In the following subsections we describe the physics implementation of our galaxy formation model. We first give a very brief description of our numerical scheme for solving the hydrodynamical equations. We then present our sub-resolution model for star formation followed by a discussion of our stellar evolution model. Next we discuss our approach for handling gas cooling. Finally, the second half of this section covers our methods for including black holes and feedback processes (stellar and AGN).

### 2.1 Hydrodynamical method

Most previous hydrodynamical simulations of galaxy formation have employed the smoothed particle hydrodynamics (SPH) technique (Lucy 1977; Gingold & Monaghan 1977; Monaghan 1992, 2005), where gas is discretised into a set of particles for which

appropriate equations of motion can be derived. The SPH method is well-suited for cosmological applications owing to its pseudo-Lagrangian character that automatically adjusts its resolution when structures collapse gravitationally. Furthermore, SPH manifestly conserves energy, momentum, mass, entropy *and* angular momentum, a feature unmatched by competing techniques.<sup>1</sup> Other methods for solving the equations of hydrodynamics in a cosmological context have been employed as well, most of which are descendants of classic Eulerian methods (Stone & Norman 1992) implemented as adaptive mesh refinement (AMR) codes (Berger & Colella 1989; Teyssier 2002; O’Shea et al. 2004). Several studies have however pointed out that these widely used schemes can lead to significant differences in the results for galaxy formation (e.g., Frenk et al. 1999; Agertz et al. 2007; Mitchell et al. 2009).

In this paper, we use a new numerical approach where a moving-mesh is used to solve the hydrodynamical equations (the AREPO code, Springel 2010), based on a quasi-Lagrangian finite volume method. The primary motivation is similar to earlier implementations of moving meshes by Gnedin (1995) and Pen (1998), but our method avoids the mesh-twisting problems that troubled these first attempts. To this end, AREPO employs an unstructured Voronoi tessellation of the computational domain. The mesh-generating points of this tessellation are allowed to move freely, offering significant flexibility for representing the geometry of the flow. This mesh is then used to solve the equations of ideal hydrodynamics with a finite volume approach using a second-order unsplit Godunov scheme with an exact Riemann solver. This technique avoids several of the weaknesses of the SPH and AMR methods while retaining their most important advantages (see the detailed discussion in Springel 2010; Vogelsberger et al. 2012; Kereš et al. 2012; Torrey et al. 2012; Sijacki et al. 2012). We note that a number of SPH extensions were proposed, which solve some of the defects of standard SPH (e.g., Price 2008; Wadsley et al. 2008; Cullen & Dehnen 2010; Abel 2011; Read & Hayfield 2012; Saitoh & Makino 2013).

## 2.2 Star formation

Owing to the limited resolution in large-scale structure simulations, we must treat the star-forming interstellar medium (ISM) in a sub-resolution fashion. Here we follow Springel & Hernquist (2003a) and model the star-forming dense ISM gas using an effective equation of state (eEOS), where stars form stochastically above a gas density of  $\rho_{\text{sfr}}$  with a star formation time scale of  $t_{\text{sfr}}$ . Such an approach for simulations with an unresolved ISM structure is very common (e.g., Ascasibar et al. 2002; Springel & Hernquist 2003a; Springel et al. 2005a; Robertson et al. 2006; Schaye & Dalla Vecchia 2008; Dubois & Teyssier 2008; Hopkins et al. 2008, 2009a,b; Few et al. 2012). The idea behind the use of an eEOS is that the ISM is believed to be governed by small-scale effects like supersonic turbulence, thermal instability, thermal conduction, and molecular cloud formation and evaporation processes. The combination of these processes is believed to quickly establish a self-regulated

<sup>1</sup> We note, however, that simultaneous conservation of entropy (for adiabatic flows) and energy are not automatically guaranteed if SPH smoothing lengths are adaptive (Hernquist 1993). This can be achieved, in general, only if the equations of motion are derived using a variational principle (Springel & Hernquist 2002; Hopkins 2013), which is not the case for many popular SPH codes.

equilibrium state of the ISM. In that regime, the average ISM temperature may be approximated as a function of density only.

We introduce a few modifications of the original Springel & Hernquist (2003a) implementation. First, to seamlessly connect to our stellar evolution model (see below) we use a Chabrier (2003) initial mass function (IMF) instead of the Salpeter IMF. Note that this also implies a larger supernovae type II (SNII) energy input in the ISM per formed solar mass of stars. Second, we take stellar mass loss processes into account when deriving the star formation rate based on the cold gas fraction in the ISM. Third, we prevent cells from being star-forming (both in terms of their star-formation rate, and of the effective equation of state) if their temperature is above the temperature corresponding to the effective equation of state at their density. This prevents spurious star-formation in diffuse hot gaseous haloes. Fourth, for determining the temperature of star-forming gas, we interpolate between the full Springel & Hernquist (2003a) eEOS and an isothermal EOS at  $10^4$  K with an interpolation parameter  $q_{\text{EOS}} = 0.3$ , which avoids an over-pressurisation of the ISM (Springel et al. 2005b; Hopkins & Quataert 2010). We did not incorporate metal dependent density thresholds nor did we take into account metal cooling within the two-phase model. Although adopting this would be straightforward, these effects do not lead to any significant changes in the functionality of our model, hence we ignore them here in order to keep the model as simple as possible. The adopted parameter choices for our star formation model are  $\rho_{\text{sfr}} = 0.13 \text{ cm}^{-3}$  and  $t_{\text{sfr}} = 2.2 \text{ Gyr}$ , in the notation of Springel & Hernquist (2003a). Our ISM sub-resolution model alone, by construction, does not drive galactic winds. We will discuss this below in more detail and present a model for the explicit generation of galactic outflows.

We note that once the numerical resolution is sufficient to resolve all the relevant ISM phases and processes, an eEOS is in principle not necessary anymore. In this case, a direct modelling of the relevant physical ISM processes, like momentum/energy injection and radiation pressure associated with star formation, is expected to lead to a turbulent and self-regulated quasi-equilibrium structure of the ISM. Impressive progress in this direction has recently been achieved (e.g. Hopkins et al. 2012b,d). However, we point out that the resolution requirements for such an approach are significantly beyond what is currently feasible in large-scale cosmological simulations, hence this is applicable only in “zoom-in” simulations of individual galaxies of low to moderate mass or in idealised simulations of isolated galaxies (Hopkins et al. 2012a, 2013a,b). In a forthcoming study (Marinacci et al., in prep), we will present a much more detailed ISM prescription on top of the other physics implementations discussed below.

## 2.3 Stellar evolution and chemical enrichment

Elemental abundance patterns are an important diagnostic tool for galaxy formation. Cosmological simulations track the evolution of baryons as they fall into galaxies, form stars, and are recycled back into the ISM. Including estimates for the recycling of material from aging stellar populations is important because it plays a central role in determining the evolution of a galaxy’s gas content and because the metal-rich ejecta from evolved stars determine its heavy element content.

Handling the mass and metal return from massive stars can be well-approximated by assuming instantaneous massive star evolution, which is implemented by lowering the effective star formation rate while the metal content of nearby gas is increased to account for metal production (e.g., Steinmetz & Mueller 1994; Springel &

Hernquist 2003a). This instantaneous recycling approach is justified for massive stars because they have relatively short lifetimes ( $\lesssim 10^7$  yr). However, an instantaneous recycling model cannot be accurately applied to intermediate mass stars, as the timescale for stellar evolution, and therefore the timescale for mass return, is comparable to or larger than galactic dynamical times. Most notably, asymptotic giant branch (AGB) stars return a substantial fraction of their mass to the ISM over expected lifetimes that can exceed  $10^9$  yr. Similarly, Type Ia supernovae explode with substantial delay times and, although they do not return a very large amount of mass to the ISM, they produce substantial quantities of iron. This gives rise to a situation where both the mass return rate and the elemental composition of the returned material will change as a function of time, depending on which mechanisms are operating.

A more general enrichment approach can be developed by tracking the mass and metal return of a stellar population to the ISM as a function of time (e.g., Mosconi et al. 2001; Lia et al. 2002; Kobayashi 2004; Scannapieco et al. 2005; Tornatore et al. 2007; Oppenheimer & Davé 2008; Wiersma et al. 2009b; Few et al. 2012). In our model, we integrate the time evolution of stellar particles to determine their mass loss and chemical enrichment as a continuous function of time. We use information from stellar evolution calculations to determine the expected main sequence lifetime, mass return fraction, and heavy element production for a wide range of initial stellar masses and metallicities. As a result, our model calculates not only the appropriate time-delayed mass loss rate, but also the chemical composition of the mass loss to the ISM. In the following, we briefly outline our scheme, which is similar to the implementation presented in Wiersma et al. (2009b).

### 2.3.1 Stellar evolution

We assume that each star particle in our simulations is a single-age stellar population (SSP) that represents a collection of discrete stars all born at the same time  $t_0$ . The distribution of stellar masses contained in each SSP is described by an initial mass function (IMF)  $\Phi(m)$  such that the integral of the IMF is equal to the mass of a star particle at its birth time,

$$M_*(t = t_0) = \int_0^\infty m \Phi(m) dm. \quad (1)$$

We further assume that the post main sequence evolution of stars is instantaneous. This assumption is justified because all stars have post main sequence evolutionary timescales that are typically  $\lesssim 1/10$  of their total lifetime. All stars within each SSP have thus a well-defined lifetime after which they instantly return some fraction of their mass and metals to the ISM. We keep track of the expected lifetimes using the stellar lifetime function  $\tau(m, Z)$ , which specifies the lifetime of stars on the main sequence as a function of their initial mass  $m$  and metallicity  $Z$ . We can invert this function to obtain the inverted lifetime function  $\mathcal{M}(t = t_0 + \tau, Z)$ , which gives the mass of stars that are moving off the main sequence at time  $t$ . Using the inverted lifetime function in conjunction with a chosen IMF, we can find the mass of stars evolving off the main sequence during any time step  $\Delta t$ ,

$$\Delta M(t, \Delta t, Z) = \int_{\mathcal{M}(t+\Delta t, Z)}^{\mathcal{M}(t, Z)} m \Phi(m) dm. \quad (2)$$

In our fiducial model, we choose a Chabrier (2003) IMF of the form

$$\Phi(m) = \begin{cases} A m^{-1} \exp\left(-\frac{\log(m/m_c)^2}{2\sigma^2}\right) & , m \leq 1 M_\odot \\ B m^{-2.3} & , m > 1 M_\odot \end{cases} \quad (3)$$

where  $m_c = 0.079$ ,  $\sigma = 0.69$ , and  $A = 0.852464$  and  $B = 0.237912$  are normalisation coefficients constrained to yield a continuous function at the transition mass scale. We note that our IMF choice influences the total mass returned to the ISM (e.g., Leitner & Kravtsov 2011) through the relative fraction of stars at the high and low mass ends. Using a different IMF would involve a trivial change to our model. For convenience, we have chosen the Chabrier (2003) IMF because it provides a reasonable fit to observational data both in our Galaxy and in nearby early-type galaxies for which detailed dynamical data are available (e.g., Cappellari et al. 2006). For the normalisation of the IMF according to equation (1) we apply a lower mass limit of  $0.1 M_\odot$  and an upper limit of  $100 M_\odot$ . We note that there is also the possibility of a varying IMF (e.g. Conroy & van Dokkum 2012).

We adopt the lifetime function from Portinari et al. (1998), which gives the expected stellar lifetimes as a function of initial stellar mass and metallicity. These lifetimes are calculated as the sum of the hydrogen and helium burning timescales for stars as a function of mass and metallicity.

### 2.3.2 Mass and metal return

To calculate the stellar mass loss of SSPs, we define the stellar recycling fraction  $f_{\text{rec}}(m, Z)$ , which indicates the total fraction of a star's initial mass that is recycled to the ISM over its entire lifetime. The dominant source of recycled material will change as a function of stellar mass  $m$  and metallicity  $Z$ . While the most massive stars ( $m > 13 M_\odot$ ) will return most of their mass in core collapse supernovae, less massive stars return their mass via AGB winds. Regardless of the source, we can calculate the amount of mass returned to the ISM  $\Delta M_{\text{rec}}$  during a time step in our simulation as

$$\Delta M_{\text{rec}}(t, \Delta t, Z) = \int_{\mathcal{M}(t+\Delta t)}^{\mathcal{M}(t)} m f_{\text{rec}}(m, Z) \Phi(m) dm. \quad (4)$$

Besides the total mass return we also track the return and production of individual chemical elements. If we denote the initial mass fraction of each element as  $Z_i$ , such that  $\sum_i Z_i = 1$ , where  $i$  is a sum over all elements (including hydrogen, helium, and all metals), then the mass of element  $i$  that is ejected from an unenriched stellar population during a simulation time step is given by

$$\Delta M_i(t, \Delta t, Z) = Z_i \int_{\mathcal{M}(t+\Delta t)}^{\mathcal{M}(t)} m f_{\text{rec}}(m, Z) \Phi(m) dm. \quad (5)$$

In the absence of chemical enrichment, the composition of the returned material is, by construction, identical to the initial metallicity of the star, independent of our choice for the returned mass fraction or IMF.

To include chemical enrichment, we must have some knowledge about the production or destruction of each element. We achieve this by using elemental mass yields  $y_i(m, Z)$  that specify the amount of mass created or destroyed for each element  $i$ , and each initial stellar mass  $m$  and initial metallicity  $Z$ . By definition, the yield for each element is

$$y_i(m, Z) = M_{i,\text{enrich}}(m, Z) - m Z_i f_{\text{rec}}(m, Z), \quad (6)$$

where  $M_{i,\text{enrich}}(m, Z)$  is the total mass of element  $i$  that is returned to the ISM. We note that the purpose of the mass yield is to track the transfer of mass between elements, not to create or destroy mass. As such, the production of one element must come at the expense of the destruction of another element such that  $\sum_i y_i = 0$ . We tabulate the elemental mass yields and incorporate them into our simulations via lookup tables. Using equations (4) and (6) we calculate the mass return as

$$\Delta M_i(t, \Delta t, Z) = \int_{\mathcal{M}(t+\Delta t)}^{\mathcal{M}(t)} (y_i + m Z_i f_{\text{rec}}(m, Z)) \Phi(m) dm. \quad (7)$$

Equation (7) is used to determine the mass return for each element at each time step so that we can physically transfer the proper elemental abundances from stellar particles to ISM cells. In our fiducial model we track nine chemical elements: H, He, C, N, O, Ne, Mg, Si, Fe.

We use the elemental mass yields for AGB stars from Karakas (2010), which are calculated by dynamically evolving the thermally pulsating AGB stars and then inferring the nucleosynthetic yields using a full reaction network over a wide range in metallicity ( $0.0001 < Z < 0.02$ ) and initial stellar masses ( $1 M_\odot < M < 6 M_\odot$ ). We adopt the elemental mass yields for core collapse supernova from Portinari et al. (1998), which are calculated using the Padova stellar evolutionary tracks in conjunction with the explosive nucleosynthesis of Woosley & Weaver (1995). We also extract  $f_{\text{rec}}(m, Z)$  from these references.

### 2.3.3 Supernovae rates

The majority of a stellar population's mass loss and metal production comes from AGB stars or core collapse supernovae. However, Type Ia supernovae are also important to consider because they produce a substantial amount of iron. Besides, the Type Ia supernova rate is crucial for cosmological studies.

The progenitor systems of Type Ia supernovae are still uncertain. The two most commonly discussed progenitor channels are the single degenerate scenario, where a Type Ia supernova results from a white dwarf accreting material from a companion star, and the double degenerate scenario, where a Type Ia supernova results from the merging of two white dwarf stars. In the standard single degenerate scenario, nearly all Type Ia progenitors will have the same mass and will be comprised mostly of carbon and oxygen. Since the conditions leading to a Type Ia event are comparatively well-posed in this picture, the chemical yields expected in each Type Ia supernova have been calculated (e.g., Thielemann et al. 2003).

What remains nevertheless highly uncertain even in this scenario is the rate we expect for Type Ia events after the birth of an SSP. In contrast, determining the expected number and rate of AGB stars and core collapse supernovae is relatively straightforward once we have made a choice for the IMF and lifetime functions. This is because we expect that all stars of a given mass will end their lives in the same way (e.g., we assume all  $20 M_\odot$  stars end as core collapse supernovae). The same simple logic cannot be applied to Type Ia supernovae because of the uncertainty that exists about their progenitor systems and the long time delay between the birth of a star and its eventual explosion in a Type Ia event. Our lack of a precise knowledge about the true form of the IMF, stellar binary fractions, and Type Ia progenitor systems prevents us from implementing a first-principles based model for Type Ia supernova rates.

Instead, a simple parameterisation of the Type Ia rate based on

the delay time distribution (DTD) of Type Ia events (e.g., Dahlen et al. 2004; Strolger 2004; Greggio 2005; Mannucci et al. 2006; Matteucci et al. 2006) is often adopted. In this formalism, the global Type Ia rate is determined by a convolution of the star formation rate with the DTD,

$$\dot{N}_{\text{Ia}}(t) = \int_0^t \Psi(t') g(t-t') dt', \quad (8)$$

where  $\Psi(t)$  is the star formation rate, and  $g(t)$  is the DTD. For a single SSP, the star formation history is a delta function centred on the stellar population's birth time, which gives a simplified Type Ia rate  $\dot{N}_{\text{Ia}}(t) = g(t-t_0)$ . Once the DTD is specified, we can calculate the number of SNIa events for  $t > t_0$  in a given time step by

$$N_{\text{Ia}}(t, \Delta t) = \int_t^{t+\Delta t} \dot{N}_{\text{Ia}}(t') dt' = \int_t^{t+\Delta t} g(t'-t_0) dt'. \quad (9)$$

Note that this does not require any explicit assumptions about the progenitors of Type Ia events, the form of the IMF, or the stellar binary fraction. All this information is implicitly contained in the DTD. Based on the number of SNIa events in a time step for a given SSP, we can calculate the returned mass and elements simply by multiplying this number by the corresponding yields per SNIa, as discussed above. Unfortunately, the exact form of the DTD is still poorly constrained. In the following, we will use a DTD model which consists of a power law in time,

$$g(t) = \begin{cases} 0 & \text{if } t < \tau_{8M_\odot} \\ N_0 \left( \frac{t}{\tau_{8M_\odot}} \right)^{-s} \frac{s-1}{\tau_{8M_\odot}} & \text{if } t \geq \tau_{8M_\odot}, \end{cases} \quad (10)$$

where  $s$  is the power law index and  $\tau_{8M_\odot}$  is an offset time between the birth of the SSP and the first expected Ia event. We take  $s = 1.12$  as the fiducial value (Maoz et al. 2012), which is consistent with theoretical expectations that relate the Type Ia rate to the loss of energy and angular momentum to gravitational radiation in a binary system (e.g., Greggio 2005). Furthermore, we take  $\tau_{8M_\odot} = 40 \text{ Myr}$ , corresponding to the main sequence lifetime of  $\sim 8 M_\odot$  stars, which we assume to be the upper mass limit for progenitors of Ia events. For the normalisation we adopt  $N_0 = 1.3 \times 10^{-3} [\text{SN } M_\odot^{-1}]$  (Dahlen et al. 2004; Maoz et al. 2012).

With the Type Ia supernova rate specified, determining the mass return and metal production is easily done using the yield calculations of Thielemann et al. (2003) and Travaglio et al. (2004). Mass and metals produced in Type Ia events are then returned to the ISM in the same fashion as for core collapse supernovae and AGB winds. We have checked that the exact choice of the DTD (e.g., power law vs. exponential) does not affect most of our results in any significant way. The reason for this is that the SNIa mainly affect the iron production, but they are not a significant source of stellar mass loss, which is dominated by stars in the AGB phase and SNII events.

We note that the number of SNII events in a given time step can be calculated based on the IMF

$$N_{\text{SNII}}(t, \Delta t) = \int_{\max[\mathcal{M}(t+\Delta t), M_{\text{SNII,min}}]}^{\min[\mathcal{M}(t), M_{\text{SNII,max}}]} \Phi(m) dm, \quad (11)$$

which is non-zero only if the integration interval is positive. In the following we set  $M_{\text{SNII,min}} = 6 M_\odot$  and  $M_{\text{SNII,max}} = 100 M_\odot$  as the mass range for stars ending in SNII.

### 2.3.4 Gas enrichment

For each active stellar particle we calculate the total mass, total metal mass and element return during its current time step following the scheme described above. These masses are then returned to the nearby Voronoi cells of the stellar particle, where we enforce momentum and energy conservation. We distribute the mass and metals over a set of nearest neighbouring cells using a top hat kernel enclosing a mass of approximately  $N_{\text{enrich}} \times m_{\text{target}}$ , where  $m_{\text{target}}$  is the cell target mass according to our (de-)refinement scheme (see below). For convergence studies we normally hold this ‘‘enrichment mass’’ fixed if we change resolution, which means that we scale  $N_{\text{enrich}}$  such that the change of the target mass with resolution is compensated. However, we find that using a constant  $N_{\text{enrich}}$  produces almost identical results.

## 2.4 Cooling and heating

Energy loss via radiative cooling is a key physical process for galaxy formation. Early cosmological hydrodynamical simulations (e.g., Katz et al. 1992, 1996) included cooling due to a primordial mixture of hydrogen and helium, where two-body processes (collisional excitation, collisional ionisation, recombination, dielectric recombination and free-free emission) and inverse Compton cooling off the CMB (e.g., Ikeuchi & Ostriker 1986) were considered. Furthermore, energy input due to photo-ionisation was injected as heat into the gas. Typically these simulations considered a spatially uniform, time-varying UVB radiation field. The presence of metals in the ISM and IGM due to enrichment processes changes the cooling rates by increasing the number of possible transitions. A primordial treatment is then not accurate anymore for such an enriched gas.

For high-temperature gas, Sutherland & Dopita (1993) published cooling rate tables for 14 heavy elements over a range of metallicities, using solar relative abundances. Their rates assume collisional ionisation equilibrium and do not include effects due to background radiation fields. However, it is important to include background radiation when calculating the cooling rates, because it affects both the thermal and ionisation state of the plasma (e.g., Efstathiou 1992; Gnedin & Hollon 2012) leading to a suppression of the cooling rate and increase of heating rates. Smith et al. (2008) introduced a table-based method to include metal line cooling, accounting for photo-ionisation due to the UVB. Their technique involves the use of the photo-ionisation code CLOUDY to construct a lookup table of metal cooling rates. This approach was also followed in other studies; e.g. Wiersma et al. (2009a) even considered the cooling contribution from individual elements.

We adopt a spatially uniform time-dependent UVB and also implement metal-line cooling in AREPO based on CLOUDY cooling tables. We assume ionisation equilibrium such that we can calculate cooling rates a priori for a given portion of dust-free and optically thin gas, for a given background radiation field. We still carry out a self-consistent calculation of the primordial cooling following Katz et al. (1996), on top of which we add the cooling contribution of the metals. In principle, the metal-line cooling can be implemented on an element-by-element basis once the main coolants are tracked by the enrichment scheme. Wiersma et al. (2009a) showed that it is sufficient to follow 11 elements (H, He, C, N, O, Ne, Mg, Si, S, Ca, Fe) to recover the main metal line cooling contribution. Although most of these elements are explicitly followed by our chemical enrichment model, we decided not to implement cooling on an element-by-element basis in our default setup because: (i) individ-

ual element yields have large uncertainties, and element-wise cooling would directly couple those into the hydrodynamical evolution via the cooling contribution; (ii) departures of the relative abundances from solar lead only to small corrections compared to the overall photo-ionisation modification (see Wiersma et al. 2009a, for example); and (iii) the computational overhead for evaluating the cooling rate scales directly with the number of elements used in the cooling. We base our implementation of metal-line cooling therefore on the rates for a solar composition gas, and these rates are scaled linearly with the total metallicity  $Z$ .

The total net cooling rate in the simulation is then evaluated based on

$$\Lambda(T, \rho, z, Z) = \Lambda_{\text{p}}(T, \rho, z) + \frac{Z}{Z_{\odot}} \Lambda_{\text{m}}(T, \rho, z, Z_{\odot}) + \Lambda_{\text{C}}(T, \rho, z). \quad (12)$$

Here  $\Lambda_{\text{p}}$  is the net cooling contribution due to primordial species (H,  $\text{H}^+$ , He,  $\text{He}^+$ ,  $\text{He}^{++}$ ),  $\Lambda_{\text{m}}$  is the net cooling contribution due to metals, and  $\Lambda_{\text{C}}$  represents Compton cooling off the CMB. The primordial cooling and heating is calculated directly from ionisation equations using the cooling, recombination and collisional ionisation rates from Cen (1992); Katz et al. (1996). Photoionisation rates, which affect abundances and inject energy into the gas, are calculated based on the UVB intensity of Faucher-Giguère et al. (2009). This ionising background has contributions from both quasars and star-forming galaxies, with the latter dominating at approximately  $z > 3$ . In addition to being compatible with recent luminosity functions, the model was calibrated to satisfy the measured mean transmission of the Ly-alpha forest at intermediate redshifts  $z = 2 - 4.2$  (Faucher-Giguère et al. 2008a,b), published HeII to HI column density ratios, HeII reionisation by  $z \sim 3$  (McQuinn et al. 2009), and complete HI reionisation by  $z = 6$ . We use the spectra from the same background as an input to CLOUDY to calculate matching metal line cooling rates  $\Lambda_{\text{m}}$ .

For simplicity we neglect the metal contribution to the mean molecular weight  $\mu$ ; i.e. we calculate temperatures based on the molecular weight corresponding to the ionisation state of the primordial gas composition. This is well-justified since in a fully ionised metal enriched plasma of metallicity  $Z$  the mean molecular weight is approximately given by  $\mu \cong 4/(8X + 3Y + 2Z)$ , such that even at super-solar composition the metal contribution leads only to minor changes in  $\mu$  (see also Smith et al. 2008). We also neglect the metal contribution to the free electron density, which is also justified since those will only be relevant for  $Z \gg Z_{\odot}$  (e.g., Wiersma et al. 2009a). For solving the primordial network we use the advected H, He mass fractions as an input. Together with the spatially uniform but temporally varying UVB this gives us the primordial abundances and a self-consistent temperature based on  $\mu$ . With this temperature we calculate  $\Lambda_{\text{p}}$ , and look up  $\Lambda_{\text{m}}$  in the pre-calculated CLOUDY tables to arrive at the total cooling rate through Equation (12).

For the construction of the lookup tables, we tabulated metal line net cooling rates on a grid in  $\log(T/\text{K})$ ,  $\log(n_{\text{H}}/\text{cm}^{-3})$  and redshift:  $1 < \log(T/\text{K}) < 9$  at 200 equally spaced grid points,  $-8 < \log(n_{\text{H}}/\text{cm}^{-3}) < 2$  at 50 equally spaced grid points, and  $0 < z < 10$  at 50 grid points. During the simulation, we linearly interpolate the metal line cooling rates in  $[z, \log(n_{\text{H}}/\text{cm}^{-3}), \log(T/\text{K})]$  space.

### 2.4.1 Self-shielding

So far we described our treatment of cooling and heating in the presence of a spatially uniform UVB radiation under the assumption that the gas is optically thin to the radiation. However, this approximation breaks down at gas densities  $\rho \gtrsim 10^{-3} \text{ cm}^{-3}$ , depending on the details of the radiation field. Above such densities, the gas absorbs the radiation to such a degree that the radiation field is attenuated compared to the optically thin case. This modified radiation field in turn affects the heating rate and ionisation state, and hence the cooling rate, differently than the unattenuated radiation field. As a result, the equilibrium gas temperature ends up being different, and hence the dynamical evolution can be affected.

In order to approximately account for this effect, we implemented a simple prescription for the self-shielding of gas from the UVB radiation to be used on-the-fly, rather than only in post-processing as has been common practice (e.g., Bird et al. 2011). Our implementation is derived from the results of radiation transfer simulations by Rahmati et al. (2013), who post-processed cosmological simulations using the radiation transfer code TRAPHIC (Pawlik & Schaye 2008, 2011), and quantified the self-shielding of the intergalactic gas as a function of cosmological epoch and gas density. We implemented their Equation (A1) with the parameters given in their Table A1 both for the primordial network that is directly followed in our code, and for the CLOUDY calculations we use to generate the lookup table. Specifically, the ionisation and heating rates entering into the primordial network are suppressed by

$$(1-f) \left[ 1 + \left( \frac{n_{\text{H}}}{n_0} \right)^{\beta} \right]^{\alpha_1} + f \left[ 1 + \frac{n_{\text{H}}}{n_0} \right]^{\alpha_2}, \quad (13)$$

and the same factor is used to suppress the normalisation of the input radiation field that is given to the CLOUDY code, making the approximation that its spectrum is unchanged. The numerical values of the various parameters in the self-shielding formula ( $\alpha_1$ ,  $\alpha_2$ ,  $\beta$ ,  $f$ ,  $n_0$ ) are interpolated linearly in redshift  $z$  between the values provided in Table A1 of Rahmati et al. (2013), up to  $z = 6$ , above which we assume zero self-shielding. Finally, we note that the radiation field is not considered for star-forming gas, which is placed on the effective equation of state of the star-formation model.

## 2.5 Stellar feedback

Although our subgrid ISM model implicitly invokes thermal SNII feedback, this is not sufficient to avoid the well-known overcooling problem (e.g., Springel & Hernquist 2003a). Large-scale cosmological simulations therefore typically resort to some subgrid model for galactic winds and outflows, capable of efficiently removing baryonic material from the star-forming phase. Two approaches are typically followed in a regime of limited resolution: injection of SN energy in kinetic form (e.g., Navarro & White 1993; Mihos & Hernquist 1994; Kay et al. 2002; Springel & Hernquist 2003a; Oppenheimer & Davé 2006; Dubois & Teyssier 2008; Dalla Vecchia & Schaye 2008; Okamoto et al. 2010; Hopkins et al. 2012c) or suppression of radiative cooling after injection of thermal energy (e.g., Gerritsen & Icke 1997; Thacker & Couchman 2000; Kawata & Gibson 2003; Sommer-Larsen et al. 2003; Brook et al. 2004; Stinson et al. 2006; Piontek & Steinmetz 2011; Dalla Vecchia & Schaye 2012; Stinson et al. 2013).

The kinetic wind models are typically characterised by a mass loading factor  $\eta_w$ , which gives the ratio of the wind mass flux and

star formation rate, and an initial wind velocity  $v_w$ . In the original kinetic wind scheme of Springel & Hernquist (2003a), star-forming SPH particles are converted into wind particles stochastically. In order to allow a precise specification of the wind mass flux, the implementation ensured that wind particles can leave the dense ISM gas without entraining additional star-forming particles. In order to technically realise this sub-grid prescription, hydrodynamical interactions were temporarily disregarded for newly launched wind particles until they “recouple” just outside of the star-forming phase, based on a density threshold criterion. The mass loading and wind velocity in Springel & Hernquist (2003a) were chosen to be constant. More recent studies propose variable wind models, however, where the wind velocity is not held fixed. For example, Oppenheimer & Davé (2006) argue for momentum driven winds, where the wind speed scales as the galaxy velocity dispersion and the mass loading is inversely proportional to that (see also Murray et al. 2005). Such an approach appears to be supported by observations. Martin (2005) and Weiner et al. (2009) found that the final wind velocity scales approximately linearly with the circular velocity. Okamoto et al. (2010) use the local velocity dispersion of dark matter to prescribe the wind velocity, although they consider energy driven winds, which are generated locally around the stellar particles similar to the approach of Dalla Vecchia & Schaye (2008), which uses constant local winds. Puchwein & Springel (2013) reported a good match to the observed stellar mass function with an energy-driven variable wind model, where the wind velocity is derived from the escape velocity of the host halo.

We have implemented two alternative wind schemes in AREPO. Our basic approaches for modelling winds and outflows are similar to those presented in previous work (Springel & Hernquist 2003a; Oppenheimer & Davé 2006, 2008; Dalla Vecchia & Schaye 2008; Okamoto et al. 2010; Puchwein & Springel 2013), but our technical implementation is slightly different to account for our mesh-based hydro scheme. Also, we note that the overcooling problem tends to be more severe in AREPO compared to previous SPH studies (see Vogelsberger et al. 2012; Kereš et al. 2012, for details). The origin of this lies in part in the treatment of subsonic turbulence and in spurious viscous heating in SPH, which leads to an artificial heating of gaseous haloes in SPH simulations (Vogelsberger et al. 2012; Bauer & Springel 2012). This effect is strongest for massive haloes, and we will show below that our simulations require stronger AGN feedback because of this (see below).

### 2.5.1 Non-local SNII feedback

In our first stellar feedback implementation, which we call “non-local”, we launch winds directly from the star-forming ISM gas, which is part of the two-phase medium. This ties the wind rate directly to the star formation rate of star-forming gas. For large-scale simulations, the time steps are typically not much shorter than the SNII delay time; i.e. it is a valid approximation to neglect locality for SNII driven winds in that case.

We realise the generation of the wind at a technical level by turning gas cells (or a fraction of their mass) for a short period of time into massive wind particles which interact gravitationally but do not couple to the hydrodynamical calculation. For these non-local winds, we probabilistically select a star-forming ISM gas cell, which we then convert into a wind particle. This particle is then allowed to travel, decoupled from hydrodynamical forces, until it reaches a certain density threshold or a maximum travel time has elapsed. Once either of these criteria is fulfilled, we dissolve the particle and deposit its mass, momentum, thermal energy and all



tracked metals into the gas cell in which it is currently located. The net effect of this procedure mimics the sub-grid wind prescription of Springel & Hernquist (2003a) and facilitates a precise control of the wind parameters independent of numerical resolution. We note that Dalla Vecchia & Schaye (2008) demonstrated that decoupling wind particles can have an effect on the galaxy properties. However, a decoupled scheme gives better control over mass loadings and typically converges better, which is why we favour such an approach.

We set the mass loading and wind velocity based on the local DM velocity dispersion (similar to Oppenheimer & Davé 2008; Okamoto et al. 2010): to this end, each gas cell calculates the local one-dimensional DM velocity dispersion ( $\sigma_{\text{DM}}^{1D}$ ) at its current location, and the wind velocity is then set to

$$v_w = \kappa_w \sigma_{\text{DM}}^{1D}, \quad (14)$$

where  $\kappa_w$  is a dimensionless model parameter. Okamoto et al. (2010) found that the local velocity dispersion measured at the position of star forming gas strongly correlates with the maximum of the circular velocity profile of its host halo ( $V_{\text{max}} \simeq 1.45 \sigma_{\text{DM}}^{1D}$ ), which motivates such a wind velocity scaling.

Once the wind velocity is determined, the wind mass, given by the mass loading  $\eta_w$ , is determined by combining momentum and energy driven wind contributions

$$\eta_w = \frac{1}{v_w^2} \left( \text{egy}_w + \sqrt{\text{egy}_w^2 + v_w^2 \text{mom}_w^2} \right), \quad (15)$$

where  $\text{mom}_w$  is the specific wind momentum,  $\text{egy}_w$  is specific energy available for wind generation (available SNII energy per formed stellar mass). Both  $\text{mom}_w$  and  $\text{egy}_w$  are free parameters, which are motivated by the underlying driving mechanism of the winds. Equation 15 gives the asymptotic mass loading scalings  $\eta_w \propto v_w^{-2}$  for energy-driven, and  $\eta_w \propto v_w^{-1}$  for momentum-driven winds. This therefore represents an average mass loading with energy and momentum contributions, where the relative importance is regulated by  $\text{mom}_w$  and  $\text{egy}_w$ . For example, purely energy driven winds would be represented by  $\text{egy}_w = 1.73 \times 10^{-2} E_{\text{SNII},51} 10^{51} \text{ erg } M_{\odot}^{-1}$ , where  $E_{\text{SNII},51}$  denotes the available energy per SNII in units of  $10^{51} \text{ erg}$  and  $1.73 \times 10^{-2}$  is the number of SNII per stellar mass formed for our adopted stellar evolution model.

For the non-local ISM driven winds, star formation and the generation of wind particles are two different mechanisms that drain gas mass simultaneously from the ISM. It is therefore desirable to have a common treatment of the generation of stellar and/or wind particles in this case. Our solution is based on a unified equation for star-formation and wind generation

$$\frac{d}{dt}(M_* + M_w) = -\dot{M} = (1 + \eta_w)\Psi = (1 + \eta_w)\frac{M}{t_{\text{SF}}}, \quad (16)$$

where  $M$ ,  $M_*$  and  $M_w$  are the mass of a gas cell  $i$ , its associated stellar and wind mass, respectively. The quantity  $\Psi$  denotes the star formation rate which is determined by the star formation time scale  $t_{\text{SF}}$ . The solution of Equation (16) specifies the amount of stellar and wind material created during a time step of size  $\Delta t$  between  $t$  and  $t + \Delta t$

$$\begin{aligned} \Delta(M_* + M_w) &= (M_* + M_w)(t + \Delta t) - (M_* + M_w)(t) \\ &= M(t) - M(t + \Delta t) \\ &= M(t) \left( 1 - e^{-(1+\eta_w)\Delta t/t_{\text{SF}}} \right). \end{aligned} \quad (17)$$

At every time step  $\Delta t$ , for each active gas cell, we first make a

probabilistic decision whether star-formation or wind-launching is treated in that step. This is done by drawing a uniformly distributed random number  $x \in U(0, 1)$ . Then, star-formation is treated if  $x < 1/(1+\eta_w)$ , and wind-launching otherwise. This procedure ensures that the expectation value for the mass-loading factor of the wind; i.e. the ratio between the wind-launching rate and the star-formation rate, is exactly  $\eta_w$ . To avoid forming very large numbers of stellar or wind particles, Equation (16) is implemented stochastically (e.g., Springel & Hernquist 2003a). This is done by assigning a probability

$$p^{\text{gas} \rightarrow \text{stars/wind}} = \frac{M_i}{M_*} (1 - e^{-(1+\eta_w)\Delta t/t_{\text{SF}}}), \quad (18)$$

to generate a star or wind particle of mass  $M_*$ . We note that it is guaranteed that the correct amount of stellar mass (wind mass) is created because star-formation (wind-formation) is treated in only  $1/(1 + \eta_w)$  ( $\eta_w/(1 + \eta_w)$ ) of the time steps by the random decision described above. In Equation (18), the star particle mass  $M_*$  is determined in the following way: if  $M < 2m_{\text{target}}$ , we set  $M_* = M$  and the full cell is converted into a star particle, while if  $M \geq 2m_{\text{target}}$ , and the cell only spawns a star particle of mass  $m_{\text{target}}$ . As discussed above,  $m_{\text{target}}$  is the mean gas cell mass in the initial conditions, which plays the role of target gas cell mass in our (de-)refinement scheme. This procedure ensures that we avoid large mass variations among the baryonic cells and particles.

For choosing the wind direction, we implemented two commonly used approaches: isotropic and bipolar winds. For the isotropic case, each wind particle is kicked in a completely random direction. In the bipolar case, each wind particle is kicked, with a random sign, in the direction  $\mathbf{v} \times \nabla\phi$  (Springel & Hernquist 2003a) in the rest frame of the corresponding FoF group. Note that both schemes do not add total momentum on average. In the following we will only use the bipolar implementation.

### 2.5.2 Local SNII feedback

In the wind scheme described above, wind particles are launched from the ISM and are therefore not spawned directly from stellar particles. Although slightly inconsistent with our stellar evolution and enrichment model, where we use a delayed SNII return, this model works very well for cosmological applications because of the relevant time scales, as argued above. Nevertheless it is desirable to have the possibility of using a more local SNII feedback implementation for comparison. For example, Okamoto et al. (2010) use an energy-driven local stochastic scheme, where wind particles are launched in the neighbourhood of stellar particles. This approach is similar to the implementation of Dalla Vecchia & Schaye (2008) with the exception of the way in which ‘‘excess energy/mass loading’’ is handled. Another variation of this approach was presented in Dalla Vecchia & Schaye (2012).

To explore the effect of non-locality we implemented a wind creation scheme similar to that of Okamoto et al. (2010) for purely energy driven winds, whose velocity scales with the local DM velocity dispersion. Specifically, we modified our enrichment routines to also distribute SNII energy among the gas cells that receive metals and mass. During the enrichment step, each cell keeps track of how much energy it receives from stellar particles such that once the enrichment is finished, some cells have received the SNII energy  $\Delta E_{\text{SNII}}$ . Each of these cells is then assigned a probability  $p = \Delta E_{\text{SNII}}/(0.5Mv_w^2)$ , where  $M$  is the mass of the gas cell and  $v_w = \kappa_w\sigma$  is the wind velocity assigned to this particle. Based on this probability it is then decided whether this cell should be

converted to a wind particle. Once a cell is converted, it is treated exactly the same way as in the non-local case described above. We note that we do not require gas cells to be above the density threshold for star formation for this to happen.

To make contact with our non-local scheme, we can derive an effective mass loading. For this we follow Okamoto et al. (2010) and assume the instantaneous recycling approximation ( $\dot{M}_w = 2\dot{E}_w/v_w^2$ , where  $\dot{E}_w$  is the available energy flux for the wind generation) to derive

$$\eta_w = E_{\text{SNII},51} \left( \frac{v_w = \kappa_w \times \sigma_{\text{DM}}^{1D}}{1307 \text{ km s}^{-1}} \right)^{-2}, \quad (19)$$

where  $E_{\text{SNII},51}$  is the energy per SNII in units of  $10^{51}$  erg and we assumed  $1.73 \times 10^{-2}$  SNII per formed stellar mass, which are the appropriate values for a Chabrier (2003) IMF with the SNII mass limits discussed above.

### 2.5.3 Wind metal loading

Wind models with an energy or momentum scaling are the two most commonly applied wind parameterisations in the literature, and both rely on mass loading factors that decrease with galaxy mass. In fact, the mass loading factors associated with low mass galaxies can often be well in excess of unity, naturally indicating that low mass galaxies do not efficiently hold onto their gaseous content. Moreover, such high mass loading factors appear to be necessary for obtaining a reasonable shape for the galaxy stellar mass function (e.g., Davé et al. 2011b; Puchwein & Springel 2013). However, calculations of the metal content of low-mass galaxies based on their observed gas fractions and metallicities indicate that low mass galaxies nevertheless retain a substantial fraction of their metals (Zahid et al. 2012). Thus, there is a certain tension between the need to efficiently expel a lot of material to reduce the star formation efficiency in low mass galaxies, and the need to retain a sizable fraction of the metals in these same low-mass galaxies.

The origin of this tension lies in our construction of the sub-grid wind model. Traditionally, it is assumed that the wind particles have the same metallicity as the ambient ISM from where they are launched (e.g., Springel & Hernquist 2003a; Davé et al. 2011b). However, while the actual wind material will be partially composed of the material from the site where the wind is launched, a substantial fraction of the wind’s mass will be entrained as the wind vents out of the galaxy and blows through low density regions of the ISM. This suggests a picture where the metallicity of the wind material will almost certainly be different – and likely lower – than the metallicity of the ISM-region from where the wind originated.

To address this point, we introduce a wind metal loading factor  $\gamma_w$ , which is set independently from the wind mass loading factor,  $\eta_w$ . The wind metal loading factor defines the relationship between the metallicity of newly created wind particles  $Z_w$ , and the metallicity  $Z_{\text{ISM}}$  of the ambient ISM,

$$Z_w = \gamma_w Z_{\text{ISM}}. \quad (20)$$

The case  $\gamma_w = 1$  corresponds to the traditionally assumed scenario of “fully metal-loaded” winds. The opposite extreme is described by  $\gamma_w = 0$ , which assumes that winds carry no metals along with them. In this case, a created wind particle deposits all its metals in the surrounding ISM cells before being kicked, thereby ensuring conservation of total metal mass.

We found that the traditional  $\gamma_w = 1$  leads to an under-production of the gas-phase metallicity and an over enrichment

of halo gas, especially in low mass galaxies. Both of these problems directly result from an overly efficient ejection of metals from galaxies via winds. Not only does this lead to a poor match to the observationally constrained mass-metallicity relation, but the over enrichment of halo gas also leads to enhanced metal-line cooling. The other extreme, when using  $\gamma_w = 0$ , leads to overly enriched galaxy gas-phase metallicities compared to the mass-metallicity relations, suggesting that the correct behaviour is bracketed by these two extremes.

We note that wind metal loadings were recently discussed in Peeples & Shankar (2011), where it was argued that winds should actually be “super-enriched” such that their metallicity should be higher than the of the surrounding ISM gas. We note however that this conclusion was reached based on the very low mass loading factors discussed in Peeples & Shankar (2011), which then automatically require highly enriched winds to match the observed mass–metallicity relation. Such low mass loadings are however incompatible with results from cosmological simulations; the latter require rather much higher mass loadings for low mass systems to match the stellar mass function (see below).

## 2.6 Black hole growth and AGN feedback

As with star formation, it is currently computationally impossible to resolve the details of accretion flows around central galactic black holes (BHs) in large-scale simulations of galaxy formation. While the gravitational radius of supermassive black holes starts to be resolved in zoom-in simulations, the Schwarzschild radius of these BHs is still many orders of magnitude smaller than the spatial resolution limits of these calculations. Describing BH growth and related feedback therefore requires a sub-resolution model (e.g. Springel et al. 2005b; Kawata & Gibson 2005; Di Matteo et al. 2005; Thacker et al. 2006; Sijacki et al. 2007; Di Matteo et al. 2008; Okamoto et al. 2008; Booth & Schaye 2009; Kurosawa & Proga 2009; Teyssier et al. 2011; Debuhr et al. 2011; Dubois et al. 2012). Our BH and AGN feedback implementation follows closely previous studies (Springel et al. 2005b; Di Matteo et al. 2005; Sijacki et al. 2007; Di Matteo et al. 2008), with modifications to adopt the scheme to the moving mesh and finite volume technique. In what follows, BHs are represented by collisionless, massive sink particles that are created at early times, and subsequently grow in mass by gas accretion or BH mergers. We include three different forms of back-reaction of the accretion: thermal, mechanical and electromagnetic feedback. Thermal and mechanical feedback have already been considered in some previous large-scale cosmological simulations, whereas electro-magnetic radiative feedback has typically been neglected (except for a few cases, see below). We here present a novel phenomenological treatment of this form of feedback.

### 2.6.1 Black hole seeding

Our seeding strategy for BHs in cosmological simulations follows previous work. We regularly run a FoF group finder and assign seed BHs to massive enough FoF groups (see Sijacki et al. 2007; Di Matteo et al. 2008, for details). We set the seeding mass threshold for FoF groups to  $5 \times 10^{10} h^{-1} M_\odot$ . For a FoF group that is selected to acquire a seed BH, we turn the gas cell with the highest density in the group into a BH sink particle. The dynamical mass of the particle is set to the cell mass. This dynamical mass is typically significantly higher than the real expected seed mass of the BH, which we set in the following to  $10^5 h^{-1} M_\odot$ , as in many previous

studies. To address this problem, we follow Springel et al. (2005b) and track the BH mass as a separate subgrid variable. This internal BH mass smoothly increases according to the estimated BH accretion rate  $\dot{M}_{\text{BH}}$  (see below), such that the value of this internal mass represents the BH mass for the case where accretion can be fully resolved and mass is not discretised.

We allow the BH sink particle to drain mass continuously from the primary cell of the BH particle. Specifically, during each time step, an active BH particle removes the mass  $\Delta M = (1 - \epsilon_r) M_{\text{BH}} \Delta t$  from its primary cell, where  $\Delta t$  is the current time step and  $\epsilon_r$  radiative efficiency (see below). BH accretion rates are typically very small compared to the actual cell masses of the primary cell such that  $\Delta M$  is usually significantly smaller than the mass of the primary cell. In the rare event that this is not the case, we added a ‘‘bucket mechanism’’ which collects  $\Delta M$  in an accretion mass bucket to be then handled with a small time delay. During subsequent time steps, this bucket is then emptied such that we always accrete the correct amount of mass. Specifically, if  $\Delta M$  is larger than 90% of the primary cell mass, we remove these 90% of the cell mass and put the remaining mass of  $\Delta M$  into the bucket. During the next accretion event of the BH we then try to remove the current  $\Delta M$  from the cell plus the mass that is currently in the bucket. Here again, we allow at maximum a removal of 90% of the cell mass. This procedure guarantees a continuous accretion scheme, where the internal and dynamical masses of the BH particles grow at the same rate, which is different from the original stochastic accretion implementation used in previous SPH studies of this model (Springel et al. 2005b). We note that the draining scheme does not change the real dynamical mass of BH sink particles until the internal mass is equal to or larger than the initially assigned dynamical mass. Also, only at that point do we actually really drain mass from the primary cell, thereby maintaining mass conservation during the whole evolution.

### 2.6.2 Black hole growth

BH sink particles grow in mass by accreting surrounding gas or through BH mergers. In our model, BH accretion is described using a Bondi-Hoyle-Lyttleton based Eddington-limited rate

$$\dot{M}_{\text{BH}} = \min \left[ \frac{4\pi\alpha G^2 M_{\text{BH}}^2 \rho}{(c_s^2 + v_{\text{BH}}^2)^{3/2}}, \dot{M}_{\text{Edd}} \right], \quad (21)$$

where  $\rho$  and  $c_s$  are density and sound speed of the surrounding gas, respectively, and  $v_{\text{BH}}$  is the BH velocity relative to the gas.  $\dot{M}_{\text{Edd}}$  denotes the Eddington accretion rate of the BH. In the following we will usually use a repositioning scheme for BH sink particles that ties them to the minimum of the gravitational potential, in which case we will neglect the relative gas velocity term ( $v_{\text{BH}}$ ) in the accretion rate. The repositioning ensures that BHs stay at the centre of their haloes (FoF groups), which is important to guarantee their correct growth rate. Note that because of the relatively coarse mass resolution available for dark matter and stars, the BHs would not by themselves sink to the centre on the correct timescale. But the repositioning implies that the velocity of the BH sink particle is unphysical, such that we do not consider it in the accretion rate. Due to our feedback implementation the sound speed ( $c_s$ ) near BHs is typically significantly higher than the relative BH – gas velocity such that this does not introduce any relevant effects. As in previous studies we multiply the theoretical Bondi-Hoyle-Lyttleton accretion rate by a factor  $\alpha$  to approximately account for the volume-average of the Bondi-rates for the cold and hot phases of the subgrid ISM model.

However, when no star-forming gas is present in the immediate vicinity of the BH (and the quasar accretion is hence in a ‘‘low state’’), this prescription is expected to significantly overestimate the true accretion rate. In particular, this will happen when the BH has grown to a large mass and is embedded in comparatively low density background gas. Then the residual BH accretion we estimate with equation (21), together with our quasar-mode feedback scheme (see below), can create a hot, low-density bubble around the black hole, with a pressure that matches the background gas pressure  $P_{\text{ext}}$  at the centre of the halo. The formation of such a bubble with density well below the star-formation density threshold would clearly be an unrealistic artifact of our subgrid model. We address this as follows.

First, we note that if a quasar-heated bubble in a quasi-stationary state forms, we expect that the cooling losses in the bubble will approximately balance the injected feedback energy from the quasar mode

$$\Lambda(T) \rho M_{\text{fb}} \simeq \epsilon_f \epsilon_r \frac{4\pi\alpha G^2 M_{\text{BH}}^2 \rho}{c_s^3} c^2. \quad (22)$$

Here  $M_{\text{fb}}$  is the gas mass in the bubble (which is equal to the amount of material that receives the feedback energy), and  $\Lambda(T)$  is the cooling function. The product  $\epsilon_f \epsilon_r$  specifies the quasar-mode feedback strength (see below). Neglecting metallicity effects for the moment, this equation describes an equilibrium temperature  $T_{\text{eq}}$  for the bubble (or equivalently a thermal energy  $u_{\text{eq}}$  per unit mass) which depends only on the black hole mass, because the density dependence drops out. We use this temperature to define a reference pressure

$$P_{\text{ref}} = (\gamma - 1) \rho_{\text{sfr}} u_{\text{eq}}, \quad (23)$$

where  $\rho_{\text{sfr}}$  is the star-formation threshold. Note that this definition makes  $P_{\text{ref}}$  effectively a function of the black hole mass alone. We now compare  $P_{\text{ref}}$  for each BH to its actual surrounding gas pressure  $P_{\text{ext}}$ , which each BH sink particle measures for its current location. If we have  $P_{\text{ext}} < P_{\text{ref}}$  then the external gas pressure is not able to compress the gas around the BH against the quasar-mode feedback to a density exceeding the star-formation threshold. In this case our multiplication factor for  $\alpha$  is not really meaningful. We compensate this by lowering the accretion rate estimate by the factor  $(P_{\text{ext}}/P_{\text{ref}})^2$ . In the regime of very hot gas (where  $\Lambda(T) \sim T^{1/2}$ ), this will lower the bubble temperature approximately by the factor  $P_{\text{ext}}/P_{\text{ref}}$ , and increase its density by the inverse of this factor, while the actual accretion rate is hardly changed. We have found that this scheme reliably prevents the formation of unphysically large bubbles around BHs in the ‘‘low state’’, whereas the self-regulated growth of the black holes and their final masses is unaffected.

BHs do not only grow through gas accretion, but also when they merge with other BHs. BHs merge once they are within their ‘‘feedback radius’’ (see below). Here we also do not consider the relative velocities of BHs for the same reason that we neglect the velocity term in the accretion rate.

### 2.6.3 Quasar- and radio-mode feedback

For AGN feedback we use a two-state model as used in previous studies (see Springel et al. 2005b; Sijacki et al. 2007, for details). This model distinguishes between quasar-mode feedback (high BH accretion rates) and radio-mode feedback (low BH accretion rates). Quasar-mode AGN feedback is modelled by assuming that a fraction ( $\epsilon_f$ ) of the radiative energy released by the accreted gas cou-

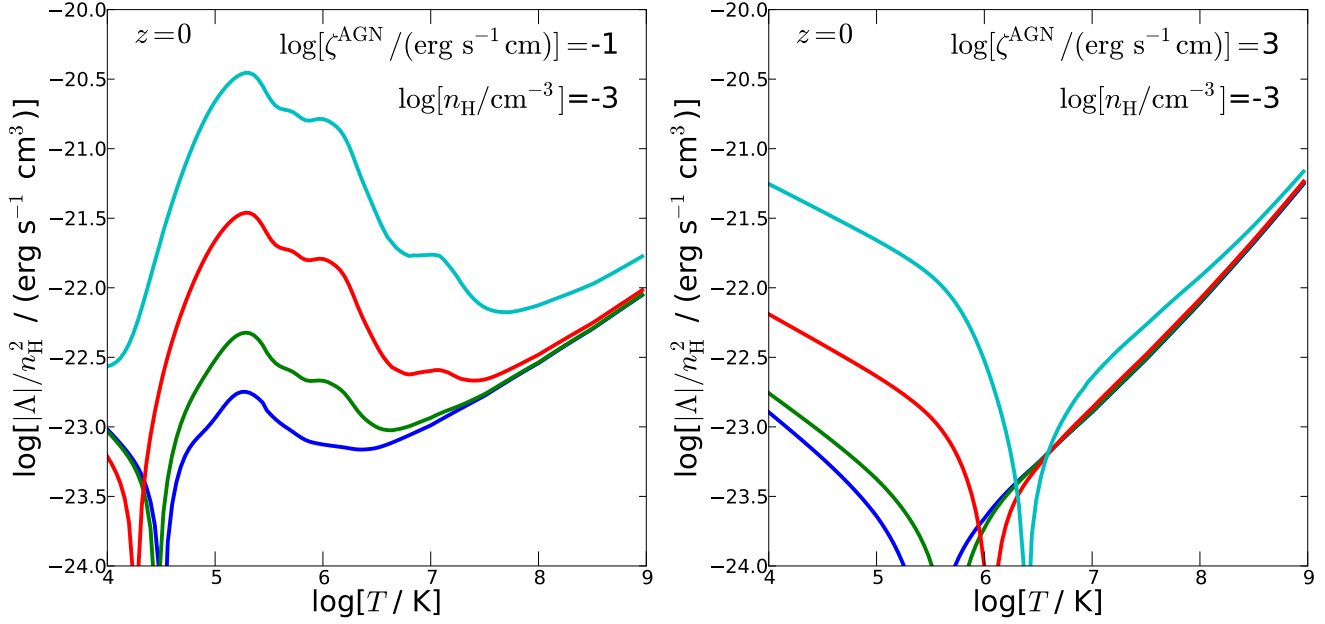


**Figure 1.** Influence of the AGN radiation field (“electro-magnetic feedback”) on the net cooling rate for gases of different metallicities, in the range  $\log[Z/Z_{\odot}] = -2.0, -1.0, 0.0, 1.0$  (lowest to highest curve). The AGN ionisation parameter is negligibly small in the left panel ( $\zeta_{\text{thresh}}^{\text{AGN}} = 10^{-1} \text{ erg s}^{-1} \text{ cm}$ ), but substantial in the right panel ( $\zeta_{\text{thresh}}^{\text{AGN}} = 10^3 \text{ erg s}^{-1} \text{ cm}$ ). Clearly, a high ionisation parameter leads to a strong cooling suppression and significant additional heating, as seen in the net cooling rates in the right panel. We note that such large ionisation parameters require high BH accretion rates close to Eddington. Therefore, halo gas is exposed to such a radiation field typically only a rather short period of cosmic time during quasar activity. For lower BH accretion rates the radiation field is essentially too small to produce large ionisation parameters for a significant fraction of the halo gas.

ples thermally to nearby gas within a radius that contains a pre-calculated mass scale. Significant quasar activity requires high densities of relatively cold gas around the black hole, supplied through large-scale inflows during galaxy mergers. We will in the following assume a radiative efficiency of  $\epsilon_r \sim 0.1-0.2$  (Shakura & Sunyaev 1973; Yu & Tremaine 2002). For quasar-mode AGN feedback we follow the same approach as for the enrichment scheme presented above and distribute energy over a number of BH neighbour cells such that a pre-defined mass is enclosed within the thermal “feedback radius”. We set the mass over which to spread the BH thermal energy to the same mass that is also used for the enrichment scheme, which again is typically set to a multiple of the target mass ( $m_{\text{target}}$ ) of our (de-)refinement scheme. For convergence studies we hold this mass fixed if we change resolution; i.e. the feedback energy is always distributed over a fixed physical mass, following the same strategy as for the enrichment scheme.

For low activity states of the BH, we consider a form of mechanical radio-mode AGN feedback following Sijacki et al. (2007). Quasar- and radio-mode feedback are distinguished based on the BH accretion rate. For BH accretion rates below a fraction  $\chi_{\text{radio}}$  of the Eddington rate, we assume that feedback operates in radio-mode, where AGN jets inflate hot, buoyantly rising bubbles in the surrounding halo atmosphere. The duty cycle of bubble injection, energy content of the bubbles as well as their initial size are estimated based on the BH accretion rate and the current BH mass. The duty cycle is coupled to the mass growth of the BH such that energy is released once the BH has increased its mass by a factor of  $\delta_{\text{BH}}$ . For the bubble properties we assume the scaling relations of Sijacki et al. (2007), with  $R_{\text{bub},0} = 50 \text{ kpc}$ ,  $E_{\text{bub},0} = 10^{60} \text{ erg}$  and  $\rho_{\text{ICM},0} = 10^4 \text{ M}_{\odot} \text{ kpc}^{-3}$ , which we will keep fixed in the following. For the scaling of the distance over which bubbles are placed we use a normalisation value of 100 kpc, which we will also keep

fixed in the following. We assume the radio-mode feedback efficiency provided by the bubbles to be  $\epsilon_{\text{em}} \times \epsilon_r$  of the accreted rest mass energy.

#### 2.6.4 Radiative AGN feedback

So far we discussed only thermal and mechanical AGN feedback, which are the most commonly employed feedback channels in BH simulations. However, near strong ionising radiation sources like AGN the radiation field is very different from the spatially uniform UVB assumed for the net cooling rate calculation above. It is well-known that this can alter the photo-ionisation and photo-heating rates of nearby plasma (e.g., Rees 1986; Efstathiou 1992; Hambrick et al. 2009, 2011; Gnedin & Hollon 2012). For AGN, this provides a channel of non-thermal/non-mechanical feedback (e.g., Sazonov et al. 2005; Ciotti & Ostriker 2007; Hambrick et al. 2011; Kim et al. 2011; Gnedin & Hollon 2012; Choi et al. 2012). Fully accounting for this effect in detail requires polychromatic radiative transfer which is too expensive to be applied to large-scale galaxy formation simulations. We will try here to take radiative electromagnetic feedback into account using an approximate approach. We assume a universal and time-independent AGN SED parameterised as (see Korista et al. 1997, for more details)

$$f^{\text{AGN}}(\nu) = \nu^{\alpha_{\text{UV}}} \exp\left(-\frac{h\nu}{kT_{\text{BB}}}\right) \exp\left(-\frac{10^{-2} \text{ Ryd}}{h\nu}\right) + a\nu^{\alpha_{\text{X}}}, \quad (24)$$

where the big bump component is exponentially cut off at a temperature  $T_{\text{BB}}$ , and the UV-bump is suppressed exponentially in the infrared at a temperature  $kT_{\text{IR}} = 0.01 \text{ Ryd}$ . The  $\alpha_{\text{X}}$  and  $\alpha_{\text{UV}}$  parameters describe the slope of the X-ray component and the low-energy slope of the big bump continuum, respectively. The ratio of

X-ray to UV,  $\alpha_{0X}$ ,

$$\frac{f^{\text{AGN}}(2 \text{ keV})}{f^{\text{AGN}}(2500 \text{ \AA})} = \left( \frac{2 \text{ keV}}{2500 \text{ \AA}} \right)^{\alpha_{0X}} = 403.3^{\alpha_{0X}}, \quad (25)$$

is set through a corresponding choice of the normalisation  $a$ . In the following we will assume a fixed SED with  $T_{\text{BB}} = 10^6 \text{ K}$ ,  $\alpha_{0X} = -1.4$ ,  $\alpha_{\text{UV}} = -0.5$  and  $\alpha_X = -1$  (Zamorani et al. 1981; Francis et al. 1993; Elvis et al. 1994) as our default reference model. We note that this radiative feedback is most effective for accretion rates close to Eddington, and it is therefore a reasonable choice to assume a fixed SED (Sazonov et al. 2005).

Based on the AGN SED, we can tabulate metal line cooling and heating rates for different AGN bolometric intensities. For that we superpose the redshift dependent UVB with the AGN radiation field and create similar net metal line cooling rate tables as for the UVB described above. Primordial cooling is changed by calculating the photo-ionisation rates

$$\Gamma_i = \int_{\nu_i}^{\infty} \frac{4\pi(J^{\text{UVB}}(\nu) + J^{\text{AGN}}(\nu))}{h\nu} \sigma_i(\nu) d\nu = \Gamma_i^{\text{UVB}} + \Gamma_i^{\text{AGN}}, \quad (26)$$

and photo-heating rates

$$\epsilon_i = \int_{\nu_i}^{\infty} \frac{4\pi(J^{\text{UVB}}(\nu) + J^{\text{AGN}}(\nu))}{h\nu} \sigma_i(\nu)(h\nu - h\nu_i) d\nu = \epsilon_i^{\text{UVB}} + \epsilon_i^{\text{AGN}}. \quad (27)$$

Here  $\Gamma_i$  and  $\epsilon_i$  are the photo-ionisation and -heating rates, respectively, for  $\text{H}^0$ ,  $\text{He}^+$  and  $\text{He}^0$ . The quantities  $\nu_i$  and  $\sigma_i(\nu)$  are the threshold frequencies and cross sections for photo-ionisation. We note that the superposition of both radiation fields (UVB plus AGN) is a valid approximation since near BHs the local AGN radiation field is significantly stronger than the overall smooth and uniform UVB. The addition of  $J^{\text{UVB}}(\nu)$  has in that case no impact on the cooling and heating rates. We further note that  $\Gamma_i^{\text{AGN}}$  and  $\epsilon_i^{\text{AGN}}$  need to be calculated only for one fixed bolometric luminosity since we can simply scale them linearly with bolometric intensity and add them to  $\Gamma_i^{\text{UVB}}$  and  $\epsilon_i^{\text{UVB}}$ , respectively. We assume that the gas is optically thin to AGN radiation. To improve on that assumption we take into account a simple approximation for AGN obscuration as a function of the AGN bolometric luminosity  $L_{\text{bol}}^{\text{AGN}}$ . We employ a power-law parameterisation (Hopkins et al. 2007), which we apply to the full bolometric luminosity

$$L_{\text{bol}}^{\text{AGN,obs}} = \omega_1 \left( \frac{L_{\text{bol}}^{\text{AGN}}}{10^{46} \text{ erg s}^{-1}} \right)^{\omega_2}, \quad (28)$$

where we adopt  $\omega_1 = 0.3$  and  $\omega_2 = 0.07$  as our default choice. With this obscuration scheme, we arrive at a rather conservative estimate for the radiation intensity impinging the halo gas. In addition, we assume that star-forming gas is optically thick to the AGN radiation and therefore neglect this effect for gas above the SF density threshold. To incorporate the impact of AGN radiation in the simulation, we assign to each gas cell a bolometric intensity based on the obscured bolometric luminosities  $L_{\text{bol}}^{\text{AGN,obs}}$  of all BHs and the cell's distance to the BHs.

To capture both radiatively efficient and inefficient accretion we change our default radiative efficiency of  $\epsilon_r$  to

$$\tilde{\epsilon}_r = \epsilon_r \frac{2x}{1+x}, \quad x = \frac{1}{\chi_{\text{radio}}} \frac{\dot{M}_{\text{BH}}}{\dot{M}_{\text{Edd}}}, \quad (29)$$

if the BH accretion rate falls below  $\chi_{\text{radio}}$  of the corresponding Eddington rate (see also Ciotti et al. 2009); i.e. if  $x < 1$ . This leads

to a continuous transition from the ADAF (Narayan & Yi 1994) to the radiatively efficient accretion regime, where we assume, as discussed above, a constant efficiency of  $\epsilon_r$ . We note that we use this efficiency scaling only for the luminosity calculation for the AGN and not for the AGN thermal and mechanical feedback discussed earlier. To be consistent with the quasar- and radio-mode AGN feedback described above we will only allow an energy fraction  $(1 - \epsilon_r)$  or  $(1 - \epsilon_m)$  to go into electro-magnetic feedback for quasar-mode or radio-mode feedback, respectively. We note that this correction and the smooth  $\epsilon_r$  parameterisation are not crucial since radiative feedback is anyways only significant for BHs in the quasar-mode phase with very high accretion rates.

In Figure 1, we show net cooling rates for gases of different metallicities which are exposed to different AGN radiation sources characterised by their ionisation parameter  $\zeta^{\text{AGN}} = L_{\text{bol}}^{\text{AGN}}/(r^2 n_{\text{H}})$ , where  $L_{\text{bol}}^{\text{AGN}} = (1 - \epsilon_r) \dot{\epsilon}_r \dot{M}_{\text{BH}} c^2$  is the bolometric luminosity and  $r$  is the distance from the plasma cell to the AGN radiation source. We note that  $J^{\text{AGN}} \equiv L_{\text{bol}}^{\text{AGN}}/r^2$  is the bolometric intensity that we tabulate in the cooling table to look up the metal line cooling. As Figure 1 demonstrates, a simple  $Z$ -scaling of the rates does not work in this regime. We hence need to tabulate metal-line cooling rates also as a function of  $Z$ . Specifically, we extend the grid of net cooling rates by  $[\log(Z/Z_{\odot}), \log(4\pi J^{\text{AGN}}/(\text{erg s}^{-1} \text{ cm}^{-2}))]$ , with  $-5 < \log(4\pi J^{\text{AGN}}/(\text{erg s}^{-1} \text{ cm}^{-2})) < 5$  sampled equally spaced at 11 bins, and six different metallicities  $\log(Z/Z_{\odot}) = -4, -3, -2, -1, 0, 1$ . At each redshift, we also add grid points for a pure UVB which we use for heating and cooling if there is no nearby AGN. Although Figure 1 clearly demonstrates that the AGN radiation field can strongly influence net cooling rates, we note that this occurs only for a short interval of cosmic time for each BH once it is in its maximum accretion phase with an accretion rate close to Eddington. This implies that the impact of electro-magnetic AGN feedback is strongest during quasar activity, but is limited when AGN enter the low accretion radio-mode state.

The intensity assignment is performed by looping over all BHs and calculating their bolometric luminosities based on the current mass accretion rates. We first calculate a search radius for each BH. For this we derive the BH's bolometric obscured luminosity and solve for the radius within which the ionisation parameter is larger than  $\zeta_{\text{thresh}}^{\text{AGN}} = 10^{-3} \text{ erg s}^{-1} \text{ cm}$ , assuming gas with mean hydrogen number density. We then calculate for all cells within this radius the incoming AGN intensity. To avoid excessively large search radii we impose an upper limit of three times the virial radius to this search radius. We have checked that our results are not sensitive to this radius once it is chosen to be of the order of the virial radius or larger. Overlapping AGN contributions of several BHs are handled by summing up their bolometric intensities at the cell's position. Once we know all local intensities we can calculate the net cooling rate for each cell. We do not include speed-of-light delay effects in the propagation from the AGN, which is a reasonable approximation since we limit the sphere of influence of the radiation field as described above, and do not allow the radiation field to propagate over arbitrarily large distances through the simulation volume.

### 3 ANALYSIS TECHNIQUES

#### 3.1 Tracer particles

The pseudo-Lagrangian nature of SPH is convenient for approximately tracing mass elements in simulations. (Although we emphasise that this 'advantage' of SPH comes at the expense of an

inaccurate integration of the mass continuity equation (see, e.g., Vogelsberger et al. 2012.) On the other hand, the Eulerian nature of finite volume schemes does not directly allow this because the mass continuity equation is integrated correctly on the resolution scale. One approach to address this “disadvantage” of grid codes is to use an additional passive tracer particle species which is advected along with the gas by inferring a tracer’s velocity by interpolating the calculated hydrodynamic velocity field.

AREPO employs a quasi-Lagrangian scheme; i.e. it is neither Eulerian nor strictly Lagrangian since mass can be advected through cell boundaries as in an ordinary finite volume approach. (We note here that SPH is not actually Lagrangian either, at best “pseudo-Lagrangian”, as the remapping that implicitly occurs when local neighbourhood relations of particles change is ignored in this approach.) This quasi-Lagrangian nature of AREPO implies that tracing the evolution of “closed-box” fluid elements is not possible a priori, similar to the situation in other finite volume schemes. We have therefore realised two different passive tracer techniques in AREPO (Genel et al. 2013). First, we implemented the velocity field approach, which ties the tracers to the reconstructed and interpolated fluid velocity field. Second, we developed a new scheme, which determines the exchange of tracers between cells in a Monte Carlo fashion based on the actual mass exchanges between them, which is given by the Riemann solver. We briefly describe the main characteristics of these schemes in the following two subsections.

### 3.1.1 Velocity field tracer particles

Velocity field tracer particles move according to the piece-wise linear reconstruction of the velocity field. At each time step, we make a look up of the closest mesh-generating point for every active tracer particle, which provides the Voronoi cell that this tracer resides in. We then use the fluid velocity field gradients of that cell to interpolate the velocity field to the tracer position. The gradient information is readily available for the cells, because it is already calculated for the MUSCL-Hancock step in the finite volume solver. Once a new velocity is assigned to each active tracer particle we drift them according to their individual time steps. Tracer particles inherit the time step from the cells they fall in, which makes their time integration adaptive and consistent with the dynamics of the underlying cell timestep hierarchy.

Velocity field tracer particles try to follow the stream lines of the underlying flow field and are essentially noise-free. Moving them is computationally very cheap, the only moderate computational effort lies in the required closest cell lookup, which however can be realised very efficiently through a tree search with an initial search radius guessed based on the nearest cell distance of the last search. However, we have found that this tracer particle approach does not follow the gas mass properly. Since the fluid is evolved based on the local solutions to the Riemann problems across each cell interface, simply using the reconstructed velocity field to advect the tracers does not lead to consistent evolution between the tracers and the fluid. Moreover, the fluid is averaged in the cell and reconstructed after it is evolved, while those steps are not performed on the tracers.

The inconsistency between the flow of the fluid and that of the tracers leads in cosmological simulations to large biases (Genel et al. 2013). For example, the tracer density profiles of haloes deviate significantly from the actual gas density profiles. This effect was already found in other studies, but was not interpreted appropriately. For example, Price & Federrath (2010) studied turbulence with the velocity field tracer implementation of the FLASH code

and found that tracer particles tend to clump on sub-resolution scales in turbulence simulations.

### 3.1.2 Monte Carlo tracers

Instead of relating the tracer evolution directly to the velocity field, we can also link them to the mass exchange between cells. The basic idea of this approach, presented and studied in Genel et al. (2013), is to attach a population of  $N_i \geq 0$  Monte Carlo tracers to a computational Voronoi cell  $i$ . Based on the finite volume update solution for this cell we know the mass fluxes through each cell face during the time step. We can then probabilistically sample the transfer of tracer particles from one cell to the other. This results in a Monte Carlo sampling of the underlying gas mass fluxes over the computational domain, which does, by construction, not suffer from the bias effect. Such a scheme can be easily inlined in the finite volume calculations, which loop over all Voronoi cell faces. This face list is constructed by the tessellation engine. During the interface loop we keep track of the current number of tracers per cell, and of the current total mass in each cell. We only consider outgoing mass fluxes  $\Delta M_{i,j} < 0$  from cell  $i$  to cell  $j$ . Furthermore, we keep track only of the reduced mass  $\widetilde{M}_i$  of each cell, which is updated for each outgoing flux, but not for in-going fluxes since the tracer particle exchange is done for all outgoing fluxes starting from a given cell. In-going fluxes into cell  $i$  are symmetrically treated by the outgoing fluxes of cell  $j$ . The probability for a tracer to leave cell  $i$  and go into cell  $j$  is then given by  $p_{i,j}^{\text{flux}} = \Delta M_{i,j} / \widetilde{M}_i$ . To decide whether a tracer should leave a cell we draw a random number  $x_\alpha \in U(0, 1)$  for each tracer  $\alpha \leq N_i$  of cell  $i$ . The tracer is put into cell  $j$  if  $x_\alpha < p_{i,j}^{\text{flux}}$ .

In such a Monte Carlo based approach, tracers have no phase-space coordinates within the cell, corresponding to the assumption that they are always uniformly mixed within a cell. We therefore store them simply in a globally distributed linked list where each list entry has a tracer ID, a set of tracked fluid properties, and a pointer to the next and the previous tracer in the list. Each fluid cell then needs only a pointer to the first tracer associated with it. Tracer exchanges between cells can be implemented as operations on this global linked list.

Another advantage of Monte Carlo tracers is that any sort of mass transfer in or out of the gas cells can be modelled probabilistically in that scheme. This can be used, for example, to follow mesh (de-)refinement operations, but also for treating the formation of stars, BHs or wind particles. We exploit this in our implementation and have added, in addition to the tracers associated with gas cells, star, wind and BH-tracers to keep track of *all* baryonic mass exchanges. For example, this allows us to quantify precisely (albeit with some Monte Carlo noise that can be reduced by averaging over many cells) what fraction of gas in a cell has previously been part of a star or a wind, or exactly which gas was swallowed by BHs.

## 3.2 On the fly volume rendering

Efficient visualisation of complex simulation datasets becomes increasingly important since it can provide insights into the physical mechanisms at play. Both for SPH- and AMR-based simulations, a large number of visualisation toolkits exist. For example, SPLASH (Price 2007) or SPLITCH (Dolag et al. 2011) provide easy-to-use tools to visualise various aspects of astrophysical SPH simulation data. AMR data can be efficiently visualised by many different software packages, including Mayavi, Visit, Paraview, and

yt (Turk et al. 2011). Tools for visualising an unstructured Voronoi mesh like the one used by AREPO are much less common and hardly exist in comparison.

Since AREPO contains already all the required Voronoi mesh infrastructure it is natural to add a volume rendering engine directly to the code. This has the advantage that the rendering can be done at a very high time frequency on-the-fly and on very large datasets due to the implemented parallelism. To this end, we have added a simple volume rendering algorithm to AREPO. Specifically, we have implemented an image-space ray-casting scheme, which follows the propagation of individual rays through the rendered volume. Given a predefined camera path, this allows for orthogonal and perspective projections. Our scheme performs the ray-casting operation in frequent time intervals, where a predefined number of rays is integrated from a near field plane to a far field plane, using the front-to-back recursive rendering equation

$$\begin{aligned} \mathbf{C}_{n+1}^{\text{acc}} &= \mathbf{C}_n^{\text{acc}} + (1 - \alpha_n^{\text{acc}}) \mathbf{C}_n^{\text{cell}} \alpha_n^{\text{cell}} \\ \alpha_{n+1}^{\text{acc}} &= \alpha_n^{\text{acc}} + (1 - \alpha_n^{\text{acc}}) \alpha_n^{\text{cell}}, \end{aligned} \quad (30)$$

where  $\mathbf{C}_{n+1}^{\text{acc}}$  is the accumulated ray colour vector,  $\mathbf{C}_n^{\text{cell}}$  is the colour vector assigned to the current Voronoi cell based on some set of transfer functions,  $\alpha_{n+1}^{\text{acc}} \leq 1$  is the accumulated ray opacity, and  $\alpha_n^{\text{cell}}$  is the opacity assigned to the current Voronoi cell specified through some transfer function. We note that this recursive render equation is simply a discretised version of an emission-absorption model which ignores any scattering. Since we perform a front-to-back ray casting, we need to keep track of the accumulated opacity during the  $\alpha$  compositing. Starting from the near plane allows one to terminate the ray-casting process once the opacity for a given ray has reached a value of  $\lesssim 1$ . Such early ray termination leads to a speed-up of the rendering process without affecting the results.

The actual ray traversing is done by exploiting mesh connectivity information which is available through the Voronoi mesh implementation in AREPO. We also use this connectivity for a smoothing operation that we optionally apply during the render process. Especially in regions of low density, the number of Voronoi cells sampling the gas distribution can be quite low. Visually, this can then lead to discrete transitions from one cell to the other, which can show up in the rendered images, similar to the familiar block structure showing up in many images of AMR simulations. To reduce this effect, we have implemented a smoothing procedure, which averages cell values based on the values of the nearest cells which are connected to the current ray casting cell. Specifically, we first make one loop over all neighbouring cells and calculate the maximum distance of their mesh generating points to the current ray location in the primary cell. We then take this radius as a smoothing length for a top hat kernel based cell value estimate, where we weight the cell values that are going to be rendered according to the cell volume.

### 3.3 Stellar population synthesis models

To compare our galaxy formation model predictions with observations, we need to transform stellar information of our simulated galaxies into photometric properties. Stellar population synthesis models (e.g., Leitherer et al. 1999; Bruzual & Charlot 2003; Le Borgne et al. 2004) provide a convenient way to associate the stars in our simulations with observable spectra or broad band luminosities. We include this in our simulations by assigning to each star particle a series of broad-band luminosities based on the Bruzual & Charlot (2003) catalogues after taking into account the star par-

ticl’s age, mass, and metallicity. Currently, we choose to include the U-, V-, B-, K-, g-, r-, i-, and z-bands, however, this could be extended easily to include any other spectral information which is accurately tabulated in the stellar population synthesis models.

The assigned stellar luminosities are not currently used in any part of the dynamical evolution, nor do we include radiative transfer or dust attenuation. However, adding together the luminosity contributions from all star particles in a given subhalo allows us to construct estimates of the galaxy luminosities in several bands for direct comparison against observations. We construct broad-band luminosities for all galaxies, and store the values in the group catalogues to simplify basic post-processing analysis.

## 4 COSMOLOGICAL SIMULATIONS

### 4.1 Simulations

We will present in this section the first cosmological AREPO simulations including the newly added physics described above. In the following, we adopt the cosmological parameters  $\Omega_{m0} = 0.27$ ,  $\Omega_{\Lambda 0} = 0.73$ ,  $\Omega_{b0} = 0.0456$ ,  $\sigma_8 = 0.81$ , and  $H_0 = 100 h \text{ km s}^{-1} \text{ Mpc}^{-1} = 70.4 \text{ km s}^{-1} \text{ Mpc}^{-1}$  ( $h = 0.704$ ). We create realisations of this cosmology in periodic boxes with a side length of  $25 h^{-1} \text{ Mpc}$ . Initial conditions are generated at  $z = 127$  based on a linear power spectrum made by CAMB, with gas particles/cells added to the initial conditions by splitting each original particle into a dark matter and gas particle/cell pair, displacing them with respect to each other such that two interleaved grids are formed, keeping the centre-of-mass of each pair fixed.

Our fiducial parameters for the different physical processes are summarised in Table 1. These parameters are physically plausible and were chosen such that they provide a reasonable fit to most key observables at  $z = 0$ , as we discuss below. Most importantly, the feedback parameters of our fiducial model are chosen such that they reasonably well reproduce the stellar mass function and the stellar mass – halo mass relation. We also explore a few modifications of this fiducial model, where we focus on differences in the stellar and AGN feedback processes. All our simulations are summarised in Table 2. We specify two Plummer-equivalent gravitational softening length values. For DM particles, we use a fixed comoving softening length (second value). For baryonic collisionless particles (stars and BHs), we further assume a maximum physical softening length (first value), which limits the growth of the physical softening length. Gas cells use an adaptive softening length tied to the cell radius, limited by a floor. This floor is set to the same value as for the other baryonic particles (i.e. stars and BHs). In the table, we also specify the simulation volume and the mass resolution for DM and baryons. Finally, the last column describes the physics characteristics of the specific model with respect to our fiducial model. We employ a (de-)refinement scheme which keeps the cell masses close to a specified target mass  $m_{\text{target}}$ , which results in a nearly constant number of cells. This scheme is identical to that used in Vogelsberger et al. (2012), and we also follow the same mesh regularisation strategy.

Table 2 includes three simulations with the fiducial setup presented in Table 1: L25n128, L25n256, L25n512. These three simulations serve as a resolution study of our fiducial physics setup to estimate convergence. The other simulations explore modifications of the fiducial setup. Each of these modified runs typically varies only one of the feedback parameters of our fiducial setup and explores it at the intermediate resolution equivalent to the L25n256

variable	fiducial value	description
stellar feedback (non-local energy-driven)		
$\kappa_w$	3.7	wind velocity relative to local DM 1D velocity dispersion
$\text{egy}_w/\text{egy}_w^0$	1.09	available SNII energy per formed stellar mass in units of $[\text{egy}_w^0]$
$\text{mom}_w/\text{km s}^{-1}$	0	specific wind momentum in units of $[\text{km s}^{-1}]$
AGN feedback (quasar-mode)		
$\epsilon_f$	0.05	quasar mode feedback energy fraction
$\epsilon_r$	0.2	radiative efficiency for Bondi accretion
AGN feedback (radio-mode)		
$\chi_{\text{radio}}$	0.05	accretion rate threshold for radio-mode in units of $[\dot{M}_{\text{Edd}}]$
$\delta_{\text{BH}}$	1.15	duty cycle of radio-mode
$\epsilon_m$	0.35	radio-mode feedback energy fraction
AGN feedback (electro-magnetic)		
$\omega_1, \omega_2$	0.3, 0.07	AGN obscuration parameterisation
wind metal loading		
$\gamma_w$	0.4	metal loading of wind particles

**Table 1.** Fiducial model parameters. We assume purely energy-driven, non-local winds for stellar feedback. AGN feedback consists of three components: quasar-mode (thermal), radio-mode (mechanical) and radiative (electro-magnetic) feedback. For SNII winds, we specify the mass loading parameter  $\text{egy}_w$  (in units of  $\text{egy}_w^0 = 1.73 \times 10^{-2} 10^{51} \text{ erg M}_\odot^{-1}$ ; i.e.  $E_{\text{SNII},51} = 1$ ) and the wind velocity  $\kappa_w$  (in units of the local 1D DM velocity dispersion). For AGN feedback,  $\epsilon_r$  indicates the radiative efficiency,  $\epsilon_f$  the fraction of the bolometric luminosity that is thermally coupled to nearby gas as a form of quasar-mode feedback and  $\epsilon_m$  the energy fraction that goes into bubbles through radio-mode feedback once the BH accretion rate drops below  $\chi_{\text{radio}}$  of the Eddington rate. Electro-magnetic AGN feedback is specified by a fixed SED ( $T_{\text{BB}} = 10^6 \text{ K}$ ,  $\alpha_{0X} = -1.4$ ,  $\alpha_{UV} = -0.5$  and  $\alpha_X = -1$ ) and the obscuration factors  $\omega_{1,2}$ . The feedback parameters are chosen such that they are physically plausible and provide a good match to key observations.

name	volume [[ $h^{-1} \text{ Mpc}$ ] <sup>3</sup> ]	cells/particles	$\epsilon$ [ $h^{-1} \text{ kpc}$ ]	$m_{\text{DM}}/m_{\text{target}}$ [ $h^{-1} \text{ M}_\odot$ ]	physics
L25n512	$25^3$	$2 \times 512^3$	0.5/1.0	$7.33 \times 10^6 / 1.56 \times 10^6$	fiducial
L25n256	$25^3$	$2 \times 256^3$	1.0/2.0	$5.86 \times 10^7 / 1.25 \times 10^7$	fiducial
L25n128	$25^3$	$2 \times 128^3$	2.0/4.0	$4.69 \times 10^8 / 1.00 \times 10^8$	fiducial
stronger winds	$25^3$	$2 \times 256^3$	1.0/2.0	$5.86 \times 10^7 / 1.25 \times 10^7$	$\text{egy}_w/\text{egy}_w^0 = 2.18$
weaker winds	$25^3$	$2 \times 256^3$	1.0/2.0	$5.86 \times 10^7 / 1.25 \times 10^7$	$\text{egy}_w/\text{egy}_w^0 = 0.545$
faster winds	$25^3$	$2 \times 256^3$	1.0/2.0	$5.86 \times 10^7 / 1.25 \times 10^7$	$\kappa_w = 7.4$
slower winds	$25^3$	$2 \times 256^3$	1.0/2.0	$5.86 \times 10^7 / 1.25 \times 10^7$	$\kappa_w = 1.85$
stronger radio	$25^3$	$2 \times 256^3$	1.0/2.0	$5.86 \times 10^7 / 1.25 \times 10^7$	$\epsilon_m = 0.7$
weaker radio	$25^3$	$2 \times 256^3$	1.0/2.0	$5.86 \times 10^7 / 1.25 \times 10^7$	$\epsilon_m = 0.175$
higher radio threshold	$25^3$	$2 \times 256^3$	1.0/2.0	$5.86 \times 10^7 / 1.25 \times 10^7$	$\chi_{\text{radio}} = 0.1$
lower radio threshold	$25^3$	$2 \times 256^3$	1.0/2.0	$5.86 \times 10^7 / 1.25 \times 10^7$	$\chi_{\text{radio}} = 0.025$
no feedback	$25^3$	$2 \times 256^3$	1.0/2.0	$5.86 \times 10^7 / 1.25 \times 10^7$	no stellar/AGN feedback

**Table 2.** Summary of the different cosmological simulations. The L25n128, L25n256, L25n512 simulations employ the fiducial physics parameters listed in Table 1 and explore convergence by changing the mass resolution by a factor of 64 in total. The remaining simulations consider variations of certain physical processes at the intermediate resolution level. Parameters that are varied are indicated in the last column. Here we increase or decrease stellar and AGN feedback parameters by a factor of two. The “no feedback” simulation does not include stellar/AGN feedback (except for the implicit ISM pressurisation).

simulation, which is sufficient to obtain reasonably converged results, and computationally efficient enough to explore different feedback settings quickly. Each of the modified parameters is increased or decreased by a factor of two compared to the fiducial value. We explore here only a rather limited number of parameters. For example, we do not change the quasar-mode feedback strength since we are mainly interested in the stellar properties of haloes and quasar-mode feedback mainly regulates BH growth (see below). Furthermore, we do not alter the wind model; i.e. we only vary the

parameterisation of the non-local energy-driven winds presented in Table 1, but we do not explore, for example, local or momentum-driven winds. For the sake of brevity, we here also do not explore a large number of unrealistic setups like models without metal-line cooling or without stellar mass loss. While such test simulations can be interesting for studying the specific implications of these physical effects, our goal is here to bracket the feedback parameters required to obtain an acceptable physical match to observations; hence we explore only models with complete physics in this



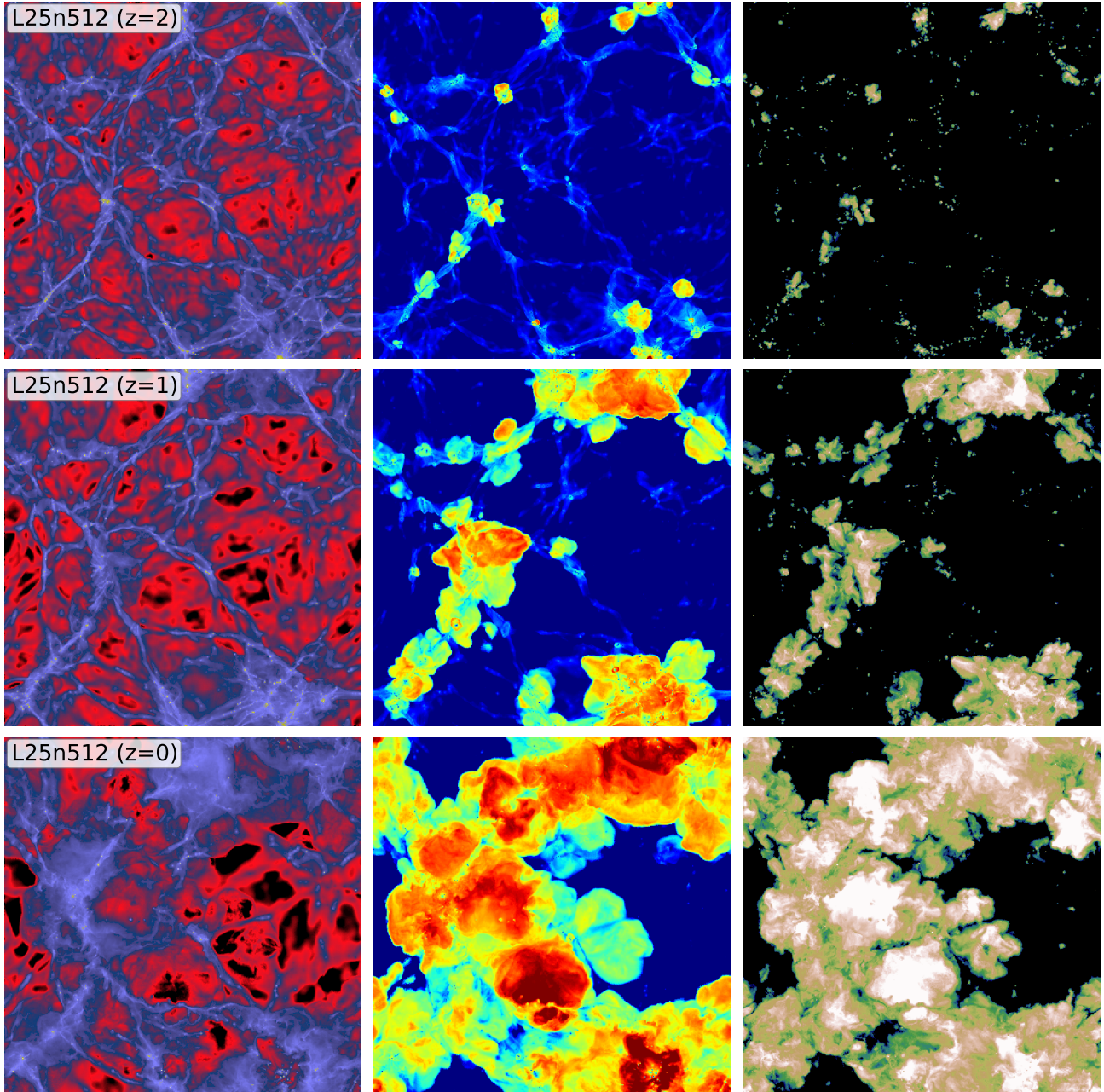


**Figure 2.** Gas density (left panel), gas temperature (middle panel) and gas metallicity (right panel) projections of the L25n512 simulation. Each panel is  $25 h^{-1}$  Mpc on a side and has a thickness of  $1 h^{-1}$  Mpc. We show the fields at three different redshifts  $z = 0, 1,$  and  $2$ . At  $z = 2$  some haloes show outflows generated mainly by strong winds through stellar SNII feedback. The more dramatic heating effects at late times ( $z = 0, 1$ ) are largely caused by strong radio-mode AGN feedback. Both stellar and AGN feedback lead to a significant enrichment of the IGM as can be seen in the metallicity projections. Strong AGN feedback also alters the density structure of the gas at  $z = 0$  (see left panel).

subsection. However, we include one simulation (“no feedback”), which does not include stellar and AGN feedback except for the implicit ISM pressurisation through SNII feedback as implemented in our effective EOS for star forming ISM gas. We consider this “no feedback” simulation to demonstrate that such a model gives a very poor fit to observations, highlighting the difference with our fiducial model which includes the full feedback physics. We stress that this “no feedback” simulation contains a weak form of stellar feedback in form of the ISM pressurisation. To understand the importance of the different physical processes in our model we will

present unrealistic simulations in Section 4.3 below. There we deactivate certain physical processes to understand better how they shape our  $z = 0$  results. Clearly, such simulations are not expected to match observational constraints, which is why we do not discuss them here.

We will show below that the fiducial parameters presented in Table 1 produce a galaxy population in good agreement with various observational probes at  $z = 0$  in the local Universe. We stress that some of these feedback parameters differ significantly from those previously used in SPH simulations with similar physics

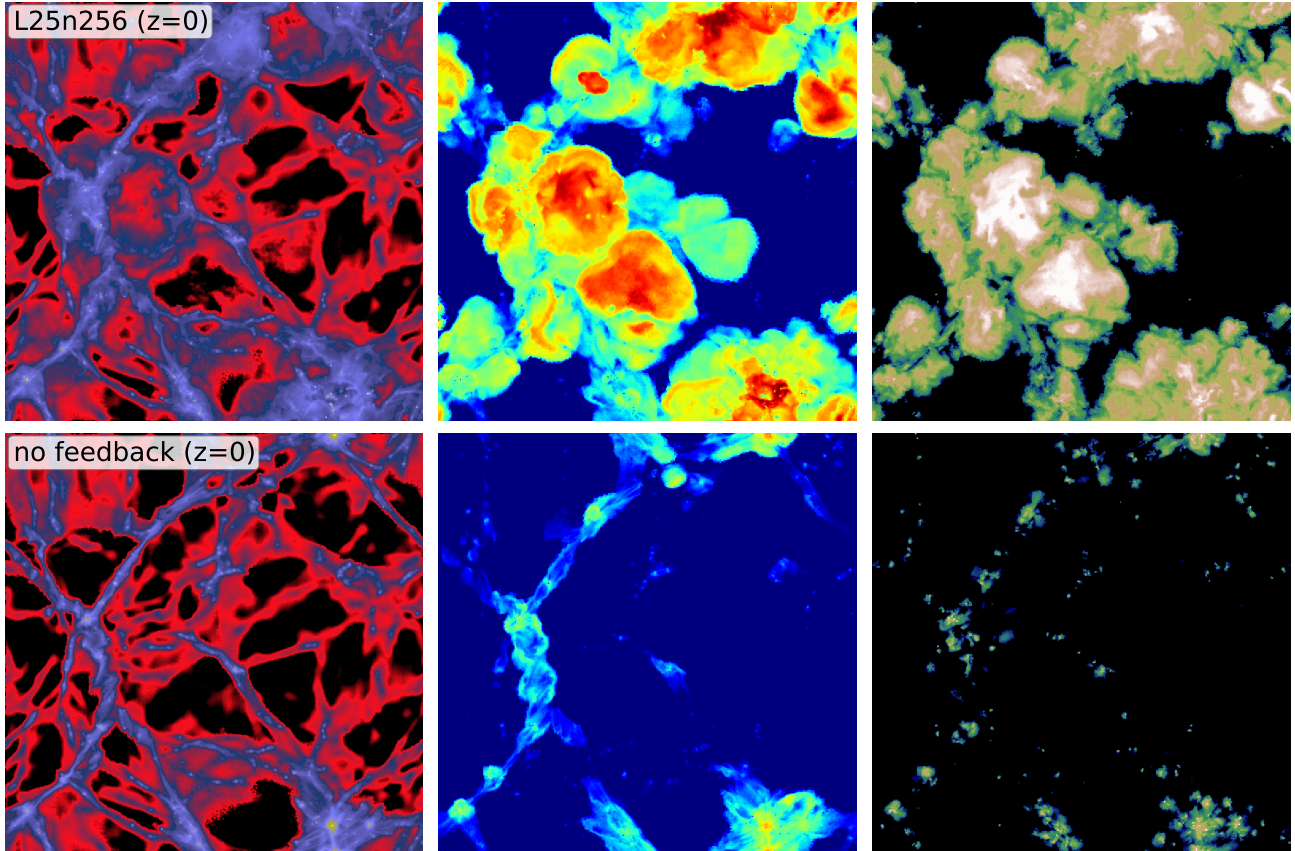


**Figure 3.** Gas density (left panel), gas temperature (middle panel) and gas metallicity (right panel) projections of the L25n256 simulation (top panels) and “no feedback” simulation (bottom panels) at  $z = 0$ . Each panel is  $25 h^{-1}$  Mpc on a side and has a thickness of  $1 h^{-1}$  Mpc (same as Figure 2). Clearly, the addition of more efficient cooling and stellar/AGN feedback strongly affects the thermodynamic properties of the gas. Most dramatically, the metal distribution is altered through the additional feedback enriching the IGM. We note that the colour scale used here is different from the one in Figure 2 as it has been adapted to the different simulation resolution in both figures.

models. Most importantly, the AGN radio-mode feedback is more energetic than in our previous simulations (e.g., Sijacki et al. 2007; Puchwein et al. 2008). This can be seen directly by the value for the radio-mode feedback energy fraction, which is about a factor of two larger than in previous SPH studies. Also, the accretion rate threshold for switching between radio- and quasar-mode feedback is five times larger than in previous simulations. This means that more of the BH accretion energy goes into radio-mode feedback compared to previous work, where  $\chi_{\text{radio}} = 0.01$  was typically adopted. As a result, more feedback energy is deposited displaced from the central BH in a bursty fashion rather than smoothly heating the central region around the BH. This automatically leads to a more efficient suppression of star formation in massive haloes. We found that this combination of an increased radio-mode feedback factor and a higher accretion rate threshold for the quasar mode are necessary to reproduce the observed stellar masses in massive haloes. We also note that the amount of supernova energy for stellar feedback is quite high in our fiducial setup. In fact, it is 1.09 times larger than what is nominally assumed for SNI type events ( $10^{51}$  erg). We argue that this is still physically plausible for a couple of reasons. First,  $10^{51}$  erg is just a canonical value which is in fact uncertain. Second, recent work has shown that accounting for early stellar feedback seems crucial for regulating star formation in low mass systems (Stinson et al. 2013; Kannan et al. 2013). In our

model, we include this contribution in the wind energy budget for launching kinetic wind particles.

The revised settings of the feedback model are required to match the  $z = 0$  observations reasonably well. Less effective feedback leads to a significant overproduction of stellar mass at both the faint and bright ends. The need for even stronger feedback than in SPH was already pointed out in Vogelsberger et al. (2012), where it was demonstrated that AREPO shows enhanced gas cooling compared to previous SPH simulations, which we primarily attribute to spurious viscous heating effects in SPH and an inaccurate treatment of subsonic turbulence (Bauer & Springel 2012). This effect is strongest for high mass systems where a quasi-hydrostatic hot atmosphere can form. SPH simulations show here effectively a form of “numerical quenching”, reducing the amount of AGN feedback required to regulate the amount of stars forming in these systems. Since AREPO does not suffer from this problem (Vogelsberger et al. 2012), we are not helped by “numerical quenching” and instead need to offset the enhanced cooling in large haloes at late times *physically* by stronger forms of stellar and AGN feedback. We note that this form of quenching can also be seen in Springel & Hernquist (2003a,b), where the cosmic SFR density could be reproduced without the inclusion of AGN feedback. This is possible because numerical quenching prevents star formation in massive haloes.



**Figure 4.** Rendered gas temperature field of a large region of the simulation volume of L25n512 at  $z = 0$ . The render frustum has a near field plane distance of  $2 h^{-1}$  Mpc and the far plane is at  $20 h^{-1}$  Mpc. The width of the near field plane is  $2 h^{-1}$  Mpc with a height of  $1.5 h^{-1}$  Mpc. Hot regions are shown in red and cold regions in blue. Galaxies are shown in bright white. Part of the cosmic web and hot halo atmosphere of one of the most massive haloes in the simulation volume can be seen.

## 4.2 Properties of the simulated galaxy population

In the following subsections we present some first comparisons of our simulation results to observational data, where we mainly focus on the local Universe ( $z = 0$ ). This serves primarily as a validation of our galaxy formation model and an identification of acceptable parameter settings. An initial study of the redshift evolution of the predicted galaxy properties is given in Torrey et al. (2013), while an in-depth analysis will be provided in forthcoming studies based on larger and higher resolution simulations.

We identify haloes, subhaloes and galaxies based on the SUBFIND algorithm (Springel et al. 2001; Dolag et al. 2009). In the following, we often refer to the stellar galaxy mass of haloes and subhaloes. For definiteness, we define this mass as the total gravitationally bound stellar mass that is contained within twice the stellar half mass radius of each SUBFIND (sub)halo. This definition of stellar mass does not significantly differ from the total stellar mass for low mass systems, but it excludes some of the intracluster light stars for massive systems. We have checked this definition against surface brightness cuts in different bands and find it to give very similar results as such more detailed methods of excluding intracluster light.

### 4.2.1 General gas structure

A first qualitative view of the simulations is presented in Figure 2, where we show gas density (left panels), gas temperature (middle panels) and gas metallicity (right panels) projections of the highest resolution L25n512 simulation with our fiducial physics setup at three redshifts  $z = 2, 1, 0$  (top to bottom). Each panel is  $25 h^{-1}$  Mpc on a side and has a projection thickness of  $1 h^{-1}$  Mpc. At  $z = 2$ , some haloes show outflows generated mainly by winds associated with stellar feedback leading to IGM enrichment. The more dramatic heating effects at late times are largely caused by strong radio-mode AGN feedback in massive systems. Both stellar and AGN feedback lead to a significant enrichment of the IGM, as can be seen in the right panels. Furthermore, the AGN feedback also alters the density structure of the gas at  $z = 0$ .

To demonstrate the impact of stellar and AGN feedback more clearly, we compare in Figure 3 the L25n256 simulation with the “no feedback” simulation, which does not include stellar and AGN feedback. We note that the colour scales in Figure 2 and Figure 3 are not the same and have been adapted for each resolution. Figure 3 clearly demonstrates that stellar and AGN feedback strongly affect the thermodynamic properties of the gas as can be seen from the density and temperature maps, which differ significantly be-

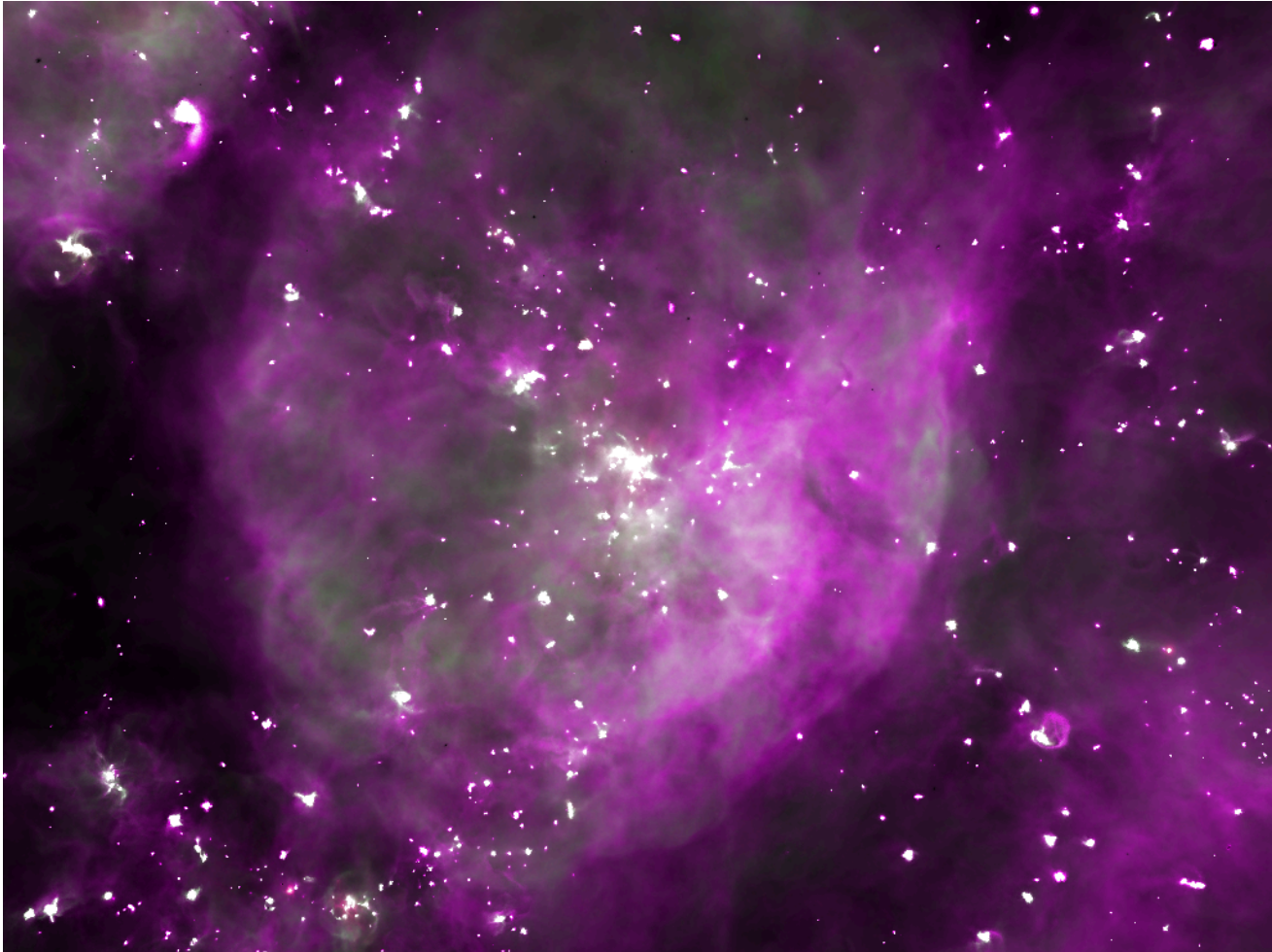


**Figure 5.** Rendered gas metallicity field of a large region of the simulation volume of L25n512 at  $z = 0$ . The render frustum has a near field plane distance of  $2 h^{-1}$  Mpc and the far plane is at  $20 h^{-1}$  Mpc. The width of the near field plane is  $2 h^{-1}$  Mpc with a height of  $1.5 h^{-1}$  Mpc. The hot halo gas shown in Figure 4 is significantly enriched.

tween the two runs. Furthermore, the metal distribution is very different. In fact, the simulation without any feedback does not lead to any significant IGM enrichment as metals are locked up efficiently in galaxies at the centres of haloes.

To give a better impression of the three-dimensional distribution of gas in the simulation volume we show in Figure 4 a volume-rendered gas temperature field of a large fraction of the L25n512 simulation volume<sup>2</sup>. Here, the newly implemented, inlined volume renderer has been used, as described above. We do not employ the smoothing procedure for this rendering. The render frustum has a near field plane distance of  $2 h^{-1}$  Mpc and the far plane is at  $20 h^{-1}$  Mpc. The width of the near field plane is  $2 h^{-1}$  Mpc with a height of  $1.5 h^{-1}$  Mpc. Hot regions are coloured in red, and cold regions in blue. Galaxies are shown in bright white. Parts of the cosmic web and the hot halo atmosphere of one of the most massive haloes in the simulation volume can be seen. In Figure 5, we show the same region of the simulation volume but render the gas metallicity instead. The hot gas atmosphere of the cluster is clearly

significantly enriched. We note that the filaments, which are visible in the temperature rendering, are not clearly visible in Figure 5.

#### 4.2.2 Evolution of the cosmic SFR density

Observationally it is now well-established that the cosmic SFR density increased significantly from  $z \sim 10$  to  $z \sim 2$  and reached a peak value at around  $z \sim 2$  followed by a rapid decline (Lilly et al. 1996; Madau et al. 1998; Schiminovich & et al. 2005; Hopkins & Beacom 2006b; Bouwens et al. 2008). In Figure 6, we show the simulated cosmic SFR density as a function of redshift. To compare our models against observational constraints, we have included a set of cosmic SFR density measurements from the literature, as compiled in Hopkins & Beacom (2006a) and Behroozi et al. (2013). We show a convergence study in the left panel, and an exploration of the different feedback models summarised in Table 2 in the right panel. We will in the following subsections follow the same format and always explore numerical convergence and physical model variations side-by-side.

The left panel of Fig. 6 demonstrates that the shape of the SFR evolution is well preserved for all three resolutions, with a minor normalisation change towards higher SFRs with increasing resolution. The magnitude of this normalisation offset between our two

<sup>2</sup> Volume-rendering movies and high-resolution images are available for download at the website <http://www.cfa.harvard.edu/itc/research/arepogal/>

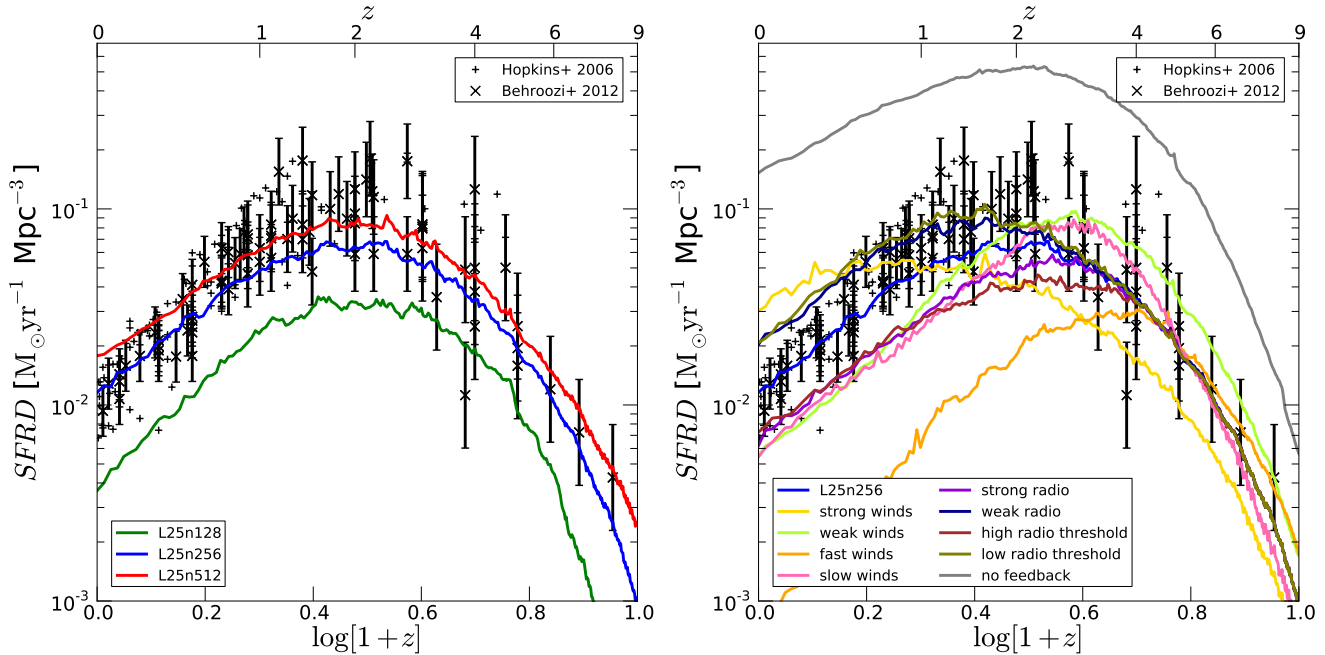


**Figure 6.** Cosmic SFR density as a function of redshift (left panel: resolution study; right panel: different feedback models). Observational data is taken from Hopkins & Beacom (2006a) and Behroozi et al. (2013). The left panel demonstrates that the overall shape of the SFR evolution is well converged, with a minor normalisation change toward higher SFRs with increasing resolution, but the peak location does not change with resolution. Doubling the wind velocity (“faster winds”) leads to a strong suppression of the overall star formation rate. Increasing the overall wind energy (“stronger winds”) leads to a clear overproduction of stars at late times. Variations in the AGN radio-mode feedback do not change the SFR density nearly as much as changes in the stellar feedback. Stronger radio-mode feedback leads to less star formation at late times. The same is true for an increased radio mode threshold, where more AGN feedback energy is channelled into the radio-mode. Since this mode is more bursty, it is more efficient at reducing star formation compared to the continuous quasar-mode AGN feedback, which mainly regulates the growth of BHs.

highest resolution runs is  $\lesssim 1.5$ , which we consider to be reasonably well converged. The overall shape of the cosmic SFR density is largely determined by stellar feedback at high redshifts and radio-mode AGN feedback towards lower redshifts. We find that the rapid decline of the SFR towards lower redshifts can only be achieved through strong radio-mode AGN feedback (see also Schaye et al. 2010; van de Voort et al. 2011; Bower et al. 2012, for example). In fact, in the absence of AGN feedback, but with the addition of stellar feedback, the cosmic SFR density would continue to rise beyond  $z = 0$ , since gas recycling and metal line cooling can support a large amount of star formation at late times (see also Schaye et al. 2010). We note in particular that the location of the peak of the SFR density does not change significantly with numerical resolution. The intermediate resolution run L25n256 is already sufficient to give a reasonably reliable estimate of the SFR in our simulation volume. We can hence study the effects of different physics parameterisations by running simulations at this intermediate resolution, as listed in Table 2.

The comparison among these different feedback models is shown in the right panel of Figure 6. Our fiducial model (L25n256) provides clearly the best match to the observational data compared to any of the other model variations presented in Table 2. The figure also highlights that the impact of changes in the wind model can be rather dramatic. For example, doubling the wind velocity (“faster winds”) leads to a strong suppression of the overall SFR, especially at late times. Such fast winds lead to a significant reduction of star formation also for massive haloes as we show below (see also Schaye et al. 2010, for a similar finding). Increasing the overall wind energy (“strong winds”) leads to a clear overpro-

duction of stars at late times, because a very substantial fraction of the gas that is blown out of galaxies at early times falls back in at late times – fueling further star formation along a “wind accretion” channel (see also Oppenheimer et al. 2010). The peak of the SFR density is also sensitive to the details of the wind and AGN parameterisation. Interestingly, the changes of the SFR density with respect to variations in the AGN radio-mode are less dramatic. As expected, “stronger radio” feedback leads to more efficient suppression of star formation at late times. Likewise, “weaker radio” mode feedback increases star formation at late times. Similar trends can be seen for changes in the radio threshold. A “higher radio threshold” puts more energy into the radio-mode and is therefore more efficient in suppressing star formation in massive systems at late times. A “lower radio threshold” on the other hand puts more AGN feedback energy into the quasar-mode, which is less efficient in suppressing star formation. Consequently, such a simulation produces more stars at late times. In fact, we find that quasar-mode feedback is mainly responsible in establishing the BH scaling relations, but does not significantly affect star formation in massive systems. The “no feedback” simulation, as expected, strongly overproduces the amount of stars at all times. However, the peak of the SFR occurs still at about the right time even for this simulation.

#### 4.2.3 Stellar mass – halo mass relation

The cosmic SFR density can be viewed as a convolution of the halo mass function and the amount of stars formed in a given halo (Springel & Hernquist 2003a). It is therefore natural to examine the average amount of stars formed as a function of halo mass. Over the

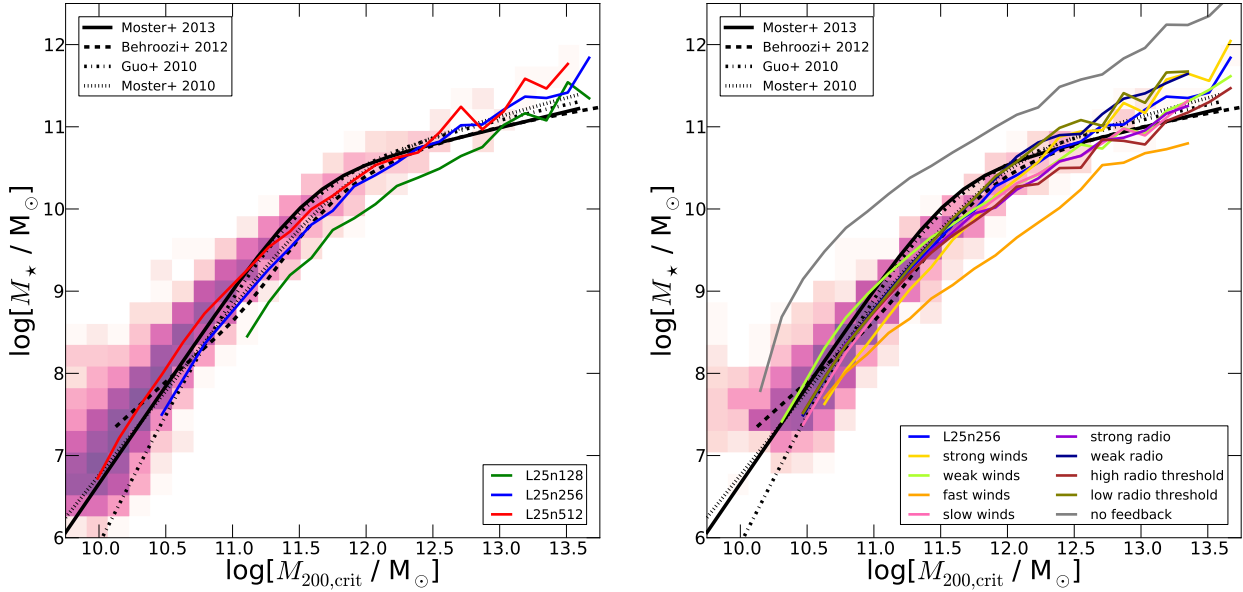


**Figure 7.** Stellar mass of central galaxies as a function of total halo mass ( $M_{200,\text{crit}}$ ) at  $z = 0$  (left panel: resolution study; right panel: various feedback models). Different black lines show abundance matching results (Moster et al. 2010; Guo et al. 2010; Behroozi et al. 2013; Moster et al. 2013), which are extrapolated beyond the constrained regime. Solid coloured lines mark the median relations of the simulations, whereas the two-dimensional histograms indicate the distribution of the L25n512 (left panel) and L25n256 (right panel) results. The left panel demonstrates that the stellar content of low mass galaxies (i.e.  $M_* < 10^9 M_\odot$ ) is not yet fully converged. But at somewhat higher galaxy masses (i.e.  $M_* > 10^9 M_\odot$ ), we find convergence in the stellar mass – halo mass relationship. The overall shape of the relation and the turnover mass agree reasonably well with the results derived based on abundance matching techniques. The right panel demonstrates that both stellar feedback at the faint end and AGN feedback at the massive end shape the stellar mass content. The wind speed has the most dramatic impact on the stellar mass content of haloes. “Faster winds” reduce the amount of stellar mass substantially over a large range of halo masses. “Weaker winds” clearly do not suppress star formation efficiently enough at the faint end. The massive end is most sensitive to changes in the radio-mode accretion rate threshold, where more radio-mode AGN feedback leads to more efficient quenching of massive systems. The same effect can be achieved through a larger radio-mode feedback strength.

last years, so-called abundance matching results have established the required relationship between the stellar mass content of haloes and their total mass (e.g., Conroy et al. 2006; Conroy & Wechsler 2009; Moster et al. 2010; Guo et al. 2010; Behroozi et al. 2013; Moster et al. 2013) in order to achieve consistency between the observed stellar mass function and the halo mass function of the  $\Lambda$ CDM cosmology. In Figure 7, we present the stellar mass – halo mass relation of our simulations at  $z = 0$  and compare it to the four abundance matching results of Moster et al. (2010); Guo et al. (2010); Behroozi et al. (2013); Moster et al. (2013). Specifically, we compare against the stellar mass – halo mass relation parameterisation

$$M_* = M_{200,\text{crit}} \times a \left[ \left( \frac{M_{200,\text{crit}}}{10^b M_\odot} \right)^c + \left( \frac{M_{200,\text{crit}}}{10^b M_\odot} \right)^d \right], \quad (31)$$

with the coefficients taken from Moster et al. (2010), Guo et al. (2010), and Moster et al. (2013). For Behroozi et al. (2013) we plot instead the provided tabulated data. Figure 7 shows the stellar mass of central galaxies as a function of their halo mass  $M_{200,\text{crit}}$ , where the stellar mass is measured within twice the stellar half-mass radius as discussed above. Again, the left panel of Fig. 7 shows a resolution study while the right panel explores the various physics settings. Solid lines mark the median relations, whereas the two-dimensional coloured histograms indicate the distribution of the L25n512 result (left panel) and L25n256 result (right panel).

The left panel of Figure 7 demonstrates that low mass galaxies (i.e.  $M_* < 10^9 M_\odot$ ) experience a factor of  $\lesssim 2$  increase in

their stellar masses as we increase the resolution. Although we do not expect similarly sized changes to the stellar masses of these galaxies with further increased resolution, the stellar masses of these low mass galaxies are clearly not yet fully converged. Galaxies with somewhat higher masses (i.e.  $M_* > 10^9 M_\odot$ ) are better resolved and show reasonable convergence in their stellar mass – halo mass relationship. As a result, the overall shape of the relation and the turnover mass are quite well converged and agree with the results derived based on abundance matching techniques. We note that the break in the stellar mass to halo mass ratio around  $M_{200,\text{crit}} \sim 10^{12} M_\odot$  can be reproduced only through a combination of stellar and AGN feedback. In fact, the main challenge in reproducing the abundance matching results is to correctly match the change of slope towards more massive systems. Reproducing the faint-end or massive-end slope alone is typically easier to achieve. Our simulation volume is too small to properly sample massive systems, but based on selected test calculations of clusters of galaxies using a zoom-in procedure, we have verified that our feedback model also reduces the stellar masses of these more massive systems to the observed levels

The right panel of Figure 7 demonstrates that both stellar feedback at the faint end and AGN feedback at the massive end are needed to produce a stellar mass – halo mass relation that matches the derived relation from abundance matching reasonably well. In agreement with our findings for the cosmic SFR density, the wind speed has the most dramatic impact on the stellar mass content of haloes, with “faster winds” being capable of substantially sup-

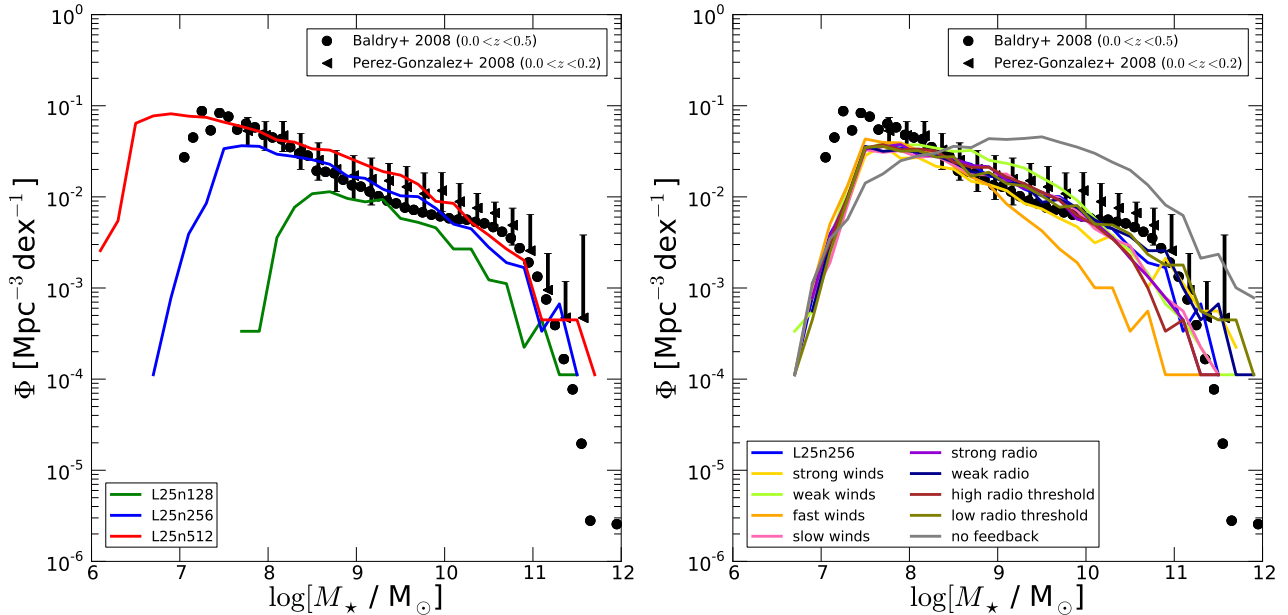


**Figure 8.** Stellar mass function at  $z = 0$  including all subhaloes (left panel: resolution study; right panel: different feedback models). Observational data points are taken from Baldry et al. (2008) and Pérez-González et al. (2008). The left panel shows that the stellar mass function is reasonably converged for higher mass systems (i.e.  $M_* > 10^9 M_\odot$ ). In the right panel the “faster wind” simulation leads to a strong reduction of stellar mass in agreement with similar findings for other diagnostics like the SFR density and the stellar mass – halo mass relation. The “weaker winds” simulation overproduces the number of galaxies at the faint end significantly, whereas the “strong winds” suppress star formation too much in these systems. A weaker radio-mode feedback leads to a less sharp drop of the stellar mass function towards the massive end. The same is true for a lower radio-mode accretion threshold since more energy goes then into the non-bursty quasar-mode AGN feedback, which is less effective at suppressing star formation.

pressing the stellar mass content of haloes over a wide mass range, also affecting more massive systems. “Weaker winds” in contrast clearly do not reduce star formation efficiently enough at the faint end. This can be seen from the “weaker wind” curve which significantly overproduces the stellar mass for low mass systems. On the other hand, “stronger winds” lead to an excessive suppression of star formation towards the low mass end, and also an undershoot around the turnover point of the observed relation. The massive end is very sensitive to changes in the radio-mode accretion rate threshold. Lowering this value, and thereby putting more AGN feedback energy into the quasar-mode, leads to an overproduction of stars in massive systems as can be seen from the “lower radio threshold” curve. The same is true if we decrease the radio feedback factor by a factor of two (“weaker radio” curve). These findings agree with the conclusions drawn from the cosmic SFR density plots. As for the cosmic SFR density, the fiducial L25n256 model provides the best fit to the observational data. The “no feedback” simulation clearly overproduces stars at all halo masses. Furthermore, the amount of stars scales nearly linearly with the halo mass in this case (above  $M_{200,\text{crit}} \sim 10^{10.5} M_\odot$ ), and there is clearly no turnover towards higher masses. This implies that radio-mode AGN feedback is crucial for the quenching of star formation at the massive end (as has been previously found by Croton et al. 2006; Bower et al. 2006; Cattaneo et al. 2006; Somerville et al. 2008; Puchwein et al. 2008; McCarthy et al. 2010; Teyssier et al. 2011; Dubois et al. 2013, for example).

We stress again that AREPO does not experience the “numerical quenching” of cooling in large haloes present in SPH simulations. This artificial quenching that occurs mainly in massive haloes helps to reduce the amount of star formation in these systems (see Vogelsberger et al. 2012), which implies that even without explicit

AGN feedback the stellar masses of massive haloes are pushed towards the observed relationship. Even though this is helpful in this sense, it is an undesirable effect as it is purely of numerical origin. In fact, it will then lead one to adopt physically incorrect settings for the radio-mode AGN feedback parameters.

#### 4.2.4 Stellar mass function

The shape of the stellar mass function is determined by the underlying halo mass function convolved with the efficiency at which stars can form in these haloes. As shown in the previous subsection, star formation in our simulations is most efficient for haloes with masses around  $M_{200,\text{crit}} \sim 10^{12} M_\odot$ , in agreement with abundance matching results. Star formation in lower mass haloes is suppressed through stellar feedback, whereas star formation in more massive systems is quenched by AGN feedback, as found in previous semi-analytic models (mainly, Bower et al. 2006; Croton et al. 2006) and more recently in self-consistent hydrodynamical simulations (e.g., Puchwein & Springel 2013). Especially, the exponential suppression at higher masses requires strong AGN feedback.

In Figure 8, we show the simulated  $z = 0$  stellar mass function and compare it to observational data of Baldry et al. (2008) and Pérez-González et al. (2008), with correction factors to account for our Chabrier IMF. Here we include all subhaloes and treat the stellar component of each as a galaxy contributing to the stellar mass function. As discussed above the stellar mass is measured within twice the stellar half-mass radius. The left panel of Figure 8 shows that the number density of galaxies at any given stellar mass increases marginally with resolution. This is directly tied to the increase in stellar mass for low mass haloes, as discussed in the previous subsection. Consistently with our previous discussion, we

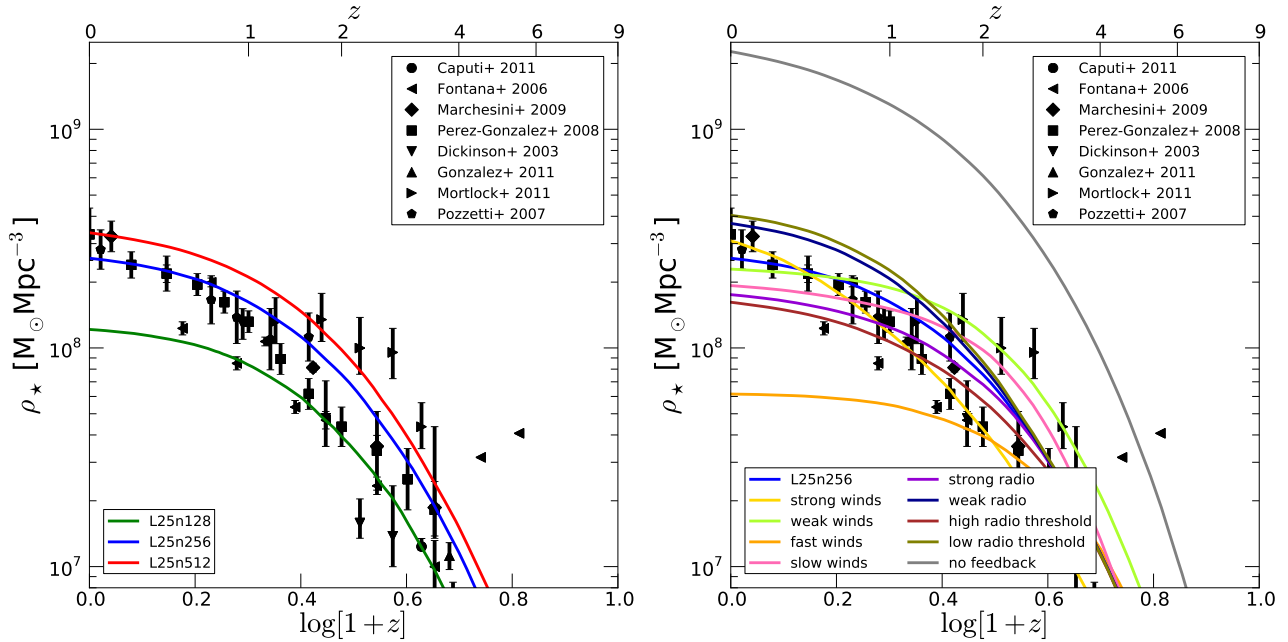


**Figure 9.** Stellar mass density as a function of redshift for the various models (left panel: resolution study; right panel: different feedback models). We compare the simulation results to observational data taken from Dickinson et al. (2003); Fontana et al. (2006); Pozzetti et al. (2007); Pérez-González et al. (2008); Marchesini et al. (2009); Mortlock et al. (2011); González et al. (2011); Caputi et al. (2011). The convergence is reasonable although the L25n512 simulation is clearly not yet fully converged (left panel). But both L25n256 and L25n512 have a stellar mass density which is consistent with the observations. The “no feedback” simulation strongly overproduces the amount of stellar mass, whereas the “faster winds” strongly underproduces it. All the other feedback variations are quite close to the fiducial model, which provides the best fit to the data. Changes in the radio-mode AGN feedback only affect the late time evolution of the stellar mass density.

find that the stellar mass function shows reasonable convergence for higher mass systems (i.e.  $M_* > 10^9 M_\odot$ ). But increasing the resolution allows an examination of progressively smaller galaxy masses. With our highest resolution simulation, we are able to compare to the observed stellar mass functions over quite a large range of masses. Although both functions differ in their detailed shape, we find that our simulated stellar mass functions are remarkably similar to the observations. This includes the slope of the low mass end of the stellar mass function, which is shaped by our stellar wind model, as well as the sharp drop towards the massive end, which is due to the radio-mode AGN feedback. We emphasise that the energy scaling of our stellar wind model is crucial to produce a very flat stellar mass function towards lower mass systems. Note that the mass loading for low mass systems can achieve very high values if an energy-scaling is adopted, and it grows more rapidly towards small galaxy sizes than for a momentum-scaling. A similar conclusion was reached by Puchwein & Springel (2013) who also argued for energy-driven winds to obtain a sufficiently flat stellar mass function for low mass systems (but see Oppenheimer et al. 2010, for arguments in favour of momentum-driven winds).

In the right panel of Figure 8, we explore variations around our fiducial model. The “faster wind” simulation leads to a strong reduction of stellar mass in agreement with similar findings for other diagnostics presented above. Such winds are capable of suppressing star formation even in more massive haloes. The other models behave largely very similarly. The “weaker winds” simulation overproduces the number of galaxies at the faint end significantly, whereas “stronger winds” suppress star formation too much in these systems. The “stronger winds” also lead to an undershoot of the stellar mass function around the cut-off scale. These findings are consistent with the ones presented above for the stellar mass –

halo mass relationship. A “weaker radio” mode feedback leads to a less sharp drop of the stellar mass function towards the massive end. The same is true for a lower radio-mode accretion threshold since in that case more energy goes then into the non-bursty quasar-mode AGN feedback. The “no feedback” simulation overproduces the number of galaxies at all stellar masses. Here the stellar mass function closely follows the shape of the halo mass function since most of the baryons in a halo can efficiently cool and form stars if not moderated by feedback. Note that the simulation without feedback does not show the strong exponential drop towards high mass galaxies masses. As for the stellar mass – halo mass relation, we hence argue that a quenching of star formation at the massive halo end requires AGN feedback.

#### 4.2.5 Stellar mass density

Integrating the cosmic SFR density leads to the overall stellar mass density in the Universe. In Figure 9 we show the stellar mass density of the total simulation volume as a function of redshift, comparing it to estimates based on observational data (Dickinson et al. 2003; Fontana et al. 2006; Pozzetti et al. 2007; Pérez-González et al. 2008; Marchesini et al. 2009; Mortlock et al. 2011; González et al. 2011; Caputi et al. 2011). We note that we here include all stellar mass formed in the simulation volume; i.e. we do not restrict ourselves to stellar mass associated with (sub)haloes or that has formed within a certain radial range in a halo. The reason for this is to make this diagnostic consistent with the cosmic SFR density (see Figure 6), which also includes all reservoirs of stellar mass formed without restriction.

Our fiducial model reproduces the observations reasonably



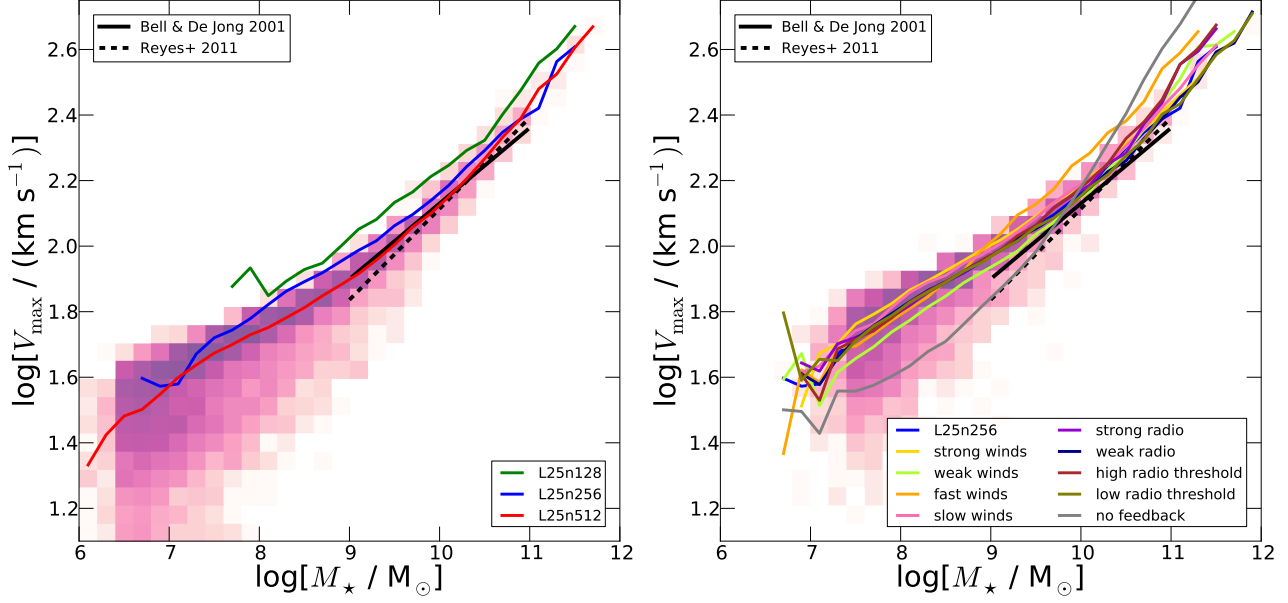


**Figure 10.** Tully-Fisher relation at  $z = 0$  (left panel: resolution study; right panel: different feedback models). Observational data is taken from Bell & de Jong (2001) and Reyes et al. (2012). Solid lines mark the simulation median relations, whereas the two-dimensional histograms indicate the distribution of the L25n512 result (left panel) and L25n256 result (right panel). The runs converge toward a relation which is very similar to the marked observed relation with the slope and normalisation of the simulated Tully-Fisher relation falling almost directly on top of the two marked observational Tully-Fisher relations. Most variations of the feedback model parameter choices lead to only minor changes in the resulting Tully-Fisher relation. The exception is the “faster wind” model which gives rise to the largest change in the Tully-Fisher relation by increasing the rotational velocity at a fixed stellar mass. This result is a consequence of the efficiency with which the fast wind model suppresses star formation.

well at all redshifts. As already seen above, the “faster winds” suppress star formation too strongly and therefore also significantly underpredict the total stellar mass density at nearly all redshifts but especially towards lower redshifts. Changes in the radio-mode lead, as expected, to differences in the late time behaviour since the radio-mode becomes dominant only at late times once more massive haloes with lower BH accretion rates form. For the radio-mode we also find the anticipated behaviour: a “stronger radio” mode reduces the total stellar mass density at late times, whereas a “weaker radio” mode leads to an increase. A similar trend can be seen for variations of the radio-mode accretion threshold. A higher threshold suppresses late time star formation compared to our fiducial model, which is in agreement with the findings above. The “no feedback” simulation strongly overproduces the amount of stars.

The left panel of Figure 9 demonstrates that the convergence of the overall amount of stellar mass is reasonable although the L25n512 simulation is clearly not yet fully converged. But both L25n256 and L25n512 have a stellar mass density at  $z = 0$  which is consistent with the observations. The non-converged L25n128 simulation clearly fails in this respect and has far too few stars at  $z = 0$  since it does not have adequate mass resolution. We note that such a low resolution does not even resolve the halo mass function properly for our simulation volume. It is therefore not surprising that the stellar mass is substantially underpredicted in that case.

#### 4.2.6 Tully-Fisher relation

The stellar mass and the circular velocity of disk galaxies are strongly correlated through the Tully-Fisher relation (Tully & Fisher 1977). Reproducing the Tully-Fisher relation, which ties together galactic mass, concentration, and angular momentum, is an important goal of any galaxy formation model (e.g., Steinmetz &

Navarro 1999; Sommer-Larsen et al. 2003; Robertson et al. 2004; Croft et al. 2009; Agertz et al. 2011; Scannapieco et al. 2012; Hummels & Bryan 2012). In Figure 10, we compare the  $z = 0$  Tully-Fisher relation of simulated galaxies with observational fits of the form

$$\log\left(\frac{V_{\max}}{\text{km s}^{-1}}\right) = \log\left(\frac{V_{\max,10}}{\text{km s}^{-1}}\right) + b \log\left(\frac{M_{\star}}{10^{10} M_{\odot}}\right), \quad (32)$$

where we take the coefficients from Bell & de Jong (2001) and Reyes et al. (2012). We note that Reyes et al. (2012) provide a fit to  $V_{80}$ , which is the rotation velocity measured at the radius containing 80% of the i-band galaxy light. However, as McCarthy et al. (2012) point out, this does generally not differ significantly from our diagnostic so we decided to compare to their results as well. Solid lines mark the median relations of the simulation, whereas the two-dimensional coloured histograms indicate the distribution of the L25n512 result (left panel) and L25n256 result (right panel). As before we measure the stellar mass within twice the stellar half-mass radius. For the plotted circular velocity, we measure the total mass within that radius and calculate the associated circular velocity (see also Scannapieco et al. 2012). We have experimented also with other measures of the circular velocity but found only very small variations. In particular, using  $V_{\max}$  of the subhaloes gives similar results.

Examining the different resolutions shown in the left panel of Figure 10, we find that there is good convergence for high mass systems, consistent with our previous findings. Furthermore our model converges towards a relation which is very similar to the observed relation, with the slope and normalisation of the simulated Tully-Fisher relation falling almost directly on top of the two observational Tully-Fisher determinations. We note that we did not select the galaxies in Figure 10 according to their type. This means that

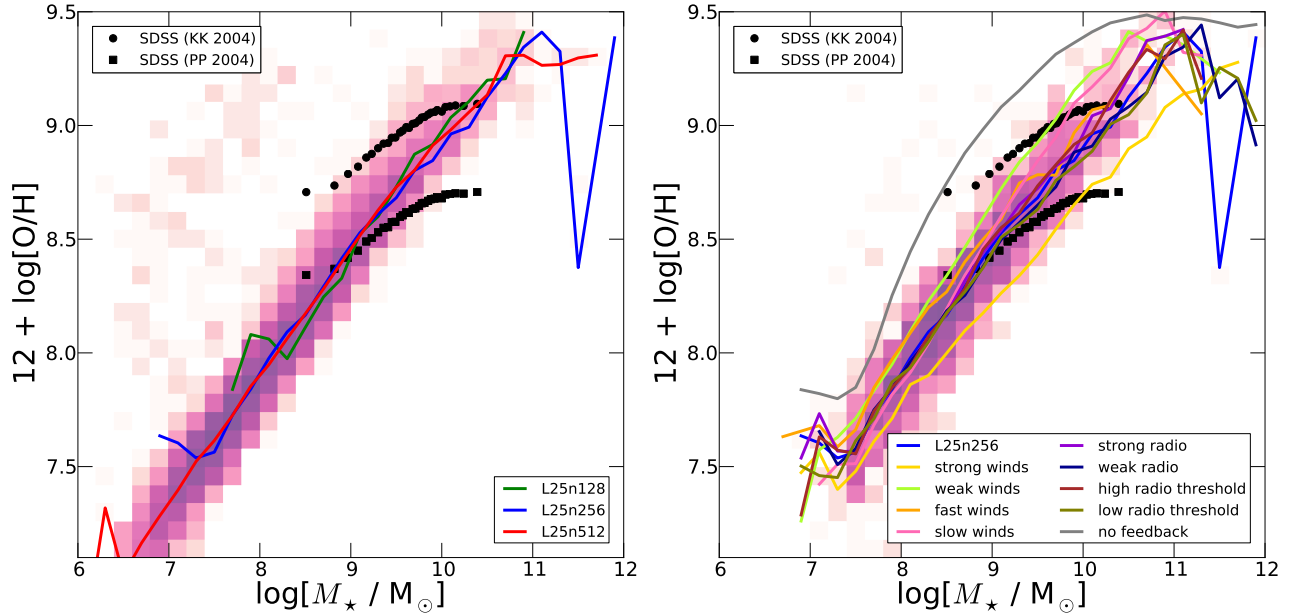


**Figure 11.** Mass–metallicity relation as a function of stellar mass (left panel: resolution study; right panel: different feedback models). Observational data is taken from SDSS DR7 (Abazajian et al. 2009). Solid lines mark the simulation median relations, whereas the two-dimensional coloured histograms indicate the distribution of the L25n512 (left panel) and L25n256 (right panel) results. The metallicity values are well-converged, but the relationship which they converge to does not perfectly match the observations. Specifically, the observed mass metallicity slope is shallower than the simulated slope, and there is no apparent turn-over in the simulated mass metallicity relation at high masses. However, the simulated mass metallicity relation falls between the PP04 and KK04 relations indicating that galaxies are retaining a reasonable fraction of their metals. The right panel shows that the simulated mass metallicity relation is quite sensitive to the adopted physics parameters since feedback variations strongly affect the amount of metals retained in galaxies and expelled to haloes.

especially at the more massive end our result will be influenced by a certain fraction of elliptical galaxies, implying that we should not expect perfect agreement with the observations in this regime.

In the right panel of Figure 10, we find that most variations in the feedback parameters do not induce significant changes in the resulting Tully-Fisher relation. The exception is the “faster wind” model which gives rise to the largest change in the Tully-Fisher relation by increasing the rotational velocity at a fixed stellar mass. This result is a consequence of the efficiency with which the fast wind model suppresses star formation, as seen previously in Figure 7. Aside from the “faster wind” model, we find that our feedback models are able to produce reasonable normalisations and slopes for the Tully-Fisher relation independent of the detailed feedback parameter choices. We therefore conclude that the Tully-Fisher relation is not very sensitive to the details of our physics parameterisation. In fact, among all the observables considered in this paper the Tully-Fisher relation is the most stable against variations of the underlying physics. However, the “no feedback” simulation clearly fails to reproduce this key observable.

#### 4.2.7 Mass-metallicity relation

Our stellar evolution and enrichment implementation allows us to study chemical abundances of galaxies in detail and confront those with observations. In Figure 11, we show the  $z = 0$  mass metallicity relation and compare it to SDSS DR7 data (Abazajian et al. 2009). Two distinct mass metallicity relations are shown. Although both use the SDSS data, one is the KK04 (Kobulnicky & Kewley 2004) nebular emission line diagnostic relation, while the other is the PP04 (Pettini & Pagel 2004) diagnostic. To facilitate this comparison, we have taken the metallicity values as tabulated in Zahid

et al. (2012) using the KK04 diagnostic and converted them to the PP04 diagnostic using the empirical relations of Kewley & Ellison (2008). The main reason for this procedure is to include the relevant information about the known uncertainty in the normalisation of nebular emission line metallicity indicators, and to avoid comparing our models to only one diagnostic method. We calculate the metallicity value for each simulated galaxy by finding the average oxygen to hydrogen abundance, weighted by the star formation rates of gas and excluding non-star forming gas from this calculation in order to provide a more straightforward comparison to observations, where the nebular emission lines naturally probe star-forming regions.

In the left panel of Figure 11, we find that the metallicity values are well-converged for our runs with varying resolution. In fact, the convergence is slightly better than in most of the other relations which we examine in this paper. However, the relationship which they converge to does not perfectly reproduce the observations. There are two main features that make the simulation results distinct from the observations. The first is that the observed mass metallicity slope is shallower than the simulated slope – regardless of whether we adopt the PP04 or KK04 diagnostic. The second issue is that there is no apparent turn-over in the simulated mass metallicity relation at high masses, unlike observed. Although there is a flattening visible for the two highest resolutions (L25n256, L25n512), this occurs at too large stellar masses and at too high metallicities to account for this observational signature. However, despite these shortcomings, the simulated mass metallicity relation falls between the PP04 and KK04 relations for most systems, which indicates that the simulated galaxies retain a reasonable fraction of their metals, in acceptable agreement with observations, on average (a similar level agreement was found in Davé et al. (2011a)).

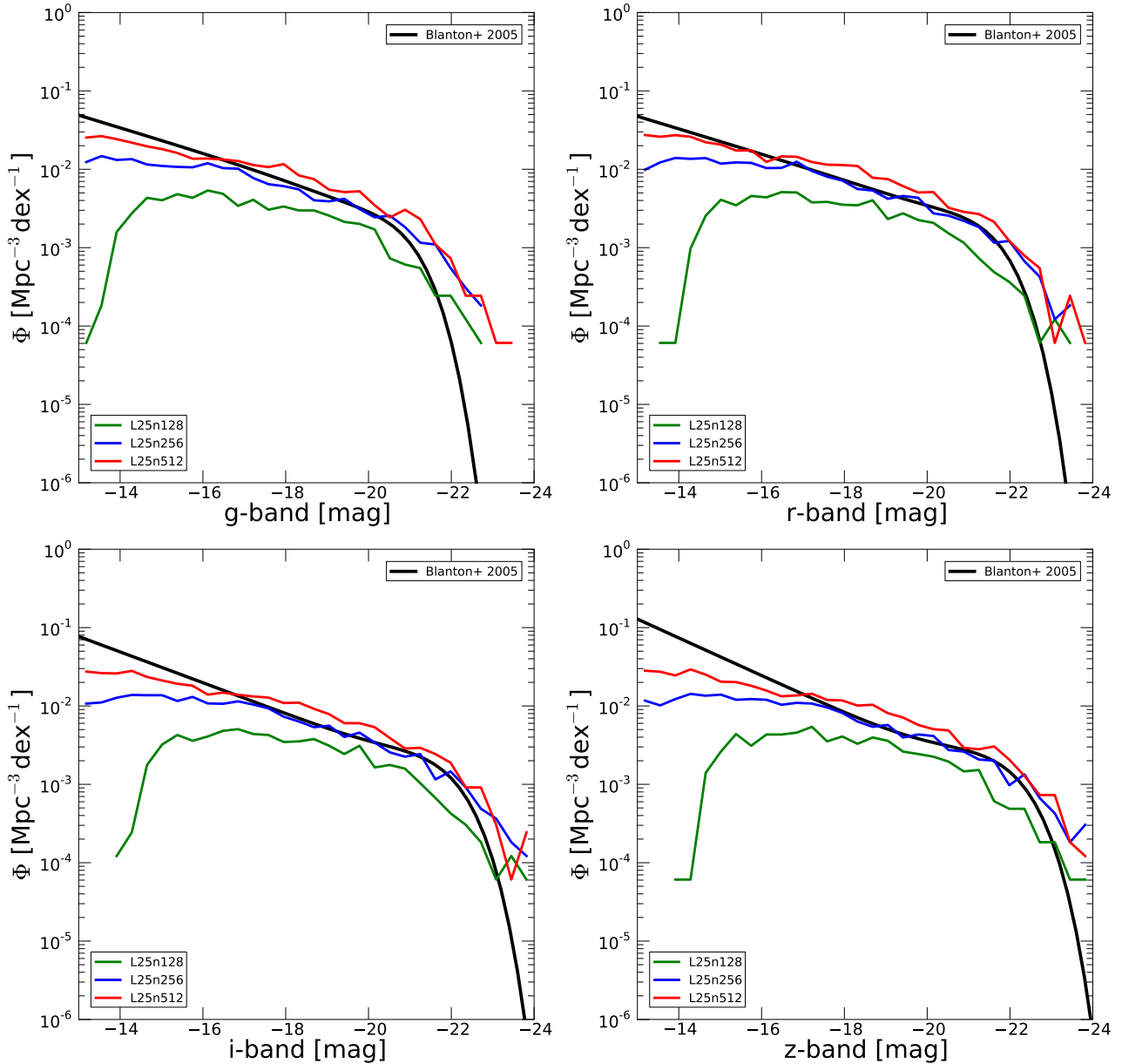


**Figure 12.** SDSS-band (g, r, i, z) luminosity functions for our simulated galaxy population (resolution study). We compare to double Schechter-fits of the observational data, taken from Blanton et al. (2005). We find a reasonable agreement of L25n256 and L25n512 with these fits. The faint-end slope agrees very well with the slope inferred from observational data, although the highest resolution simulations have a slightly too high normalisation. Also, the exponential suppression is reasonably well reproduced but starts at slightly too bright galaxies. This discrepancy is largest for the g-band luminosity function.

We note that this agreement has become possible only through the independent treatment of mass and metal loading of stellar winds. As described above, we have adopted a wind metal loading factor ( $\gamma_w$ ), which determines the metallicity of the wind material relative to the local ISM metallicity from where the wind is launched. Without such a scheme our galaxies would retain too few metals due to the large wind mass loadings required to match the observed stellar masses of lower mass systems. This creates an interesting tension between the need for high wind efficiencies to reduce the buildup of stellar mass in low mass galaxies, and the need for low mass galaxies to be relatively efficient at retaining their metal content (Zahid et al. 2012). The solution to this tension likely either lies in: (i) fundamentally reducing the accretion efficiency of

low mass galaxies via some feedback mechanism that is able to disrupt and heat the IGM around these systems, or (ii) in a more detailed wind model that self-consistently handles the entrainment of low metallicity material as winds propagate out of galaxies (e.g., Hopkins et al. 2012c).

An interpretation of the differences between the simulated mass metallicity relation and the observed relation is guided by the right panel of Figure 11. We find that the simulated mass metallicity relation is quite sensitive to the adopted feedback physics parameters. The reason for this behaviour is that the level of central galactic metallicity is easily reduced if we encourage mixing between the central galaxy gas and the halo gas, which is mediated by AGN or stellar feedback. Our winds, which by construction transport highly

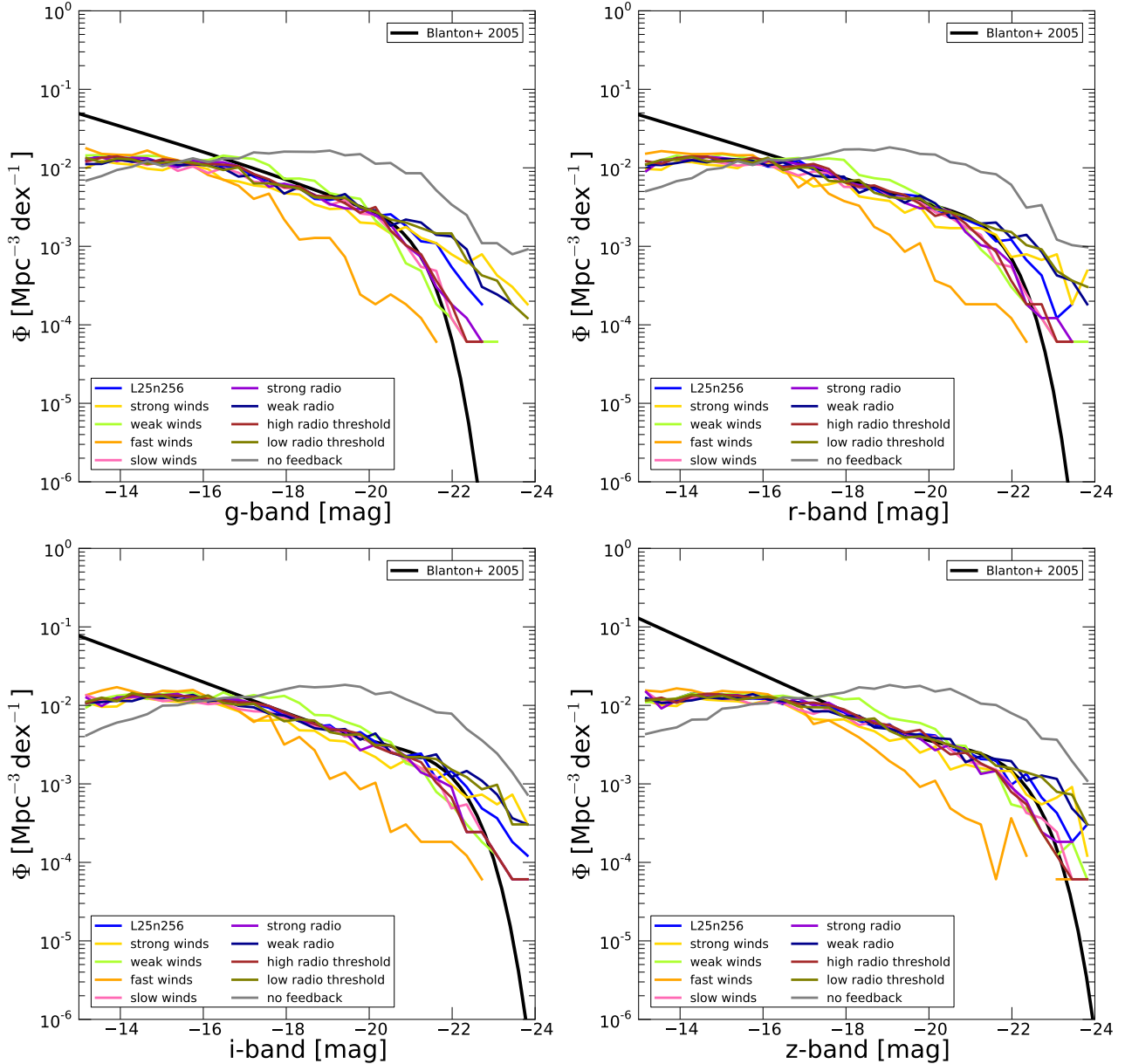


**Figure 13.** SDSS-band luminosity ( $g$ ,  $r$ ,  $i$ ,  $z$ ) functions for our simulated galaxy population (different feedback models). We compare to observational double Schechter-fits taken from Blanton et al. (2005). Our fiducial model reproduces the observational fit reasonably well. Models with faster winds clearly give the poorest agreement. Weakening the radio-mode AGN feedback leads to a significant overshoot of the luminosity function at the bright end. “Weaker winds” lead to an overproduction of faint galaxies. The “no feedback” simulation clearly fails dramatically in reproducing the observed luminosity function. Interestingly, a model with a high radio-mode threshold leads to a better agreement for the bright end in all bands.

enriched disk gas into the halo, are very efficient at mixing metals. Thus, when we use a “weaker wind” prescription we find that the average metal content of the central dense galaxy gas goes up. On the other hand, if we employ “stronger winds” we find that the average metal content goes down. The need to regulate the growth of low mass galaxies successfully while at the same time avoiding overly depleting galaxies of their metal content prompted us to implement a specific wind metal loading, as described above. We note that variations in the AGN radio-mode alone are not able to remove the metallicity tension at the high mass end. Most of the simulations overshoot the amount of metals in massive galaxies by 0.3 – 0.5 dex.

#### 4.2.8 Luminosity function

We can use the stellar population synthesis models described above to derive luminosities of individual galaxies in various bands. We here confront the resulting galaxy luminosity functions with SDSS observations. We note that we neglect the impact of dust attenuation, and simply define the luminosity of each galaxy as the sum of the luminosities of all its star particles. In Figure 12 we show the  $g$ -,  $r$ -,  $i$ -, and  $z$ -band luminosities (other bands are compared to observations in Torrey et al. (2013); there we also include a crude model

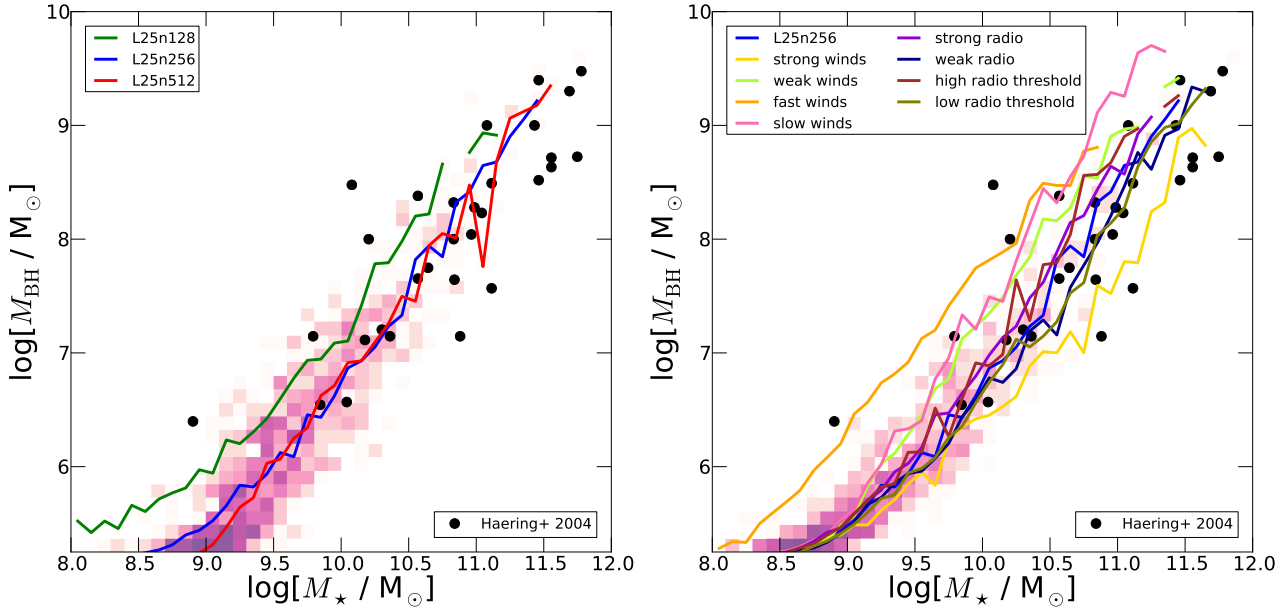


**Figure 14.** Black hole mass – stellar mass relation (left panel: resolution study; right panel: different feedback models). Observational data is taken from Häring & Rix (2004). The BH mass – stellar mass relation is well-converged and agrees with the observations both in slope and in normalisation. Also the amount of scatter is in reasonable agreement with the observational data. Normalisation changes in this relation are mainly due to changes in the stellar mass caused by the different feedback choices. For example, “fast winds” strongly reduce the amount of stars forming in haloes, as demonstrated above. We note that the right panel does not include the “no feedback” simulation since this run did not include any BHs.

for dust attenuation) and compare them to double Schechter-fits

$$\Phi(M) = 0.4 \ln 10 \, dM \exp \left( -10^{-0.4(M-M_*)} \right) \quad (33)$$

$$\left[ \phi_{*,1} 10^{-0.4(M-M_*)(\alpha_1+1)} + \phi_{*,2} 10^{-0.4(M-M_*)(\alpha_2+1)} \right],$$

from SDSS, where we take the fitting parameters  $M_*$ ,  $\phi_{*,1}$ ,  $\phi_{*,2}$ ,  $\alpha_1$ , and  $\alpha_2$  from Blanton et al. (2005). We find a reasonable agreement of L25n256 and L25n512 with these fits. Especially the faint-end slope agrees well with the Schechter-fit slope inferred from observational data, although the highest resolution simulation has a slightly too high normalisation. Also the exponential suppression at the bright end is reasonably well reproduced, although for most bands the suppression starts at slightly too bright galaxies. We will demonstrate in Torrey et al. (2013) that we also find good agreement of the simulated B-band luminosity function compared to observations at various redshifts. Interestingly, the g-band luminosity function shows the worst agreement with the observations at the bright end. For all other bands the exponential drop is significantly better reproduced. Furthermore, we find that the simulated luminosity function is well converged even at the faint end. We caution however that this comparison does not account for dust attenuation.

We compare the luminosity functions of the different feedback models to the observational fits in Figure 13. Our fiducial L25n256 model gives a good fit to the observed luminosity function, whereas a model with “faster winds” clearly gives the worst agreement. Weakening the radio-mode AGN feedback leads to a significant overshoot of the luminosity function at the bright end. “Weaker winds” cause an overproduction of faint galaxies. Finally, the “no feedback” clearly fails dramatically in reproducing the observed luminosity function, as it did for the stellar mass function. Interestingly, the “higher radio threshold” simulation produces luminosity functions which are in better agreement with the observations than our fiducial model. This is true for all bands, where the

exponential drop at the bright end is systematically in better agreement with the observational data for the “higher radio threshold” simulation. Also the model with “stronger radio-mode” feedback leads to a better agreement of the luminosity functions in all bands for the bright end. However, although these two models agree better with the observed luminosity functions, their stellar mass functions do not agree as well with the observations as our model with the fiducial feedback settings.

#### 4.2.9 Black hole mass – stellar mass relation

The BH mass growth is mainly regulated by quasar-mode feedback which together with the BH accretion yields a tightly self-regulated feedback loop. As a result, a BH mass – stellar mass relation is expected to be produced through these two processes (see also Springel et al. 2005b; Di Matteo et al. 2005). Here we compare the BH mass – stellar mass relation to observational data of Häring & Rix (2004). As the left panel Figure 14 demonstrates, the implemented quasar-mode model leads to the correct growth of BHs in our simulation. Most important, we reproduce the correct slope of the relation. This demonstrates that the modifications of the original Springel et al. (2005b) model described above, do not affect the BH mass – stellar mass relation in any significant way. Reproducing this relation is also crucial to inject the correct amount of radio-mode AGN feedback generated by these BHs and to create the appropriate radiation field used for the radiative (EM) AGN feedback. We note that we do not plot the stellar bulge mass in Figure 14 but rather the stellar mass within twice the stellar half mass radius, as discussed above. Correcting for the bulge mass does however not affect the conclusions of this subsection. We will in forthcoming work study this relation in more detail using extracted bulge masses (Sijacki et al, in prep).

The left panel of Figure 14 also shows that our BH mass –

stellar mass relation is well converged and agrees with the observations both in slope and in normalisation. Also, the amount of scatter is in reasonable agreement with the observational data. The right panel of Figure 14 demonstrates that the slope of this relation does not change significantly if we alter the stellar or radio-mode AGN feedback. We note that this plot does not include the “no feedback” simulation since this run did not include BHs due to the absence of any BH growth regulating feedback mechanism. Normalisation offsets in this relation are mainly due to the changes in the stellar masses caused by the different feedback choices. For example, “faster winds” strongly reduce the amount of stars forming in haloes. This implies that the low mass stellar systems end up with too massive BHs at their centres, as can be seen in the right panel. Overall we find that our fiducial model reproduces the BH mass – stellar mass relation reasonably well.

### 4.3 Disentangling the impact of different physical processes

So far we have explored feedback variations around our fiducial model, varying the strength of stellar and AGN feedback. In this subsection, we briefly discuss the impact of the different physical effects on the cosmic SFR density, the stellar mass function, the stellar mass – halo mass relation, and the stellar mass density. Most of the simulations presented here are unrealistic in the sense that they deliberately ignore important processes required to shape the galaxy population. But they are useful for demonstrating the impact of these physical processes and how they influence the galaxy population. In particular, we discuss the importance of our newly implemented radiative AGN feedback scheme and demonstrate the impact of our wind metal loading scheme.

It is instructive to consider a simulation set with increasing model complexity, starting from a physics setup close to the simulations presented in Vogelsberger et al. (2012) and ending at the full physics implementation discussed above. The different simulations of this series are summarised in Table 3. The “plain” simulation differs only in terms of the IMF (Chabrier instead of Salpeter), a softer eEOS ( $q = 0.3$  instead of  $q = 1.0$ ) and self-shielding corrections from the simulations presented in Vogelsberger et al. (2012). We then add more physical processes on top of this plain setup, where the parameters of the individual physics modules are chosen according to our fiducial setup discussed above (see Table 1). We start with the simulation MeGa, which includes on top of the “plain” setup metal-line cooling and gas recycling. This simulation is identical to the “no feedback” simulation presented in the previous section. The last simulation listed (MeGaWiMIQuEmRa) includes all physical effects discussed above and is identical to the fiducial L25n256 simulation. Table 3 also includes a simulation which is similar to L25n256; i.e. our full fiducial model, but without stellar feedback (NoWindFeed). This simulation is useful for studying the detailed impact of stellar feedback, but still considering all the other physical processes included in our model. We note that MeGaWiMI explores the situation with full stellar feedback, but without AGN feedback.

The upper left panel of Figure 15 shows the cosmic SFR density for the different simulations, whereas the upper right panel presents the stellar mass function. We do not include observational data in these plots for graphical clarity and because a detailed comparison to the observational data was already presented above. Going from the “plain” model to the model which includes in addition metal-line cooling and gas recycling (MeGa=“no feedback”) strongly increases the star formation rates since net cooling rates are increased and recycled gas can form additional stars. However,

name	physics
plain	same as in Vogelsberger et al. (2012) (except for IMF, softer eEOS, self-shielding)
MeGa	+ met. line cool., gas recycl. = “no feedback”
MeGaWi	+ stellar winds
MeGaWiMI	+ separate metal mass loading of winds
MeGaWiMIQu	+ quasar-mode AGN feedback
MeGaWiMIQuEm	+ electro-magnetic AGN feedback
MeGaWiMIQuEmRa	+ radio-mode AGN = L25n256
NoWindFeed	L25n256 without stellar feedback

**Table 3.** Summary of simulation series with increasing physics complexity, starting from a setup similar to the simulations presented in Vogelsberger et al. (2012) except for the IMF (Chabrier instead of Salpeter), the softer eEOS ( $q = 0.3$  instead of  $q = 1.0$ ) and self-shielding corrections for cooling (“plain”). The other simulations include additional physical processes as listed. The adopted parameters for these processes are the same as those of our fiducial model (see Table 1). The MeGaWiMIQuEmRa run includes the same physics as the L25n256 simulation presented above. We also performed one other simulation which is identical to L25n256 except for turning off the stellar feedback (NoWindFeed).

such a model still correctly produces a star formation rate peak although at a slightly different redshift compared to the “plain” and full MeGaWiMIQuEmRa setup. Including stellar winds (MeGaWi) regulates this behaviour at early times by strongly suppressing the star formation in low mass systems. This implies that a significant amount of gas is not turned into stars at high redshifts in this simulation. This gas is then available for star formation at late times, which results in a rising SFR density towards lower redshift. Metal line cooling and gas recycling are so efficient then that the SFR density almost does not decline. In fact, a substantial decline can be achieved to a sufficient degree only by including radio-mode AGN feedback as demonstrated by the MeGaWiMIQuEmRa curve.

The MeGaWiMI simulation employs our new metal loading scheme for outflows. Reducing the metal loading of winds from  $\gamma_w = 1$  (MeGaWi) to our fiducial  $\gamma_w = 0.4$  (MeGaWiMI) decreases the star formation rate slightly towards lower redshifts. This is because less enriched winds lead to less enriched gaseous haloes. As a result, these haloes then experience less metal-line cooling yielding a lower gas supply to central galaxies such that the star formation rate decreases. Although this effect is clearly visible, we note however that it does not represent a substantial change in the star formation rates, which is clearly largely shaped by feedback processes. As we discussed above, such a metal loading scheme is required to retain enough metals in galaxies and to obtain a reasonable match to the galaxy mass–metallicity relation. In fact,  $\gamma_w = 1$  would lead to a far too small normalisation of the mass–metallicity relation.

Comparing the MeGaWiMI simulation with a run that additionally includes quasar-mode AGN feedback (MeGaWiMIQu) demonstrates that continuous thermal AGN feedback has no significant effect on the global star formation rates. The MeGaWiMIQu simulation differs from the MeGaWiMIQuEm only by radiative electro-magnetic AGN feedback, which is included in the latter. Most importantly, this causes quasar-mode feedback to have a slightly more noticeable effect on the star formation rates; i.e. our new radiative feedback is stronger than the continuous thermal AGN feedback of our quasar-mode feedback implementation alone. Radiative AGN feedback leads to a suppression of atomic cooling and to an increase of the heating rates, so that star forma-

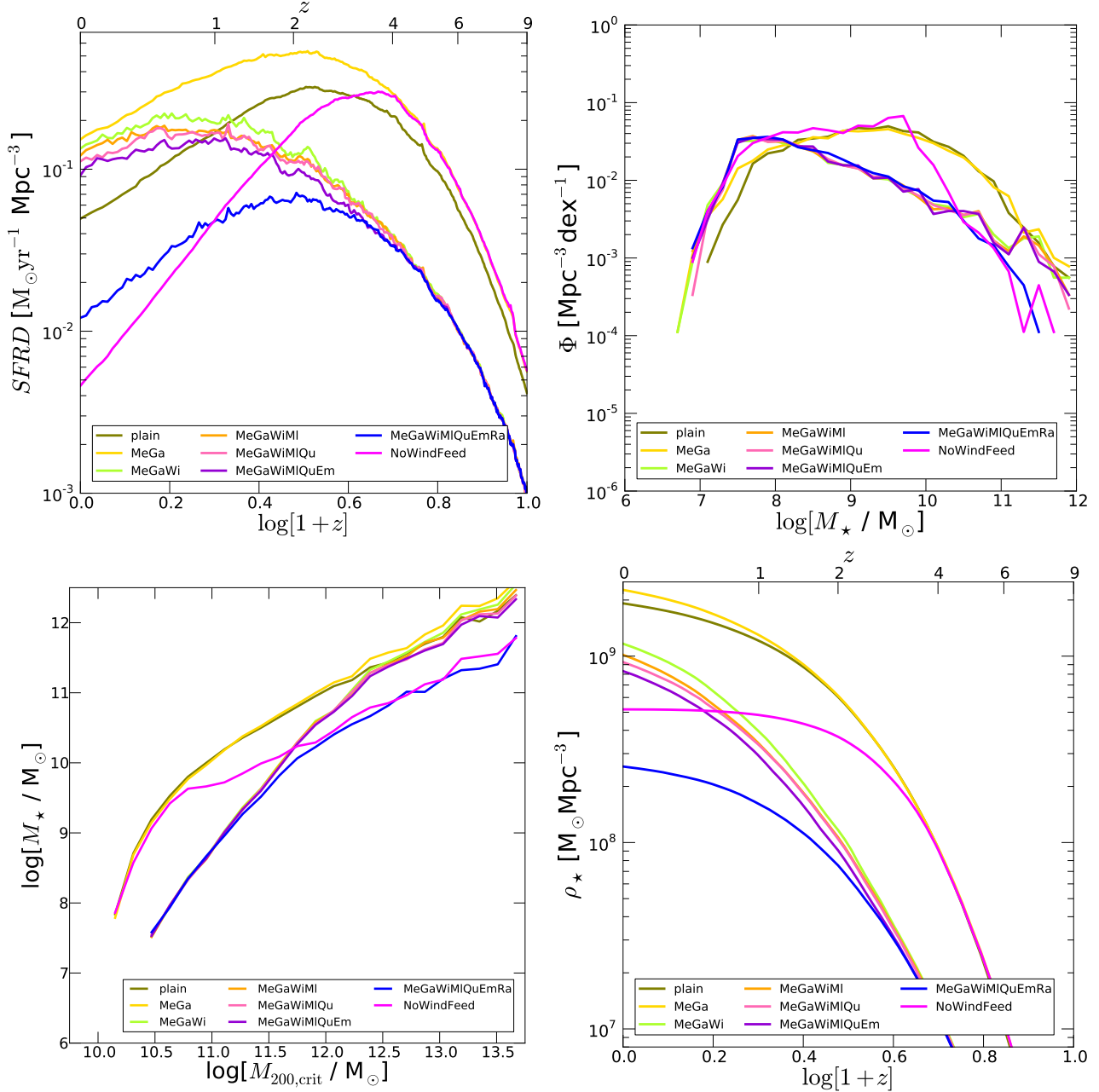


**Figure 15.** Cosmic SFR density (upper left panel), stellar mass function (upper right panel), stellar mass – halo mass relation (lower left panel) and stellar mass density (lower right panel) of simulations with increasing modelling complexity (see Table 3). The “plain” setup does not include any explicit stellar and AGN feedback. The MeGaWiMIQuEmRa simulation includes all physical processes discussed above with parameters set as for our fiducial model (see Table 1). Although most of these simulations are unrealistic since they miss important physical ingredients, they are helpful in disentangling the impact of various physical processes on the galaxy population. Simulations including stellar winds, but no radio-mode AGN feedback, lead to a significant overproduction of stars at late times. This can only be regulated by strong radio-mode AGN feedback. Quasar-mode feedback alone has essentially no effect on the star formation (see MeGaWiMI vs. MeGaWiMIQu). However, radiative (electro-magnetic) AGN feedback leads to a minor reduction of the star formation rate. Changing the metal loading of stellar winds (MeGaWi vs. MeGaWiMI) has about the same effect on the star formation rate. As expected, stellar feedback regulates star formation in low mass systems, whereas the stellar content of higher mass haloes is mainly set through radio-mode AGN feedback.

tion is further suppressed by this feedback channel. This can be seen in the cosmic SFR density, where we find a lower star formation rate once quasars become active. Although the effect is visible in the star formation rates, it is not particularly strong compared to radio-mode AGN feedback, which is implemented in the MeGaWiMIQuEmRa simulation. The reason is that electro-magnetic AGN feedback is effective when the accretion rate is near Eddington in

the quasar regime, which typically happens only for short periods of cosmic time for any given BH. This questions previous claims suggesting that such radiative feedback is a highly important and very efficient feedback channel compared to thermal and mechanical AGN feedback (e.g., Gnedin & Hollon 2012). We stress however that we focus here only on the effect of electro-magnetic feedback on the amount of stellar mass formed, and not do analyse the

impact of the AGN radiation field on the surrounding IGM, for example.

Finally, the MeGaWiMIQuEmRa simulation has an equivalent setup as the L25n256 simulation presented above. It includes all its processes and uses the same parameterisation as our fiducial model (see Table 1). Clearly, radio-mode feedback leads to a strong suppression of star formation at late times in massive haloes. This induces a steep decline of the cosmic SFR density and an exponential drop of the stellar mass function towards massive haloes. The NoWindFeed run, which does not include winds, but is otherwise identical to L25n256, does not show any star formation suppression at early times such that the overall normalisation of the SFR density is significantly too high. We conclude that late time star formation is largely shaped by metal line cooling, gas recycling and radio-mode AGN feedback. The high-redshift SFR density, on the other hand, is essentially only determined through stellar feedback. Metal line cooling and gas recycling have essentially no effect in that regime. This is expected since not many stars formed at higher redshifts such that no significant amount of metals is available and also mass return of stars is not important at these early times.

The upper right panel of Figure 15 demonstrates the effect of our physics implementation on the stellar mass function. Clearly, models without any feedback (“plain” and MeGa) lead to a substantial overproduction of stars. This is also true for the simulation without any explicit stellar feedback (NoWindFeed). The incorporation of winds is the main driver for the low mass slope of the stellar mass function. The separate metal loading of these winds has essentially no impact on the stellar mass function (MeGaWi vs. MeGaWiMI). The bright end is largely shaped by radio-mode AGN feedback, which starts to dominate around  $M_* \sim 10^{11} M_\odot$ . Also radiative (electro-magnetic) AGN feedback has only a rather minor impact on the massive end of the stellar mass function.

The lower left panel of Figure 15 shows the stellar mass – halo mass relation. For clarity we only show the median relations here. As expected, simulations without stellar feedback (“plain”, MeGa, NoWindFeed) lead to a large overproduction of stellar mass for lower and intermediate mass systems. The addition of stellar winds leads to about an order of magnitude suppression of stellar mass. The inclusion of quasar-mode and radiative (electro-magnetic) AGN feedback does not significantly affect the massive end. Only the simulation with radio-mode AGN feedback (MeGaWiMIQuEmRa) leads to a reduction of stellar mass for higher mass systems, resulting in the correct turnover behaviour of the stellar mass – halo mass relation.

The lower right panel of Figure 15 shows the stellar mass density as a function of redshift; i.e. the integrated version of the upper left panel. Here we find a behaviour similar to what we found for the other three diagnostics discussed so far. The lack of stellar feedback in the “plain”, MeGa and NoWindFeed simulations strongly overproduces the stellar mass density already at high redshifts. Radio-mode AGN feedback on the other hand strongly reduces the number of stars formed at later times (MeGaWiMIQuEmRa). All other curves follow in a narrow range between these extremes.

We conclude that the stellar content of haloes is largely dominated by stellar feedback and radio-mode AGN feedback. Other model details, like the independent metal loading of winds or radiative (electro-magnetic) AGN feedback lead only to very minor changes in the stellar mass, although they can have important consequences for other observables, such as the galaxy mass-metallicity relation in the case of wind metal-loading.

## 5 SUMMARY AND CONCLUSIONS

Matching the enormous amount of low redshift observational data is a great challenge for any galaxy formation model that tries to explain the galaxy population from first principles. Especially in the era of “precision cosmology” based on large surveys like SDSS, LSST, etc., it is crucial to have predictive, accurate and reliable galaxy formation models to test our understanding of structure formation by confronting these models with a plethora of data. The most general self-consistent way to study structure formation is through hydrodynamical simulations which follow the coupled evolution of dark matter, dark energy and baryonic physics. This task requires two main ingredients: (i) a highly reliable and computationally efficient scheme to solve the basic hydrodynamical and gravity equations, and (ii) a well-motivated and numerically meaningful model for the required physics of galaxy formation.

We have recently demonstrated that a moving-mesh approach for solving the underlying gas dynamics is very attractive for cosmic structure formation and offers advantages compared to other numerical schemes for galaxy formation simulations (Springel 2010; Vogelsberger et al. 2012; Kereš et al. 2012; Sijacki et al. 2012; Torrey et al. 2012; Bauer & Springel 2012; Nelson et al. 2013). This approach hence addresses requirement (i). The natural next step is to equip this new numerical scheme with the relevant physical processes to fulfil requirement (ii), with the goal of carrying out studies of galaxy formation in large volumes with higher accuracy and fidelity to the physics than possible thus far.

Along these lines, we have presented in this paper the first galaxy formation implementation for the moving-mesh code AREPO specifically aimed towards large-scale cosmological hydrodynamics simulations. Our objective has been to construct a model which results in a realistic galaxy population, similar to what the best semi-analytic models achieve, yet realised in a self-consistent hydrodynamical simulation of galaxy formation. This is an important next step in galaxy formation theory and promises a much higher predictive power from the theoretical models.

Our star formation prescription (see Section 2.2) models star-forming dense ISM gas with an effective equation of state, where stars form stochastically above a certain density threshold. To reach these densities, gas cools through primordial and metal-line cooling in the presence of a photo-ionising UV background with self-shielding corrections (see Section 2.4). Primordial cooling is treated with a self-consistent chemical network, whereas metal-line cooling rates are tabulated based on CLOUDY calculations. Both processes include self-shielding corrections from the otherwise spatially uniform UV background radiation. We follow stellar evolution and chemical enrichment processes based on AGB, SNIa and SNII yields and account for stellar mass loss processes (see Section 2.3). For the chemical enrichment we follow nine elements (H, He, C, N, O, Ne, Mg, Si, Fe). Stellar feedback effects are based on a kinetic outflow prescription, where stellar winds are either non-locally driven from the ISM gas directly or locally around evolving stellar particles (see Section 2.5). Our implementation supports energy- and momentum-driven winds or a combination of both, although in practice we prefer energy-driven winds since they provide a better fit to the faint-end of the stellar mass function. We introduce a novel wind metal mass loading scheme, which allows us to decouple mass and metal loading for gas put into the outflowing wind (see Section 2.5.3), which is required to match the mass–metallicity relation and stellar mass function for low mass galaxies simultaneously. We also follow black hole growth and include quasar- and radio-mode feedback pro-



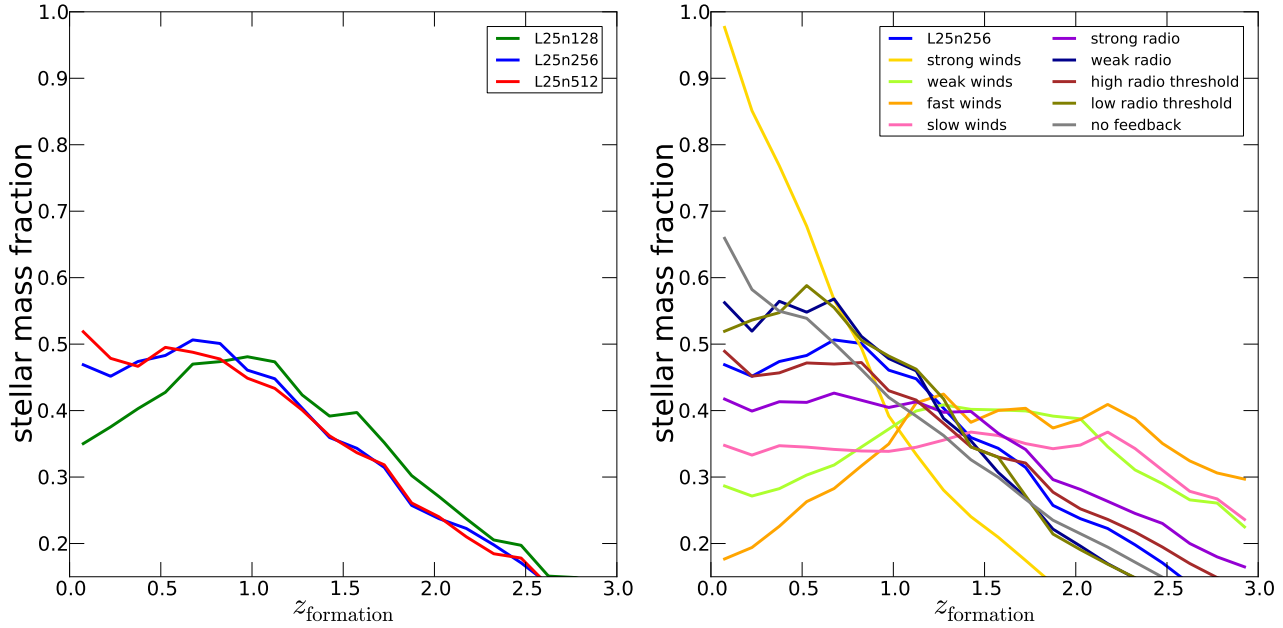


**Figure 16.** Distribution of star formation times for all stars at  $z = 0$  (left panel: resolution study; right panel: different feedback models). Stellar formation times are well converged. The feedback variations strongly affect when stars form in the simulation. The most extreme feedback models are the simulation with “strong winds”, which leads to a great deal of late-time star formation, and the simulation with “faster winds”, which yields almost no late-time star formation. All other feedback variations fall more or less between these two extreme setups.

cesses (see Section 2.6). Furthermore, we introduce a novel model for radiative (electro-magnetic) AGN feedback (see Section 2.6.4), which is implemented assuming an average AGN SED and a bolometric, luminosity-dependent scaling to take into account obscuration effects. Finally, we introduced inlined analysis techniques for gas tracking in the form of classical Lagrangian velocity field tracer particles and a new Monte Carlo based scheme, and we added on-the-fly visualisation routines to allow for direct volume rendering through a ray casting technique while the simulation is running.

The scope of the paper is to present our galaxy formation implementation, to identify a fiducial model with promising settings of the feedback parameters, and to show some basic results for the newly added physics that are compared with some key observations at  $z = 0$ . To this end, we have explored three different sets of simulations: one resolution study using our fiducial feedback parameters with a maximum resolution of  $2 \times 512^3$  resolution elements in a  $(25 h^{-1} \text{ Mpc})^3$  simulation volume, a set of simulations where we slightly modified the strength of stellar and radio-mode AGN feedback to explore changes in the feedback prescriptions, and simulations where we systematically explored the impact of various physical processes by specifically deactivating certain parts of our model.

Our fiducial feedback parameters were chosen to be physically plausible and set such that they reasonably well reproduce key observations at  $z = 0$ . We note that the stellar and radio-mode AGN feedback settings of this fiducial model differ significantly from those previously used in SPH simulations. Most important, the AGN radio-mode feedback is more energetic than adopted earlier. These energetic feedback processes are required to match the  $z = 0$  stellar mass function and stellar mass – halo mass relation. Such a need for stronger feedback was already pointed out in Vogelsberger et al. (2012) and Kereš et al. (2012) where it was demonstrated that AREPO shows significantly more efficient gas cooling compared to previous SPH simulations, which is mainly

due to spurious viscous heating effects in SPH and the lack of a proper cascade of subsonic turbulent energy to small scales. This in turn results in an overall increase of star formation by a factor of two towards lower redshifts (Vogelsberger et al. 2012) and also a stellar mass function which significantly overpredicts the number of massive systems (Kereš et al. 2012). Stronger feedback needs to compensate for this increase in cooling and star formation. The artificial heating effect of SPH is largest for high mass systems where a quasi-hydrostatic hot atmosphere can form. SPH simulations suffer here a form of “numerical quenching”, reducing the amount of AGN feedback required in this technique to regulate the amount of stars forming in these systems. Since AREPO does not suffer from this unphysical effect, we need to invoke a corresponding increased radio-mode feedback strength.

The feedback variations explored in this paper are summarised in Table 2. We only varied the strength of stellar and radio-mode feedback since those influence star formation most significantly. These modifications also affect the times at which stars form in the simulation (see Figure 16) and therefore many of the key observables studied above are significantly altered by these feedback changes. The most extreme feedback models, in terms of stellar formation times, are our simulations with “stronger winds”, which produces too much late-time star formation, and the simulation with “faster winds”, which leads to almost no late-time star formation. All other feedback variations fall more or less between these two extreme setups. “Weaker winds” lead, as expected, to more star formation at higher redshifts. Weakening the radio-mode AGN feedback results in more late time star formation, whereas a stronger radio-mode feedback has the opposite effect. Interestingly, a simulation without any feedback leads to a lower late-time star formation rate than the model with very strong winds. The reason is that strong winds very efficiently suppress star formation at early times such that significant quantities of gas remain for late-time star formation.

Before discussing how our simulations compare to observations and how changes in the stellar and AGN feedback strength affects this comparison, we will first briefly elaborate on the importance of the two most novel aspects of our galaxy formation model, namely the incorporation of radiative AGN feedback and the special treatment of metals for stellar outflows.

**Impact of radiative AGN feedback:** Our galaxy formation model includes a new phenomenological model for radiative (electro-magnetic) AGN feedback. This feedback acts on halo gas by changing the net cooling rates due to the radiation coming from AGN, which is particularly strong during quasar activity. Our model assumes a fixed SED with a simple and rather conservative prescription for obscuration effects. We explored for the first time the impact of this radiative AGN feedback in fully self-consistent large-scale cosmological simulations with a focus on its consequences for the host galaxy in terms of the stellar mass content and overall star formation rates. We find that this form of feedback is more efficient in regulating star formation than purely thermal, continuous quasar-mode AGN feedback, which is mainly relevant to regulate BH growth. However, this radiative form of feedback is only efficient if the BH accretion rates are close to Eddington where the radiation field is strongest. Since this happens only for a rather short period of cosmic time, the impact of mechanical radio-mode feedback is typically significantly stronger than radiative feedback. However, we did not explore possible effects on the ionisation state of the IGM, which could be more substantially influenced by radiative AGN feedback.

**Metal loading of stellar winds:** Our stellar feedback model allows the metal loading of winds to be adjusted separately from the actual mass loading. We found that such a treatment is necessary to reproduce the stellar mass and metal content of galaxies simultaneously. Specifically, we have introduced a wind metal loading factor which is set independently from the wind mass loading factor. This wind metal loading factor defines the relationship between the metallicity of newly created wind particles and the metallicity of the ambient ISM. We found that the traditional wind metal loading leads to an under-production of the gas-phase metallicity and an over enrichment of halo gas. Both of these directly result from the efficient ejection of metals from galaxies via winds. Not only does this lead to poor matches to the observationally constrained mass-metallicity relation, but the over enrichment of halo gas leads to enhanced metal line cooling as well. We can remove this tension with our metal loading scheme for stellar winds. In fact, such a scheme allows us to simultaneously match the mass-metallicity relation and stellar mass function reasonably well. While this wind treatment significantly affects the mass-metallicity relation, it only slightly modifies other observables like the stellar mass function. We note that metal loading factors can be constrained empirically (Zahid et al. 2013). Such studies point to rather low values for  $\gamma_w$ .

**Comparison to observations:** Our fiducial model reproduces many key observables over a wide range of halo masses, covering low mass and high mass systems through the combination of strong stellar and AGN feedback. Most importantly, our model correctly describes the transition region around  $M_{200,\text{crit}} \sim 10^{12} M_\odot$ , where star formation is maximally efficient. We briefly summarise our main findings for each of the key characteristics presented in this paper.

(i) *Cosmic SFR Density:* Our fiducial model reproduces the cosmic

SFR density as a function of redshift reasonably well, although our highest resolution simulation is not yet fully converged. The wind velocity of the stellar feedback has a significant impact on the cosmic SFR density. Fast winds lead to a strong suppression of the SFR, and such fast winds can reduce the star formation even in more massive haloes. The impact of variations of the AGN radio mode is less dramatic and mainly affects the late time decline of the cosmic SFR density, but no radio mode altogether gives a far too high late time SFR.

(ii) *Stellar mass – halo mass relation:* Our model predicts a stellar mass – halo mass relation that is in good agreement with results based on abundance matching. At higher galaxy masses (i.e.  $M > 10^9 M_\odot$ ) we find clear convergence in the stellar mass – halo mass relation. Most importantly, our combination of stellar feedback and radio-mode AGN feedback leads to a shape in the stellar mass – halo mass relation which is in good agreement with abundance matching results, including a correct turnover at the massive end due to efficient quenching through AGN radio-mode feedback in massive haloes. We need strong stellar and AGN feedback to reproduce the stellar content of low and high mass haloes.

(iii) *Stellar mass function:* Our model reproduces the stellar mass function well, although we find that we have slightly too many low mass galaxies in our highest resolution simulation. We find a similar problem for lower mass systems for the stellar mass – halo mass relation. Here we also slightly overproduce the amount of stars in these systems. Both findings indicate the need for yet stronger stellar feedback, which we partially explored in this work by increasing the SNII energy factor by a factor of two. But we note that our fiducial simulation setup includes already rather strong SNII feedback, and increasing this further appears energetically problematic. Radio-mode AGN feedback successfully produces the sharp exponential drop-off of the stellar mass function towards larger stellar masses. We also find that energy-driven winds are required to suppress the low mass end of the stellar mass function sufficiently since they allow for large mass-loading factors for low mass systems compared to momentum-driven winds. This is essentially required to obtain a shallow slope of the stellar mass function at the low mass end.

(iv) *Stellar mass density:* Our fiducial model reproduces the observed stellar mass density reasonably well. The “no feedback” simulation strongly overproduces the amount of stellar mass, whereas the “faster winds” strongly underproduces it. All the other feedback variations are quite close to the fiducial model, which provides the best fit to the data. Changes in the radio-mode AGN feedback only affect the late time evolution of the stellar mass density.

(v) *Tully-Fisher relation:* We find good convergence for the Tully-Fisher relation, and our highest resolution fiducial model agrees very well with observations both in terms of normalisation and slope. This is an important result of our model since it implies that our galaxies, in general, have the correct dynamical structure. Variations of the feedback model parameter choices lead to only negligible changes in the resulting Tully-Fisher relation, implying that the Tully-Fisher relation is a rather stable outcome of our model. The exception is the “fast wind” model which gives rise to the largest change in the Tully-Fisher relation by increasing the rotational velocity at a fixed stellar mass. Also a model without

any feedback does not reproduce the Tully-Fisher relation.

(vi) *Mass-metallicity relation:* Among all the relations that we examined in this paper, the mass-metallicity relation shows the largest tension between observations and our simulations. Although we find a positive correlation between stellar mass and [O/H], the overall amplitude of this relation is not fully correctly reproduced. But given the observational uncertainties we do not consider this a very severe problem at this point. The main issue is that the simulations overpredict the metallicity of higher mass systems. Here our simulations do not predict the turnover in the mass-metallicity relation correctly, and therefore lead to too many metals in massive galaxies. For lower to intermediate mass systems we can only achieve a reasonable agreement with the observations through our novel wind metal loading scheme, which decouples the actual mass loading from the metal loading of winds. Without such a scheme, low mass galaxies particularly would lose far too many metals owing to the high mass loadings of our energy-driven wind scalings. However, such high mass loadings are required to reduce star formation sufficiently in these low mass systems.

(vii) *Luminosity function:* We used stellar population synthesis models to derive SDSS-band luminosity functions (g-, r-, i-, z-bands). Our highest resolution simulations produce luminosity functions at  $z = 0$  which are in reasonable agreement with observations. Especially the faint end slope and the exponential drop towards brighter systems are well reproduced. Our highest resolution simulation has a slightly too high faint-end normalisation compared to the observations. Also the exponential drop happens at slightly too high halo masses. Interestingly, this effect is strongest for the g-band luminosity function, whereas the agreement with the other bands is typically better. Feedback models with faster winds strongly disagree with the observations. Weakening the radio-mode AGN feedback leads to a significant overshoot of the luminosity function at the bright end while weak winds cause an overproduction of faint galaxies.

(viii) *Black hole mass – stellar mass relation:* Black hole growth is mainly regulated by quasar-mode feedback in our model, which results together with BH accretion in a tightly self-regulated feedback loop. Our simulated BH mass – stellar mass relation is well converged and agrees with the observations both in slope and in normalisation. This demonstrates that our modifications to the BH accretion procedure do not affect BH growth in any significant way. Furthermore, the slope of the BH mass – stellar mass relation does not change strongly if we alter the stellar or radio-mode AGN feedback parameters. Normalisation changes in the relation are mainly due to changes in the stellar mass caused by the different feedback choices.

Overall, we find that our fiducial model reproduces a significant number of key observations of the low redshift Universe. As demonstrated in Torrey et al. (2013) our model also reproduces many high redshift observables. Furthermore, Marinacci et al. (2013) shows that our galaxy formation implementation also produces close analogs of Milky Way-like disk galaxies in high resolution simulations of Milky Way-sized DM haloes. We therefore conclude that we have implemented a successful galaxy formation model in the new moving-mesh code AREPO, which is suitable for large-scale galaxy formation simulations. Clearly, the simulations presented in this paper are not sufficient to fully explore all regimes of galaxy formation. Most important, our simulation volume is too

small to sample very high-mass systems and ideally we would like to have slightly higher mass and spatial resolution. The convergence studies presented in this paper show that our model requires a mass resolution of at least  $10^6 h^{-1} M_{\odot}$  for the baryonic component to achieve reasonably converged results. Therefore, predictive large-scale structure simulations with our model require a simulation volume of the order of  $(100 h^{-1} \text{Mpc})^3$  with a mass resolution of the order of  $10^6 h^{-1} M_{\odot}$ , which implies that the simulation has to follow the evolution of many billions of resolution elements. In forthcoming work we will present such simulations based on the methodology presented here (Vogelsberger et al., in prep).

## ACKNOWLEDGEMENTS

The simulations in this paper were run on the Odyssey cluster supported by the FAS Science Division Research Computing Group at Harvard University, the Stampede supercomputer at the Texas Advanced Computing Center, the Magpy Cluster at HITS, and the CURIE supercomputer at CEA/France as part of PRACE project RA0844. We thank Simeon Bird, Laura Blecha, Charlie Conroy, Daniel Eisenstein, Claude-Andre Faucher-Giguere, Chris Hayward, Dusan Keres, Lisa Kewley, Bence Kocsis, Federico Marinacci, Diego Munoz, Dylan Nelson, Rüdiger Pakmor, Christoph Pfrommer, Ewald Puchwein, Vicente Rodriguez-Gomez, Laura Sales, Rob Simcoe, Gregory Snyder, Joshua Suresh, Rob Wiersma, Dandan Xu, and Jabran Zahid for useful discussions. MV acknowledges support from NASA through Hubble Fellowship grant HST-HF-51317.01. VS acknowledges support through SFB 881 'The Milky Way System' of the DFG, and through the European Research Council under ERC-StG grant EXAGAL-308037.

## REFERENCES

- Abazajian, K. N., Adelman-McCarthy, J. K., Agüeros, M. A., et al. 2009, *ApJS*, 182, 543  
 Abel, T. 2011, *MNRAS*, 413, 271  
 Abel, T., & Wandelt, B. D. 2002, *MNRAS*, 330, L53  
 Agertz, O., Teyssier, R., & Moore, B. 2011, *MNRAS*, 410, 1391  
 Agertz, O., Moore, B., Stadel, J., et al. 2007, *MNRAS*, 380, 963  
 Ascasibar, Y., Yepes, G., Gottlöber, S., & Müller, V. 2002, *A&A*, 387, 396  
 Aumer, M., White, S., Naab, T., & Scannapieco, C. 2013, *ArXiv e-prints*  
 Baldry, I. K., Glazebrook, K., & Driver, S. P. 2008, *MNRAS*, 388, 945  
 Bauer, A., & Springel, V. 2012, *MNRAS*, 423, 2558  
 Baugh, C. M. 2006, *Reports on Progress in Physics*, 69, 3101  
 Behroozi, P. S., Wechsler, R. H., & Conroy, C. 2013, *ApJ*, 762, L31  
 Bell, E. F., & de Jong, R. S. 2001, *ApJ*, 550, 212  
 Benson, A. J. 2012, *New Astronomy*, 17, 175  
 Berger, M. J., & Colella, P. 1989, *Journal of Computational Physics*, 82, 64  
 Bird, S., Peiris, H. V., Viel, M., & Verde, L. 2011, *MNRAS*, 413, 1717  
 Bird, S., Vogelsberger, M., Sijacki, D., et al. 2013, *MNRAS*, 429, 3341  
 Blanton, M. R., Lupton, R. H., Schlegel, D. J., et al. 2005, *ApJ*, 631, 208

- Blumenthal, G. R., Faber, S. M., Primack, J. R., & Rees, M. J. 1984, *Nature*, 311, 517
- Booth, C. M., & Schaye, J. 2009, *MNRAS*, 398, 53
- Bouwens, R. J., Illingworth, G. D., Franx, M., & Ford, H. 2008, *ApJ*, 686, 230
- Bower, R. G., Benson, A. J., & Crain, R. A. 2012, *MNRAS*, 422, 2816
- Bower, R. G., Benson, A. J., Malbon, R., et al. 2006, *MNRAS*, 370, 645
- Boylan-Kolchin, M., Springel, V., White, S. D. M., & Jenkins, A. 2010, *MNRAS*, 406, 896
- Brook, C. B., Kawata, D., Gibson, B. K., & Flynn, C. 2004, *MNRAS*, 349, 52
- Bruzual, G., & Charlot, S. 2003, *MNRAS*, 344, 1000
- Cantalupo, S., & Porciani, C. 2011, *MNRAS*, 411, 1678
- Cappellari, M., Bacon, R., Bureau, M., et al. 2006, *MNRAS*, 366, 1126
- Caputi, K. I., Cirasuolo, M., Dunlop, J. S., et al. 2011, *MNRAS*, 413, 162
- Cattaneo, A., Dekel, A., Devriendt, J., Guiderdoni, B., & Blaizot, J. 2006, *MNRAS*, 370, 1651
- Cen, R. 1992, *ApJS*, 78, 341
- Chabrier, G. 2003, *PASP*, 115, 763
- Choi, E., Ostriker, J. P., Naab, T., & Johansson, P. H. 2012, *ApJ*, 754, 125
- Ciotti, L., & Ostriker, J. P. 2007, *ApJ*, 665, 1038
- Ciotti, L., Ostriker, J. P., & Proga, D. 2009, *ApJ*, 699, 89
- Collins, D. C., Xu, H., Norman, M. L., Li, H., & Li, S. 2010, *ApJS*, 186, 308
- Conroy, C., & van Dokkum, P. G. 2012, *ApJ*, 760, 71
- Conroy, C., & Wechsler, R. H. 2009, *ApJ*, 696, 620
- Conroy, C., Wechsler, R. H., & Kravtsov, A. V. 2006, *ApJ*, 647, 201
- Crain, R. A., Theuns, T., Dalla Vecchia, C., et al. 2009, *MNRAS*, 399, 1773
- Croft, R. A. C., Di Matteo, T., Springel, V., & Hernquist, L. 2009, *MNRAS*, 400, 43
- Croton, D. J., Springel, V., White, S. D. M., et al. 2006, *MNRAS*, 365, 11
- Cullen, L., & Dehnen, W. 2010, *MNRAS*, 408, 669
- Dahlen, T., Strolger, L.-G., Riess, A. G., et al. 2004, *ApJ*, 613, 189
- Dalla Vecchia, C., & Schaye, J. 2008, *MNRAS*, 387, 1431
- . 2012, *MNRAS*, 426, 140
- Davé, R., Finlator, K., & Oppenheimer, B. D. 2011a, *MNRAS*, 416, 1354
- Davé, R., Oppenheimer, B. D., & Finlator, K. 2011b, *MNRAS*, 415, 11
- Debuhr, J., Quataert, E., & Ma, C.-P. 2011, *MNRAS*, 412, 1341
- Dekel, A., & Silk, J. 1986, *ApJ*, 303, 39
- Di Matteo, T., Colberg, J., Springel, V., Hernquist, L., & Sijacki, D. 2008, *ApJ*, 676, 33
- Di Matteo, T., Springel, V., & Hernquist, L. 2005, *Nature*, 433, 604
- Dickinson, M., Papovich, C., Ferguson, H. C., & Budavári, T. 2003, *ApJ*, 587, 25
- Dolag, K., Borgani, S., Murante, G., & Springel, V. 2009, *MNRAS*, 399, 497
- Dolag, K., Jubelgas, M., Springel, V., Borgani, S., & Rasia, E. 2004, *ApJ*, 606, L97
- Dolag, K., Reinecke, M., Gheller, C., et al. 2011, in *Astrophysics Source Code Library*, record ascl:1103.005, 3005
- Dolag, K., & Stasyszyn, F. 2009, *MNRAS*, 398, 1678
- Dubois, Y., Devriendt, J., Slyz, A., & Teyssier, R. 2012, *MNRAS*, 420, 2662
- Dubois, Y., Gavazzi, R., Peirani, S., & Silk, J. 2013, *ArXiv e-prints*, 1301.3092
- Dubois, Y., & Teyssier, R. 2008, *A&A*, 477, 79
- Efstathiou, G. 1992, *MNRAS*, 256, 43P
- Elvis, M., Wilkes, B. J., McDowell, J. C., et al. 1994, *ApJS*, 95, 1
- Faucher-Giguère, C.-A., Lidz, A., Hernquist, L., & Zaldarriaga, M. 2008a, *ApJ*, 688, 85
- Faucher-Giguère, C.-A., Lidz, A., Zaldarriaga, M., & Hernquist, L. 2009, *ApJ*, 703, 1416
- Faucher-Giguère, C.-A., Prochaska, J. X., Lidz, A., Hernquist, L., & Zaldarriaga, M. 2008b, *ApJ*, 681, 831
- Few, C. G., Courty, S., Gibson, B. K., et al. 2012, *MNRAS*, 424, L11
- Fontana, A., Salimbeni, S., Grazian, A., et al. 2006, *A&A*, 459, 745
- Francis, P. J., Hooper, E. J., & Impey, C. D. 1993, *AJ*, 106, 417
- Frenk, C. S., White, S. D. M., Bode, P., et al. 1999, *ApJ*, 525, 554
- Genel, S., Vogelsberger, M., Nelson, D., et al. 2013, *ArXiv e-prints*
- Genel, S., et al. 2012, *MNRAS*, 11
- Gerritsen, J. P. E., & Icke, V. 1997, *A&A*, 325, 972
- Gingold, R. A., & Monaghan, J. J. 1977, *MNRAS*, 181, 375
- Gnedin, N. Y. 1995, *ApJS*, 97, 231
- Gnedin, N. Y., & Hollon, N. 2012, *ApJS*, 202, 13
- González, V., Labbé, I., Bouwens, R. J., et al. 2011, *ApJ*, 735, L34
- Governato, F., Brook, C., Mayer, L., et al. 2010, *Nature*, 463, 203
- Greggio, L. 2005, *A&A*, 441, 1055
- Guedes, J., Callegari, S., Madau, P., & Mayer, L. 2011, *ApJ*, 742, 76
- Guo, Q., White, S., Li, C., & Boylan-Kolchin, M. 2010, *MNRAS*, 404, 1111
- Guo, Q., White, S., Boylan-Kolchin, M., et al. 2011, *MNRAS*, 413, 101
- Haas, M. R., Schaye, J., Booth, C. M., et al. 2012a, *ArXiv e-prints*, 1211.1021
- . 2012b, *ArXiv e-prints*, 1211.3120
- Hambrick, D. C., Ostriker, J. P., Naab, T., & Johansson, P. H. 2009, *ApJ*, 705, 1566
- . 2011, *ApJ*, 738, 16
- Häring, N., & Rix, H.-W. 2004, *ApJ*, 604, L89
- Hernquist, L. 1993, *ApJ*, 404, 717
- Hopkins, A. M., & Beacom, J. F. 2006a, *ApJ*, 651, 142
- . 2006b, *ApJ*, 651, 142
- Hopkins, P. F. 2013, *MNRAS*, 428, 2840
- Hopkins, P. F., Cox, T. J., Dutta, S. N., et al. 2009a, *ApJS*, 181, 135
- Hopkins, P. F., Cox, T. J., Hernquist, L., et al. 2013a, *MNRAS*, 430, 1901
- Hopkins, P. F., Hernquist, L., Cox, T. J., Dutta, S. N., & Rothberg, B. 2008, *ApJ*, 679, 156
- Hopkins, P. F., Keres, D., & Murray, N. 2013b, *ArXiv e-prints*
- Hopkins, P. F., Kereš, D., Murray, N., Quataert, E., & Hernquist, L. 2012a, *MNRAS*, 427, 968
- Hopkins, P. F., Lauer, T. R., Cox, T. J., Hernquist, L., & Kormendy, J. 2009b, *ApJS*, 181, 486
- Hopkins, P. F., & Quataert, E. 2010, *MNRAS*, 407, 1529
- Hopkins, P. F., Quataert, E., & Murray, N. 2012b, *MNRAS*, 421, 3522
- . 2012c, *MNRAS*, 421, 3522

- . 2012d, MNRAS, 421, 3488
- Hopkins, P. F., Richards, G. T., & Hernquist, L. 2007, ApJ, 654, 731
- Hummels, C. B., & Bryan, G. L. 2012, ApJ, 749, 140
- Ikeuchi, S., & Ostriker, J. P. 1986, ApJ, 301, 522
- Jubelgas, M., Springel, V., & Dolag, K. 2004, MNRAS, 351, 423
- Jubelgas, M., Springel, V., Enßlin, T., & Pfrommer, C. 2008, A&A, 481, 33
- Kannan, R., Stinson, G. S., Macciò, A. V., et al. 2013, ArXiv e-prints, 1302.2618
- Karakas, A. I. 2010, MNRAS, 403, 1413
- Katz, N., Hernquist, L., & Weinberg, D. H. 1992, ApJ, 399, L109
- Katz, N., Weinberg, D. H., & Hernquist, L. 1996, ApJS, 105, 19
- Kauffmann, G., White, S. D. M., & Guiderdoni, B. 1993, MNRAS, 264, 201
- Kawata, D., & Gibson, B. K. 2003, MNRAS, 340, 908
- . 2005, MNRAS, 358, L16
- Kay, S. T., Pearce, F. R., Frenk, C. S., & Jenkins, A. 2002, MNRAS, 330, 113
- Kereš, D., Vogelsberger, M., Sijacki, D., Springel, V., & Hernquist, L. 2012, MNRAS, 425, 2027
- Kewley, L. J., & Ellison, S. L. 2008, ApJ, 681, 1183
- Kim, J.-h., Wise, J. H., Alvarez, M. A., & Abel, T. 2011, ApJ, 738, 54
- Klypin, A. A., Trujillo-Gomez, S., & Primack, J. 2011, ApJ, 740, 102
- Kobayashi, C. 2004, MNRAS, 347, 740
- Kobulnicky, H. A., & Kewley, L. J. 2004, ApJ, 617, 240
- Korista, K., Baldwin, J., Ferland, G., & Verner, D. 1997, ApJS, 108, 401
- Kurosawa, R., & Proga, D. 2009, MNRAS, 397, 1791
- Le Borgne, D., Rocca-Volmerange, B., Prugniel, P., et al. 2004, A&A, 425, 881
- Leitherer, C., Schaerer, D., Goldader, J. D., et al. 1999, ApJS, 123, 3
- Leitner, S. N., & Kravtsov, A. V. 2011, ApJ, 734, 48
- Lia, C., Portinari, L., & Carraro, G. 2002, MNRAS, 330, 821
- Lilly, S. J., Le Fevre, O., Hammer, F., & Crampton, D. 1996, ApJ, 460, L1
- Ling, F.-S., Nezri, E., Athanassoula, E., & Teyssier, R. 2010, J. Cosmol. Astropart. Phys., 2, 12
- Lucy, L. B. 1977, AJ, 82, 1013
- Madau, P., Pozzetti, L., & Dickinson, M. 1998, ApJ, 498, 106
- Mannucci, F., Della Valle, M., & Panagia, N. 2006, MNRAS, 370, 773
- Maoz, D., Mannucci, F., & Brandt, T. D. 2012, MNRAS, 426, 3282
- Marchesini, D., van Dokkum, P. G., Förster Schreiber, N. M., et al. 2009, ApJ, 701, 1765
- Marinacci, F., Pakmor, R., & Springel, V. 2013, ArXiv e-prints
- Martin, C. L. 2005, ApJ, 621, 227
- Matteucci, F., Panagia, N., Pipino, A., et al. 2006, MNRAS, 372, 265
- McCarthy, I. G., Schaye, J., Font, A. S., et al. 2012, MNRAS, 427, 379
- McCarthy, I. G., Schaye, J., Ponman, T. J., et al. 2010, MNRAS, 406, 822
- McQuinn, M., Lidz, A., Zaldarriaga, M., et al. 2009, ApJ, 694, 842
- Mihos, J. C., & Hernquist, L. 1994, ApJ, 437, 611
- Mitchell, N. L., McCarthy, I. G., Bower, R. G., Theuns, T., & Crain, R. A. 2009, MNRAS, 395, 180
- Monaghan, J. J. 1992, ARA&A, 30, 543
- . 2005, Reports on Progress in Physics, 68, 1703
- Mortlock, A., Conselice, C. J., Bluck, A. F. L., et al. 2011, MNRAS, 413, 2845
- Mosconi, M. B., Tissera, P. B., Lambas, D. G., & Cora, S. A. 2001, MNRAS, 325, 34
- Moster, B. P., Naab, T., & White, S. D. M. 2013, MNRAS, 428, 3121
- Moster, B. P., Somerville, R. S., Maulbetsch, C., et al. 2010, ApJ, 710, 903
- Murray, N., Quataert, E., & Thompson, T. A. 2005, ApJ, 618, 569
- Narayan, R., & Yi, I. 1994, ApJ, 428, L13
- Navarro, J. F., & White, S. D. M. 1993, MNRAS, 265, 271
- Nelson, D., Vogelsberger, M., Genel, S., et al. 2013, MNRAS, 429, 3353
- Ocvirk, P., Pichon, C., & Teyssier, R. 2008, MNRAS, 390, 1326
- Okamoto, T., Frenk, C. S., Jenkins, A., & Theuns, T. 2010, MNRAS, 406, 208
- Okamoto, T., Nemmen, R. S., & Bower, R. G. 2008, MNRAS, 385, 161
- Oppenheimer, B. D., & Davé, R. 2006, MNRAS, 373, 1265
- . 2008, MNRAS, 387, 577
- Oppenheimer, B. D., Davé, R., Kereš, D., et al. 2010, MNRAS, 406, 2325
- O’Shea, B. W., Bryan, G., Bordner, J., et al. 2004, ArXiv Astrophysics e-prints
- Pakmor, R., Bauer, A., & Springel, V. 2011, MNRAS, 418, 1392
- Pakmor, R., & Springel, V. 2012, ArXiv e-prints, 1212.1452
- Pawlik, A. H., & Schaye, J. 2008, MNRAS, 389, 651
- . 2011, MNRAS, 412, 1943
- Peeples, M. S., & Shankar, F. 2011, MNRAS, 417, 2962
- Pen, U. 1998, ApJS, 115, 19
- Pérez-González, P. G., Rieke, G. H., Villar, V., et al. 2008, ApJ, 675, 234
- Perlmutter, S., et al. 1999, ApJ, 517, 565
- Petkova, M., & Springel, V. 2010, MNRAS, 403, 1851
- Pettini, M., & Pagel, B. E. J. 2004, MNRAS, 348, L59
- Piontek, F., & Steinmetz, M. 2011, MNRAS, 410, 2625
- Portinari, L., Chiosi, C., & Bressan, A. 1998, A&A, 334, 505
- Pozzetti, L., Bolzonella, M., Lamareille, F., et al. 2007, A&A, 474, 443
- Price, D. J. 2007, PASA, 24, 159
- . 2008, Journal of Computational Physics, 227, 10040
- Price, D. J., & Federrath, C. 2010, MNRAS, 406, 1659
- Puchwein, E., Sijacki, D., & Springel, V. 2008, ApJ, 687, L53
- Puchwein, E., & Springel, V. 2013, MNRAS, 428, 2966
- Rahmati, A., Pawlik, A. H., Raičević, M., & Schaye, J. 2013, MNRAS, 426, 765
- Read, J. I., & Hayfield, T. 2012, MNRAS, 422, 3037
- Rees, M. J. 1986, MNRAS, 218, 25P
- Rees, M. J., & Ostriker, J. P. 1977, MNRAS, 179, 541
- Reyes, R., Mandelbaum, R., Gunn, J. E., et al. 2012, MNRAS, 425, 2610
- Riess, A. G., Filippenko, A. V., Li, W., et al. 1999, AJ, 118, 2675
- Robertson, B., Cox, T. J., Hernquist, L., et al. 2006, ApJ, 641, 21
- Robertson, B., Yoshida, N., Springel, V., & Hernquist, L. 2004, ApJ, 606, 32
- Saitoh, T. R., & Makino, J. 2013, ApJ, 768, 44
- Sales, L. V., Navarro, J. F., Theuns, T., et al. 2012, MNRAS, 423, 1544
- Sazonov, S. Y., Ostriker, J. P., Ciotti, L., & Sunyaev, R. A. 2005, MNRAS, 358, 168

- Scannapieco, C., Tissera, P. B., White, S. D. M., & Springel, V. 2005, *MNRAS*, 364, 552
- Scannapieco, C., Wadepuhl, M., Parry, O. H., et al. 2012, *MNRAS*, 423, 1726
- Schaye, J., & Dalla Vecchia, C. 2008, *MNRAS*, 383, 1210
- Schaye, J., Dalla Vecchia, C., Booth, C. M., et al. 2010, *MNRAS*, 402, 1536
- Schiminovich, D., & et al. 2005, *ApJ*, 619, L47
- Shakura, N. I., & Sunyaev, R. A. 1973, *A&A*, 24, 337
- Sijacki, D., & Springel, V. 2006, *MNRAS*, 366, 397
- Sijacki, D., Springel, V., Di Matteo, T., & Hernquist, L. 2007, *MNRAS*, 380, 877
- Sijacki, D., Vogelsberger, M., Kereš, D., Springel, V., & Hernquist, L. 2012, *MNRAS*, 424, 2999
- Silk, J. 1977, *ApJ*, 211, 638
- Smith, B., Sigurdsson, S., & Abel, T. 2008, *MNRAS*, 385, 1443
- Somerville, R. S., Hopkins, P. F., Cox, T. J., Robertson, B. E., & Hernquist, L. 2008, *MNRAS*, 391, 481
- Sommer-Larsen, J., Götz, M., & Portinari, L. 2003, *ApJ*, 596, 47
- Springel, V. 2010, *MNRAS*, 401, 791
- Springel, V., Di Matteo, T., & Hernquist, L. 2005a, *ApJ*, 620, L79
- . 2005b, *MNRAS*, 361, 776
- Springel, V., & Hernquist, L. 2002, *MNRAS*, 333, 649
- . 2003a, *MNRAS*, 339, 289
- . 2003b, *MNRAS*, 339, 312
- Springel, V., White, S. D. M., Tormen, G., & Kauffmann, G. 2001, *MNRAS*, 328, 726
- Springel, V., White, S. D. M., Jenkins, A., et al. 2005c, *Nature*, 435, 629
- Springel, V., Wang, J., Vogelsberger, M., et al. 2008, *MNRAS*, 391, 1685
- Steinmetz, M., & Mueller, E. 1994, *A&A*, 281, L97
- Steinmetz, M., & Navarro, J. F. 1999, *ApJ*, 513, 555
- Stinson, G., Seth, A., Katz, N., et al. 2006, *MNRAS*, 373, 1074
- Stinson, G. S., Brook, C., Macciò, A. V., et al. 2013, *MNRAS*, 428, 129
- Stone, J. M., & Norman, M. L. 1992, *ApJS*, 80, 753
- Strolger, L.-G. a. 2004, *ApJ*, 613, 200
- Sutherland, R. S., & Dopita, M. A. 1993, *ApJS*, 88, 253
- Teyssier, R. 2002, *A&A*, 385, 337
- Teyssier, R., Fromang, S., & Dormy, E. 2006, *Journal of Computational Physics*, 218, 44
- Teyssier, R., Moore, B., Martizzi, D., Dubois, Y., & Mayer, L. 2011, *MNRAS*, 414, 195
- Thacker, R. J., & Couchman, H. M. P. 2000, *ApJ*, 545, 728
- Thacker, R. J., Scannapieco, E., & Couchman, H. M. P. 2006, *ApJ*, 653, 86
- Thielemann, F.-K., Argast, D., Brachwitz, F., et al. 2003, in *From Twilight to Highlight: The Physics of Supernovae*, ed. W. Hillebrandt & B. Leibundgut, 331
- Tornatore, L., Borgani, S., Dolag, K., & Matteucci, F. 2007, *MNRAS*, 382, 1050
- Torrey, P., Vogelsberger, M., Genel, S., et al. 2013, *ArXiv e-prints*
- Torrey, P., Vogelsberger, M., Sijacki, D., Springel, V., & Hernquist, L. 2012, *MNRAS*, 427, 2224
- Travaglio, C., Hillebrandt, W., Reinecke, M., & Thielemann, F.-K. 2004, *A&A*, 425, 1029
- Tully, R. B., & Fisher, J. R. 1977, *A&A*, 54, 661
- Turk, M. J., Smith, B. D., Oishi, J. S., et al. 2011, *ApJS*, 192, 9
- van de Voort, F., Schaye, J., Booth, C. M., & Dalla Vecchia, C. 2011, *MNRAS*, 415, 2782
- Vogelsberger, M., Sijacki, D., Kereš, D., Springel, V., & Hernquist, L. 2012, *MNRAS*, 425, 3024
- Vogelsberger, M., Helmi, A., Springel, V., et al. 2009, *MNRAS*, 395, 797
- Wadsley, J. W., Veeravalli, G., & Couchman, H. M. P. 2008, *MNRAS*, 387, 427
- Weiner, B. J., Coil, A. L., Prochaska, J. X., et al. 2009, *ApJ*, 692, 187
- White, S. D. M., & Frenk, C. S. 1991, *ApJ*, 379, 52
- White, S. D. M., & Rees, M. J. 1978, *MNRAS*, 183, 341
- Wiersma, R. P. C., Schaye, J., & Smith, B. D. 2009a, *MNRAS*, 393, 99
- Wiersma, R. P. C., Schaye, J., Theuns, T., Dalla Vecchia, C., & Tornatore, L. 2009b, *MNRAS*, 399, 574
- Woodsley, S. E., & Weaver, T. A. 1995, *ApJS*, 101, 181
- Wu, H.-Y., Hahn, O., Wechsler, R. H., Mao, Y.-Y., & Behroozi, P. S. 2013, *ApJ*, 763, 70
- Yu, Q., & Tremaine, S. 2002, *MNRAS*, 335, 965
- Zahid, H. J., Dima, G. I., Kewley, L. J., Erb, D. K., & Davé, R. 2012, *ApJ*, 757, 54
- Zahid, H. J., Torrey, P., Vogelsberger, M., et al. 2013, *ArXiv e-prints*
- Zamorani, G., Henry, J. P., Maccacaro, T., et al. 1981, *ApJ*, 245, 357